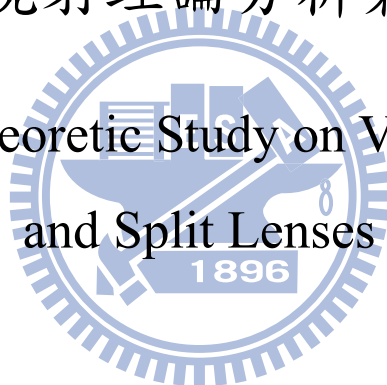# 國立交通大學

光電工程研究所

博士論文

廣義裂片的繞射理論分析兼論向量光束

Diffraction Theoretic Study on Vectorial Beams
and Split Lenses

研 究 生：鄭介任

指導教授：陳志隆

中華民國 九十九 年 八 月

廣義裂片的繞射理論分析兼論向量光束

Diffraction Theoretic Study on Vectorial Beams and Split Lenses

研究生：鄭介任　　　　Student : Chieh-Jen Cheng

指導教授：陳志隆　　　Advisor : Jyh-Long Chern

國立交通大學

光電工程研究所

博士論文

1896

A Dissertation
Submitted to Department of Photonics and Institute of Electro-Optical
Engineering
College of Electrical and Computer Engineering
National Chiao Tung University
in Partial Fulfillment of the Requirements
for the Degree of Doctor of Philosophy
in
Electro-Optical Engineering
August 2010
Hsinchu, Taiwan

中華民國 九十九 年 八 月

廣義裂片的繞射理論分析兼論向量光束

博士研究生：鄭介任　　指導教授：陳志隆教授

國立交通大學　　光電工程研究所

摘　要

對切透鏡有比勒(Billet)橫向及梅斯林(Meslin)縱向切割兩種型式。比勒對切透鏡在遠場會產生雙曲面及等間距直線這兩種干涉條紋，而梅斯林對切透鏡在兩透鏡焦點中間附近會產生半圓型的干涉條紋。本論文延伸對切透鏡成裂解透鏡，並討論比勒裂解透鏡之焦點形成一個圓形時的遠場干涉條紋分佈情形及其相對於光軸的對稱性；在梅斯林裂解透鏡中，我們將一個圓透鏡切割成$2N$塊等角度透鏡，編號為單數與雙數分別放置於不同焦點處，並討論其光場分佈之對稱性。相對於通過兩焦點之中心點的垂直面；N為單數時，振幅及相位分別為鏡面反射對稱及反對稱(扣除π相位角)，N為偶數時，在鏡面反射對稱與反對稱外要再加上額外的$2\pi/N$的旋轉角。此外，從光場的漸近表示式可以得知比勒裂解透鏡可以用來產生貝索光束(Bessel beam)，並可再經由另一透鏡消除發散相位成一無繞射貝索光束(non-diffracting Bessel beam)。相對於傳統的環形孔徑，使用此透鏡所產生的貝索光束可以攜帶更多能量。有趣的是在漸近表示式中，貝索函數之參數與數值孔徑無關，但是數值孔徑卻決定了漸近表示式的適用範圍。因此，數值孔徑會決定貝索光束的發散情形與其所適用的漸近表示式範圍。

另一方面，在完美透鏡(perfect lens)成像系統中，焦點位移(Focal shift)效應發生於菲涅耳數(Fresnel number)小於10的情形之下，若使用線偏振光(linearly polarized)的入射光學系統中，則焦點位移效應與菲涅耳數及數值孔徑皆成反比。本論文討論在徑向偏振光(radially polarized)及方位偏振光(azimuthally polarized)入射情形下，焦點位移效應與菲涅耳數及數值孔徑並不會只有單純反比關係。此外，三種不同偏振光在同一個系統參數下(亦即相同菲涅耳數和數值孔徑)，方位偏振光所造成的焦點位移效應最嚴重，徑向偏振光次之，線偏振光最輕微。

Diffraction Theoretic Study on Vectorial Beams and Split Lenses

Doctoral Student: Chieh-Jen Cheng **Advisor:** Dr. Jyh-Long Chern

Institute of Electro-Optical Engineering

National Chiao Tung University

Abstract

This study examines the diffraction properties of the generalized split N-sector lens originating from the configuration of Meslin's experiment and the Billet's split bi-sector lens. In Billet's N-split lens, the type of lens splitting selected causes the interference pattern of equidistant straight lines in the original Billet's lens to form an N-fold angularly distributed pattern with an angle difference of $2\pi/N$. For an odd number of splitting N, there is an additional angle shift of π/N for the azimuthally distributed patterns of equidistant straight lines. In other words, there are two kinds of symmetry even for simple splitting operations. On the other hand, the peak intensity distribution in the central portion resembles a concentric-circle-like pattern, when N is large as a result of N-beam interference. As to the Meslin's N-split lens, the amplitude and the phase follow $\left|U(-u,v,\psi+\dfrac{2\pi}{N})\right| = \left|U(u,v,\psi)\right|$ and $\Phi(-u,v,\psi+\dfrac{2\pi}{N}) = -\Phi(u,v,\psi)-\pi$ respectively when the splitting is with double of an even number. On the other hand, for the case of double of an odd number, the relation changes to hold with $\left|U(-u,v,\psi)\right| = \left|U(u,v,\psi)\right|$ and $\Phi(-u,v,\psi) = -\Phi(u,v,\psi)-\pi$, where the optical units u and v are used to denote the z- and the radial coordinates respectively and the azimuthal angle is ψ. Additional symmetry properties are also explored and identified, particularly for the distributions on the focal plane.

Moreover, the Bessel beam is studied and by the use of the Billet's *N*-split lens distributing the focal points circularly on the focal plane. This study explores the characteristics of beam propagation and analytically derives the asymptotic characteristics of beam propagation based on the stationary phase approximation and the moment-free Filon-type method. Results show that the unique Billet's *N*-split lens can generate a quasi-Bessel beam if the number of splitting *N* is large enough, e.g., $N \geqq 24$. This study also explores the diffraction efficiency of corresponding quasi-Bessel beam and the influence of aperture size. The potential advantage of proposed split-lens approach is that, unlike the classical means of annual aperture, this simple lens approach allows a much large throughput in creating the Bessel beam and hence the Bessel beam could have more optical energy.

The diffraction behaviors of cylindrical vector beam, particularly the focal shifts further caused by different polarizations, namely linear, radial and azimuthal, are also investigated. The variation of focal shifts associated with numerical aperture and the Fresnel number is also explored. It is found that with a low numerical aperture, e.g., 0.1, the focal shifts associated by the radially and azimuthally polarized illuminations are nearly the same, while they are about 1.65 times as large as that of linearly polarized illumination. As the system is of high numerical aperture, e.g., 0.9, the focal shifts associated by the radially and azimuthally polarized illuminations have ~10% difference and their ratios with that of linearly polarized illumination become double in comparing with the case of low numerical aperture. In general, azimuthally polarized illumination has the largest power in shifting the focal point.

誌　謝

　　從大學畢業後就來到風城求學，經過這九個年頭的努力後，終於順利拿到光電工程博士學位，感謝上天！感謝博士論文指導教授陳志隆老師多年來的指導與提攜。陳老師傳道、授業、解惑的恩惠，學生沒齒難忘。也感謝博士論文考試委員們施宙聰老師、許瑞榮老師、郭浩中老師、賴暎杰老師及謝文峰老師，給予學生許多寶貴的建議。

　　感謝鄭伊凱學長、朱淑君同學、曹兆璽同學及鄭竹明同學在求學過程中的諸多幫忙及鼓勵。也感謝學弟妹們家佑、志雲、建成、夢華、玫君、家瑜、奎佐、燃宏、志傑、冠廷、健榮、璧榮、建德、志明、肇佑、保嘉、怡文、偉傑、宏智、偉宏、柏宇、意雯的協助，有了你們的加入，實驗室更顯朝氣。感謝偉宏、柏宇、意雯三位學弟妹們於己丑年孟秋幫忙進行實驗室搬遷，讓實驗室能順利從電資大樓搬到田家炳光電大樓。
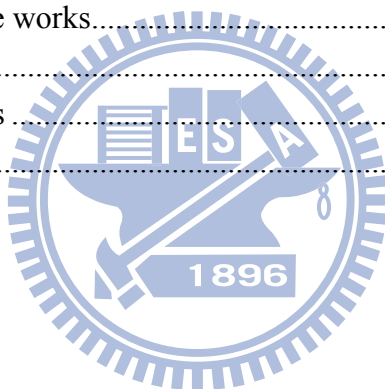
　　最後，感謝父母親對我的栽培，也感謝家人的支持、鼓勵與包容；同時也感謝芳能一直陪在我身邊；感謝每一位曾經幫助我的人，謝謝。

　　　　　　　　　　　　　　　　　　　　　－庚寅年申月　風城交大

Contents

List of Figures

List of Tables

1

Introduction

It is a classical topic to study field propagation and its associated diffraction behavior in the image space of an optical system. The resultant electric fields in the image space are determined crucially by the optical system. In existing literature, the optical systems with perfect lenses are classical platforms for exploring diffraction behavior. The current study considers a different approach that may be able to provide an additional basic reference for diffraction study, namely the generalized form of a split lens. There are many ways to achieve lens splitting; for example, in a configuration of Meslin's experiment or using Billet's split lens. Once a lens is split in multiple pieces, the resulting interference involves multiple beams and the configuration of multiple paths. This creates complicated beam propagation and interference. Nevertheless, if this generalization is implemented symmetrically, the field distribution exhibits an embedded symmetry, which reduces and simplifies the complexity of analysis and calculation. Thus, exploring the diffraction behavior with such a generalization, particularly the symmetry properties, is worthy of further research. Therefore, this study presents such a generalization of Billet's split lens and Meslin's split lens and

therefore the propagation characteristics of the beams generated by Billet's N-split

lens manipulating the resultant electromagnetic fields.

The exploration of the beam propagation characteristics of a polarized beam is not

only important for fundamental understanding but also to provide a useful mean in

exploring and probing the other systems as polarized illumination. In paraxial optics,

the numerical aperture of the lens is small and the polarization characteristic

properties of light sources are ignored. Nonetheless the polarization effect can not be

ignored when the numerical aperture of lens becomes extremely large. When vector

nature is included in consideration, the performance will be influenced where the

focal property is always the first item to be checked because of its importance to

application. The polarization properties of incident wave, and therefore, are important

when we study the electromagnetic fields in an optical system having a high

numerical aperture. For a light source with a special polarization, the polarization

properties are crucial to the diffracted electromagnetic fields. Here some polarizations

are listed below.

1.   Uniform polarizations; linearly polarization, circularly polarization.

2.   Non-uniform polarizations; radially polarization or azimuthally polarization.

1.1   Incident beams – scalar field
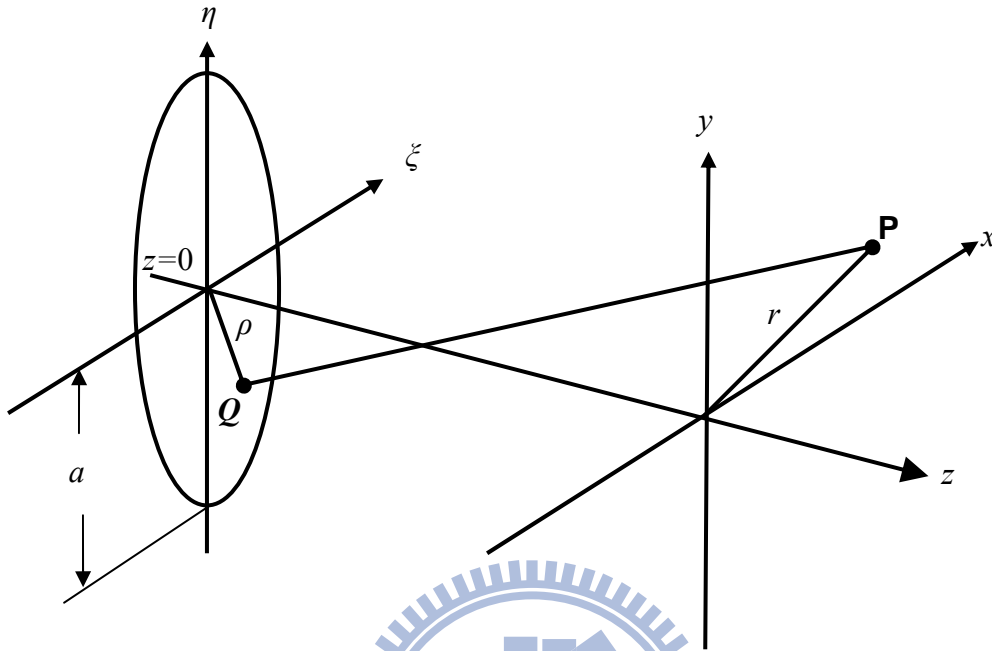
Fig. 1-1 Schematic diagram of diffraction by a circular aperture.

Fig. 1-1 shows the schematic diagram for the diffraction by an aperture. By the

application of the first Rayleight-Sommerfeld diffraction formula, the diffracted field

$U(P)$ by an aperture, having the field $u(\xi,\eta,0)$, can be written as [1]

$$U(P) = -\frac{1}{2\pi}\int_{-\infty}^{\infty}\int_{-\infty}^{\infty} u(\xi,\eta,0)\frac{\partial}{\partial z}\frac{\exp(ikR)}{R}d\xi d\eta,\qquad(1\text{-}1)$$

where $k=2\pi/\lambda$ is the wavenumber of the incident wave, λ is the wavelength and

$R = \left[(x-\xi)^2 + (y-\eta)^2 + z^2\right]^{\frac{1}{2}}$.

$$U(P) = -\frac{z}{2\pi}\int_{-\infty}^{\infty}\int_{-\infty}^{\infty} u(\xi,\eta,0)\frac{ikR-1}{R}\frac{\exp(ikR)}{R^2}d\xi d\eta.\qquad(1\text{-}2)$$

When $kR \gg 1$, the diffraction field can be expressed as

$$U(P) = \frac{z}{i\lambda} \int_{-\infty}^{\infty} \int_{-\infty}^{\infty} u(\xi,\eta,0) \frac{\exp(ikR)}{R^2} d\xi d\eta, \qquad (1\text{-}3)$$

By use of Taylor series expansion of the square root $R \approx z\left[\frac{1}{2}\left(\frac{x-\xi}{z}\right)^2 + \frac{1}{2}\left(\frac{y-\eta}{z}\right)^2 + 1\right]$ and keep only the first two terms the diffraction field now is

$$U(P) = \frac{e^{ikz}}{i\lambda z} \int_{-\infty}^{\infty} \int_{-\infty}^{\infty} u(\xi,\eta,0) \exp\left\{i\frac{k}{2z}\left[(x-\xi)^2 + (y-\eta)^2\right]\right\} d\xi d\eta, \qquad (1\text{-}4)$$

which is the *Fresnel diffraction integral* or the *near field* diffraction of the aperture. To meet sufficient criteria for accuracy, the maximum phase changed by the leading term of dropped series has much less than 1 radian. Thus z has to satisfy

$$z^3 \gg \frac{\pi}{4\lambda}\left[(x-\xi)^2 + (y-\eta)^2\right]_{\max}^2. \qquad (1\text{-}5)$$

If $z \gg \frac{k(\xi^2 + \eta^2)_{\max}}{2}$ is applicable the diffracted field can be further simplified as

$$U(P) = \frac{e^{ikz} e^{i\frac{k}{2z}(x^2+y^2)}}{i\lambda z} \int_{-\infty}^{\infty} \int_{-\infty}^{\infty} u(\xi,\eta,0) \exp\left[-i\frac{2\pi}{\lambda z}(x\xi + y\eta)\right] d\xi d\eta, \qquad (1\text{-}6)$$

which is the *Fraunhofer diffraction integral* or the *far field* diffraction of the aperture.

When a circular aperture with radius a illuminated by a unit-amplitude plane-wave, i.e., $u(\xi,\eta,0)=1$, the on-axis diffracted field by the first Rayleigh-Sommerfeld theory can be expressed as [2]

$$U(z) = z\left[\frac{\exp(ikz)}{z} - \frac{\exp\left(ik\sqrt{z^2 + a^2}\right)}{\sqrt{z^2 + a^2}}\right].$$ (1-7)

The Fresnel diffraction integral can be written as [1]

$$U(P) = \frac{2\pi e^{ikz} e^{\frac{ik}{2z}r^2}}{i\lambda z}\int_0^a J_0\left(\frac{kr\rho}{z}\right)\exp\left(\frac{ik}{2z}\rho^2\right)\rho d\rho,$$ (1-8)

The Fraunhofer diffraction integral now is [1]

$$U(P) = \pi a^2 \frac{e^{ikz} e^{i\frac{k}{2z}r^2}}{i}\frac{2J_1\left(ka\frac{r}{z}\right)}{ka\frac{r}{z}}.$$ (1-9)

This is the so-called Airy pattern.

Fig. 1-2 shows the diffracted intensity $|U(P)|^2$ by a circular aperture with radius

a=20λ. In the top of Fig. 1-2, the geometry and the intensity line scans through the

radial direction at various distances from the aperture z=0.5, 90, 210, 350, 500, and

650λ are illustrated. The near field of the aperture when z=0.5λ is clearly shown and

the Fresnel region can be recognized when z is beyond the near field of the aperture to

z~400λ. The Fraunhofer region is approximately beyond z=400λ as the last two curves

shown. The middle of Fig. 1-2 displays the intensity distribution in the meridional

plane and the on-axis intensity is shown in the bottom of Fig. 1-2.
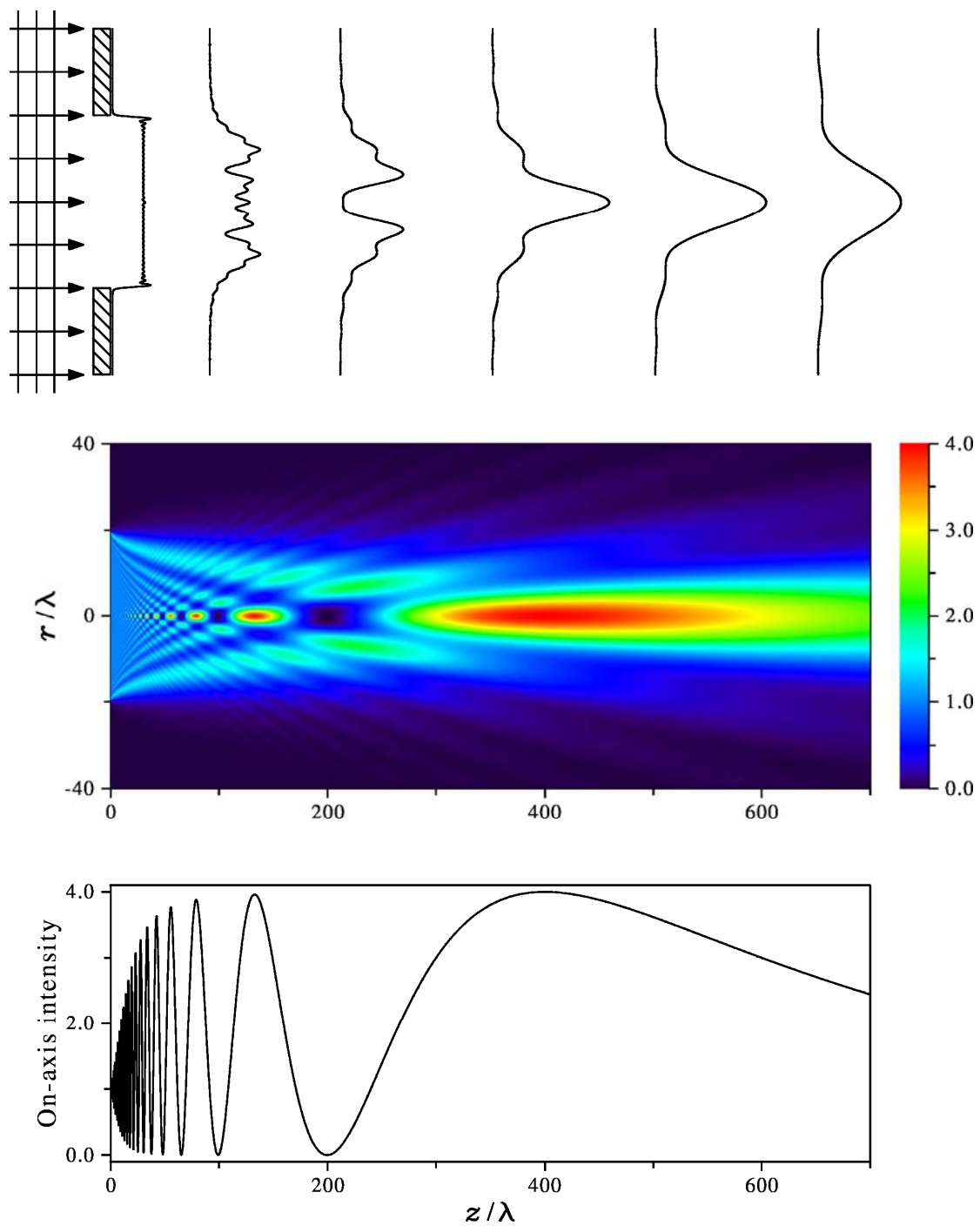
Fig. 1-2 Diffraction by a circular aperture with radius $a=20\lambda$. *Top*: Geometry and the intensity line scans at various distances $z=0.5, 90, 210, 350, 500,$ and 650λ. *Middle*: The intensity distribution in the meridional plane. *Bottom*: The on-axis intensity.

1.2   Optics

Assume we have an aberrated wavefront and pass through a circular aperture. The aberrated wavefront is a deformation of a spherical wave and the spherical wave converges towards an axial focal point $F(0,0,0)$. According to the classical scalar Debye diffraction theory the field at an observation point $P(x,y,z)$ is then given as [3]

$$U(P) = -\frac{i}{\lambda}\frac{a^2 A}{f^2} e^{i(\frac{f}{a})^2 u} \int_0^1 \int_0^{2\pi} e^{i\left[k\Phi(\rho,\theta)-v\rho\cos(\theta-\psi)-\frac{1}{2}u\rho^2\right]} \rho d\rho d\theta , \qquad (1\text{-}10)$$

where the optical units u, v, and ψ represent the Cartesian coordinate positions of P $(x,$ $y,$ $z)$. These values are $u = \frac{2\pi}{\lambda}\left(\frac{a}{f}\right)^2 z$, $v = \frac{2\pi}{\lambda}\left(\frac{a}{f}\right)r = \frac{2\pi}{\lambda}\left(\frac{a}{f}\right)\sqrt{x^2+y^2}$, where $x = r\cos\psi$ and $y = r\sin\psi$. $\Phi(\rho,\theta)$ is the aberration function. Fig. 1-3 shows the coordinate system.
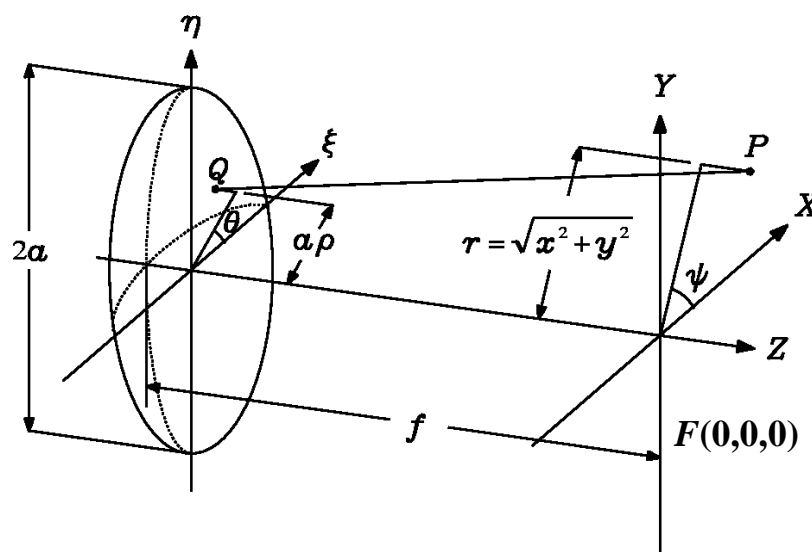
Fig. 1-3 Geometry for focusing through a circular aperture. The focal point lies on the origin of the *XYZ* Cartesian coordinate and the diffracted field is observed at *P(x,y,z)*.

1.2.1   Perfect lens

In the absence of aberrations, i.e. when $\Phi(\rho,\theta)=0$, the diffracted field of the double

integral in Eq. (1-10) can be simplified to one integral by carrying out the integral

with respect to θ using $\dfrac{i^{-n}}{2\pi}\displaystyle\int_0^{2\pi}e^{ix\cos\alpha}e^{in\alpha}\mathrm{d}\alpha = J_n(\alpha)$ where $J_n(\alpha)$ is Bessel function

of first kind.

$$U(P) = -\frac{i2\pi a^2 A}{\lambda f^2}e^{i(\frac{f}{a})^2 u}\int_0^1 J_0(v\rho)e^{-\frac{1}{2}iu\rho^2}\rho d\rho, \qquad (1\text{-}11)$$

This integral can be further carried out when $u=0$ i.e., the field in the focal plane is

$$U(P) = -\frac{i2\pi a^2 A}{\lambda f^2}e^{i(\frac{f}{a})^2 u}\frac{J_1(v)}{v}, \qquad (1\text{-}12)$$

The intensity $I=|U|^2=\left[\dfrac{2J_1(v)}{v}\right]^2 I_0$ is the Airy formula for Fraunhofer diffraction at a

circular aperture where $I_0 = \left(\dfrac{\pi a^2 |A|}{\lambda f^2}\right)^2$.

The intensity distribution in the focal plane is characterized by the Airy function

shown in Fig. 1-4. The bottom of Fig. 1-4 shows the line scan through the focus and

the Airy function can be observed clearly. Fig. 1-5 shows the intensity distribution in

the meridional plane. The dashed lines indicate the boundary of the geometrical

shadow. The Airy pattern can be also observed in the radial directionFig. 1-4.
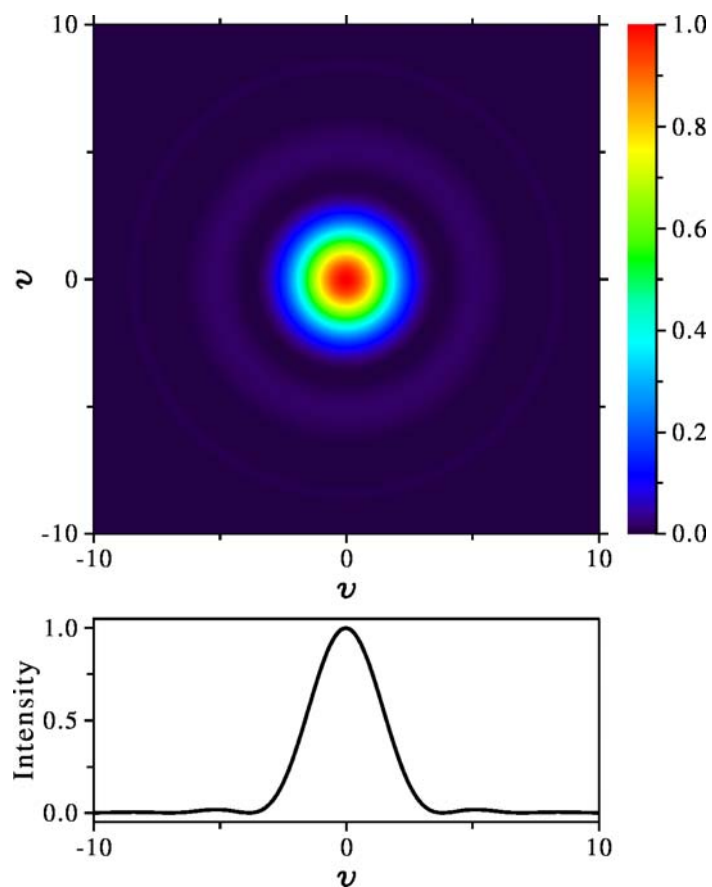
Fig. 1-4 Density plot of intensity distribution in the focal plane and the Airy pattern is clearly seen. The intensity is normalized to unity at focus.
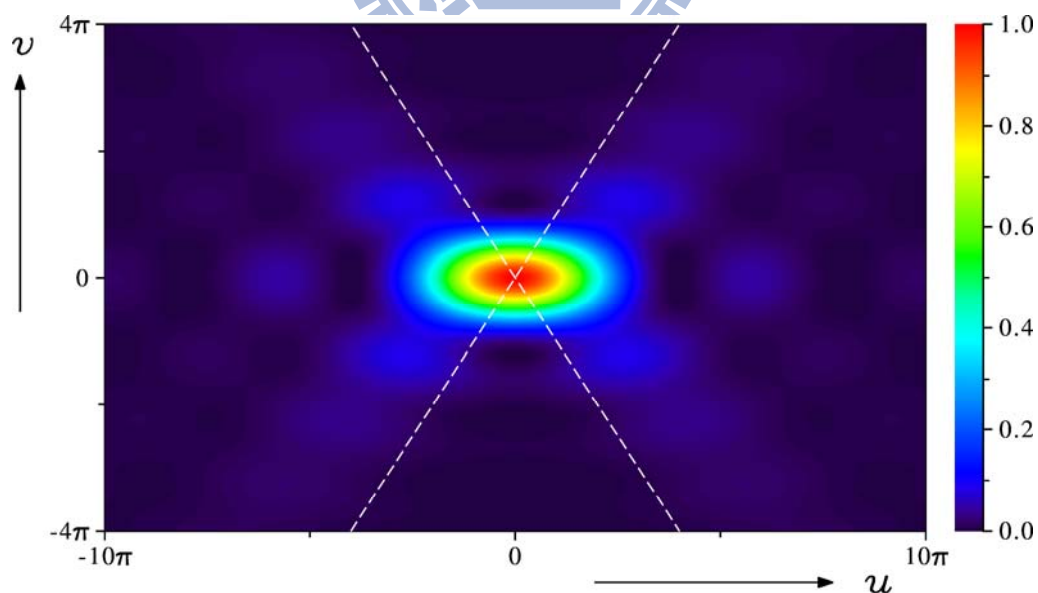
Fig. 1-5 Density and contour plot of intensity distribution in the meridional plane near focus of a converging spherical wave diffracted at a circular aperture. The intensity is normalized to unity at focus. The dashed lines represent the boundary of the geometrical shadow.

1.2.2   A lens with aberration

1.2.2.1 Primary spherical aberration

In the presence of primary spherical aberration only, the aberration function is

$$\Phi(\rho,\theta) = W_{040}\rho^4, \qquad (1\text{-}13)$$

where W_{040} is the amount of wavefront deformation at the aperture edge, measured in units of wavelengths. On substituting Eq. (1-13) and carrying out the integral carrying out the integral with respect to θ by the Bessel function, the Eq. (1-10) yields

$$U(P) = -\frac{i2\pi a^2 A}{\lambda f^2} e^{i(\frac{f}{a})^2 u} \int_0^1 J_0(v\rho) e^{i\left(kW_{040}\rho^4 - \frac{1}{2}u\rho^2\right)} \rho d\rho. \qquad (1\text{-}14)$$

From Eq. (1-14) the intensity is rotationally symmetry about the optical axis in the primary spherical aberration.

$$U(P) = -\frac{i\pi a^2 A}{2\lambda f^2} e^{i(\frac{f}{a})^2 u} \int_{-\frac{1}{2}}^{\frac{1}{2}} e^{i\frac{1}{2}u_F\left(\rho - \frac{u'}{2u_F}\right)^2} d\rho, \qquad (1\text{-}15)$$

where $u'=u-u_F$ and $u_F=4\pi W_{040}$.

The axial intensity from Eq (1-15) is symmetric about the point $u=u_F=4\pi W_{040}$ and the diffraction foci, a unique position (u_F, v_F, ψ_F) has the maximum intensity, is $(4\pi W_{040}, 0, 0)$. The schematic diagram for a lens having primary spherical aberration

with ray-tracing is shown in Fig. 1-6 where the caustic curves can be readily observed.

The intensity distribution in the meridional plane for the case of the aberration-free, in

the presence of primary spherical aberration W_{040}=-0.5λ and W_{040}=-1λ are shown in

Fig. 1-7. The dashed lines indicate the geometrical caustics.
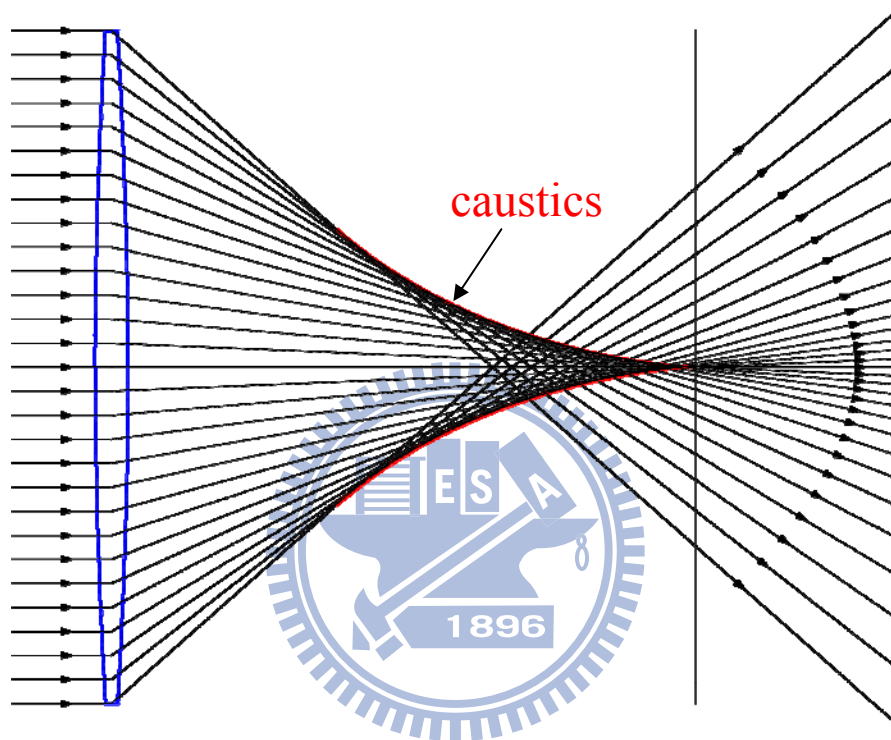
Fig. 1-6 Schematic diagram of ray-tracing of a lens in the presence of primary spherical aberration. The caustic curve can be easily seen and the wavefront is also seen by connecting the arrows in all of the rays.
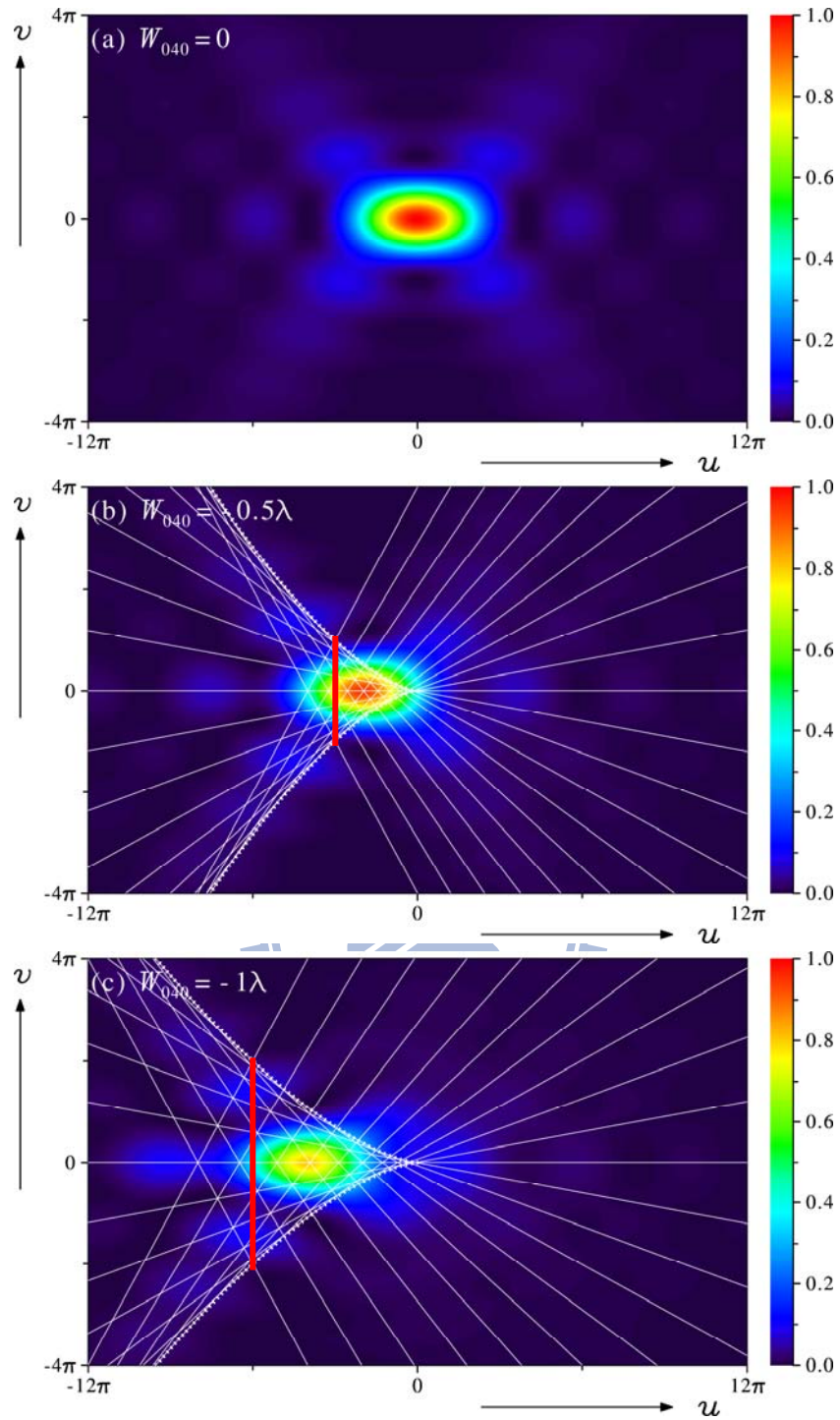
Fig. 1-7 Density and contour plot of intensity distribution in the meridional plane near focus diffracted at a circular aperture in the aberration-free (W_{040}=0) and in the presence of primary spherical aberration ($\Phi = W_{040}\rho^4$) of half a wavelength (W_{040}=-0.5λ) and one wavelength (W_{040}=-1λ). The dashed lines indicate the geometrical caustics and red vertical line denotes the diffraction focus. (a) W_{040}=0; (b) W_{040}=-0.5λ and (c) W_{040}=-1λ.

1.2.2.2 Primary comatic aberration

In the presence of primary comatic aberration only, the aberration function is

$$\Phi(\rho, \theta) = W_{031}\rho^3 \cos\theta, \tag{1-16}$$

and therefore, the Eq. (1-10) gives rise to

$$U(P) = -\frac{i}{\lambda}\frac{a^2 A}{f^2}e^{i(\frac{f}{a})^2 u}\int_0^1\int_0^{2\pi}e^{i\left[kW_{031}\rho^3\cos\theta - v\rho\cos(\theta - \psi) - \frac{1}{2}u\rho^2\right]}\rho\, d\rho\, d\theta. \tag{1-17}$$

Schematic diagram of ray-tracing through a lens in the presence of primary comatic aberration is shown in Fig. 1-8 and the geometrical confusion figures are also shown on the right side.
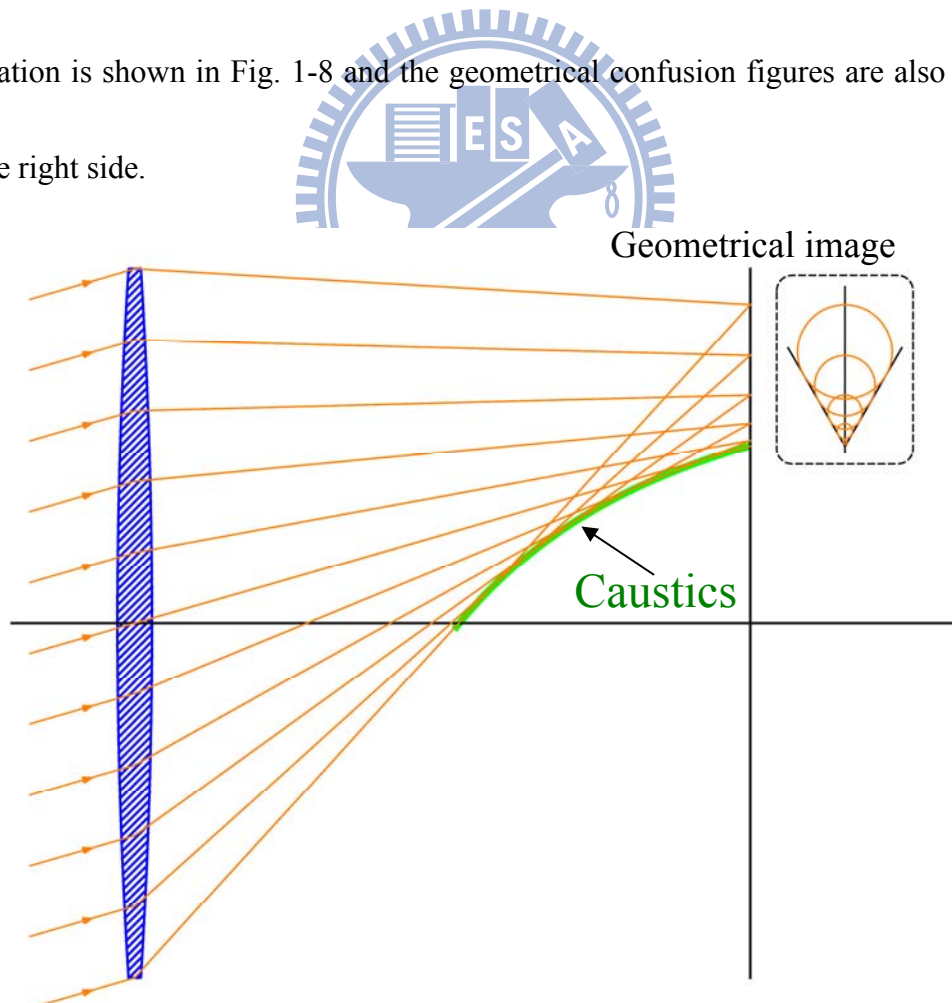
Fig. 1-8 Schematic diagram of ray-tracing through a lens in the presence of primary comatic aberration. The geometrical confusion figures are also shown.

The intensity distribution at the geometrical focal plane in the presence of primary

comatic aberration $W_{031}=0.5\lambda$, $W_{031}=1\lambda$ and $W_{031}=3\lambda$ are shown in Fig. 1-9. The

diffraction focus lies in the geometrical focal plane in the presence of primary comatic

aberration. When the W_{031} is small, the location of diffraction focus is given by [3]

$v_F=\frac{2}{3}kW_{031}$ and $\psi_F=0$. As expected, it agrees well with the diffraction foci in Fig. 1-9

(a) and (b). However, the diffraction foci in Fig. 1-9 (c) is $v_F{\sim}5.4$ instead of $v_F=4\pi$

because a large comatic aberration $W_{031}=3\lambda$ is used here.
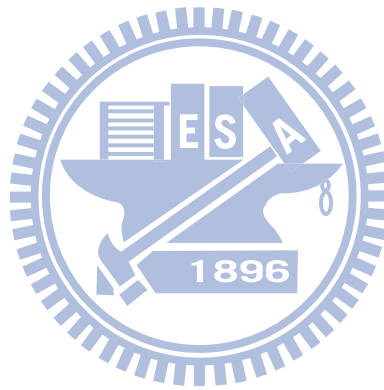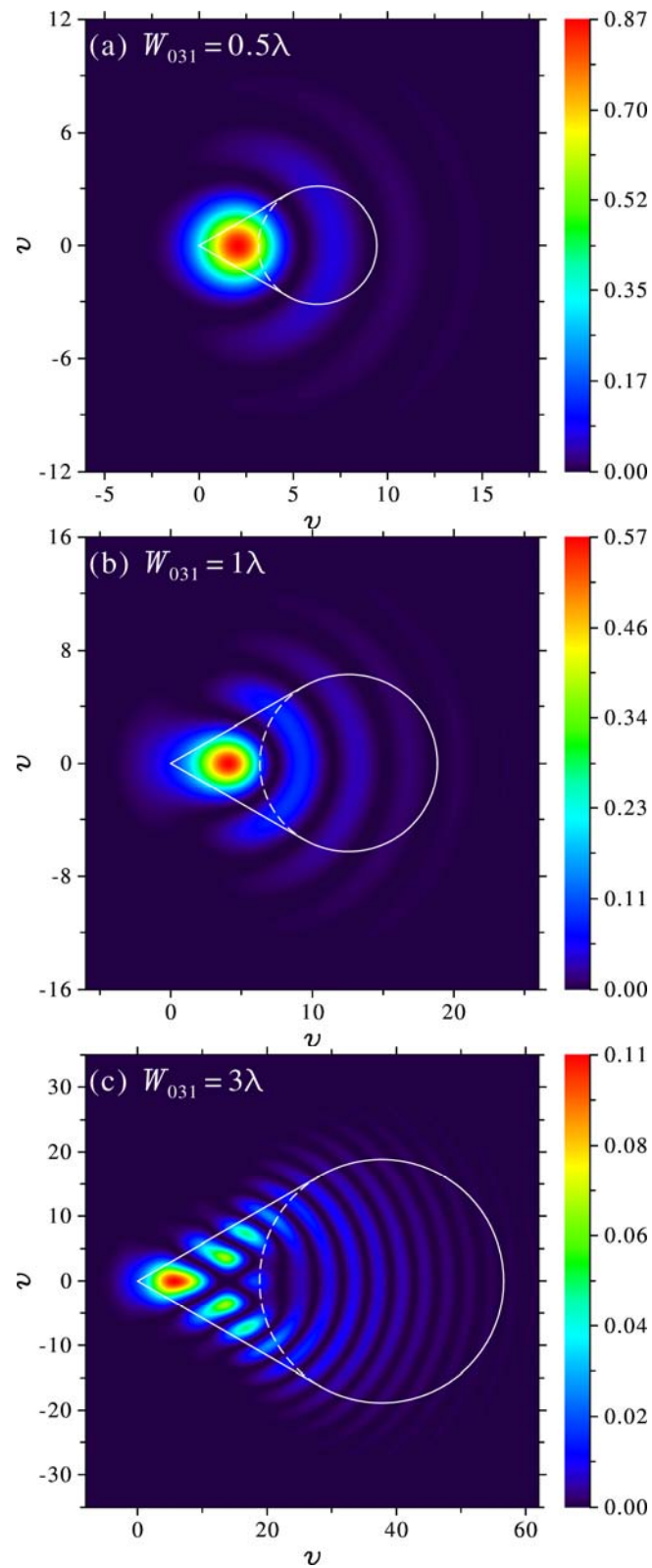
Fig. 1-9 Intensity distribution at the geometrical focal plane in the presence of primary comatic aberration. The boundary of geometrical confusion figures is also shown. (a) $W_{031}=0.5\lambda$; (b) $W_{031}=1\lambda$ and (c) $W_{031}=3\lambda$.

1.2.2.3 Primary astigmatism

In the presence of primary astigmatism only, the aberration function can be written as

$$\Phi(\rho,\theta) = W_{022}\rho^2 \cos^2\theta, \tag{1-18}$$

and therefore, the Eq. (1-10) yields

$$U(P) = -\frac{i}{\lambda}\frac{a^2 A}{f^2} e^{i(\frac{f}{a})^2 u} \int_0^1 \int_0^{2\pi} e^{i\left[kW_{022}\rho^2 \cos^2\theta - v\rho\cos(\theta-\psi) - \frac{1}{2}u\rho^2\right]} \rho d\rho d\theta. \tag{1-19}$$

From Eq. (1-19) the intensity distribution has reflection symmetry about both x and y axis. Fig. 1-10 shows the schematic diagram of a lens having primary astigmatism. In the sagittal focal plane $u = u_S = 0$, the Eq. (1-19) gives rise to

$$U(P) = -\frac{i}{\lambda}\frac{a^2 A}{f^2} e^{i(\frac{f}{a})^2 u} \int_0^1 \int_0^{2\pi} e^{i\left[kW_{022}\rho^2 \cos^2\theta - v\rho\cos(\theta-\psi)\right]} \rho d\rho d\theta. \tag{1-20}$$

In the tangential focal plane $u = u_T = 2kW_{022}$, the Eq. (1-19) is

$$U(P) = -\frac{i}{\lambda}\frac{a^2 A}{f^2} e^{i(\frac{f}{a})^2 u} \int_0^1 \int_0^{2\pi} e^{-i\left[kW_{022}\rho^2 \sin^2\theta + v\rho\cos(\theta-\psi)\right]} \rho d\rho d\theta. \tag{1-21}$$

The diffraction pattern in the sagittal focal plane is the same as in the tangential focal plane, except for a rotation of 90°. The diffraction focus in the presence of a small amount of primary astigmatism situates in the central plane $u_F = kW_{022}$, midway between the sagittal and the tangential focal lines [3]. Fig. 1-11 shows the intensity

distribution in the presence of primary astigmatism $W_{022}=0.64\lambda$ at the geometrical

focal plane, at $u=k\ W_{022}$ and $u=2kW_{022}$. As expected, the intensity patterns in Fig.

1-11(a) and Fig. 1-11(c) show the rotation of 90° with respect to the optical axis.
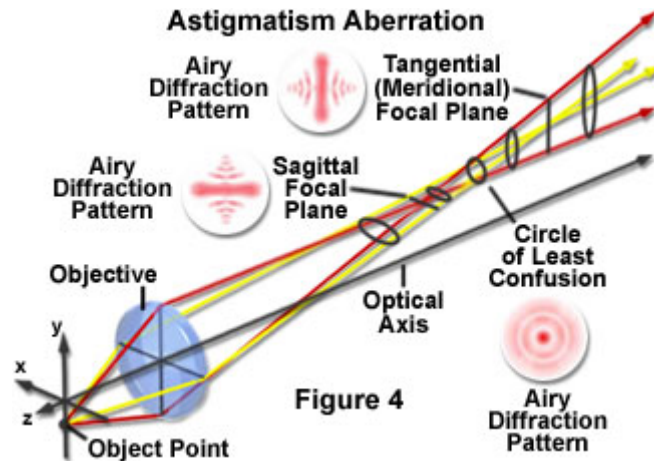
Fig. 1-10 Schematic diagram of a focusing lens in the presence of primary astigmatism. [5]
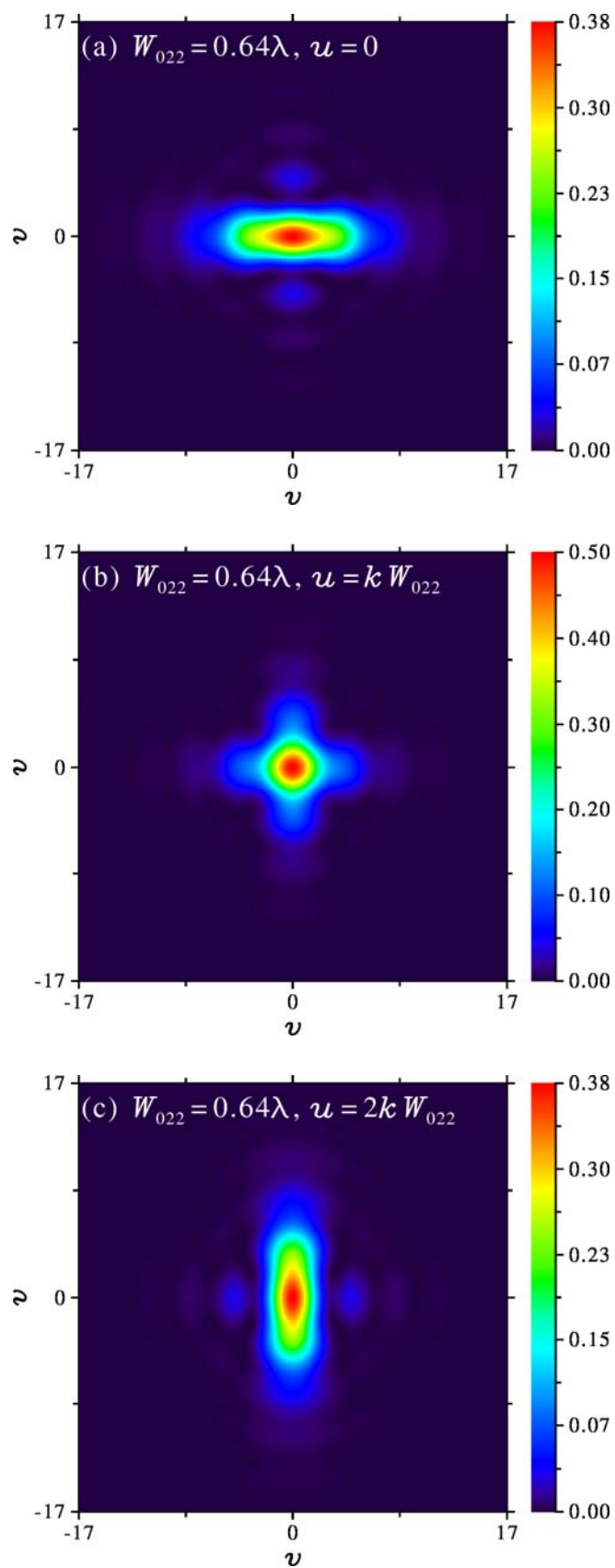
Fig. 1-11 Intensity distribution in the presence of primary astigmatism W_{221}=0.64 (a) at the sagittal focal plane; (b) $u=kW_{221}$ and (c) at tangential focal plane $u=2kW_{221}$.

1.2.3 Split lens

A split lens is proposed and used to generate desired focus shape near the focal region and therefore to manipulate a beam having particular propagation characteristic in the entire image space. Lens splitting can be implemented in many different ways, such as a configuration of Meslin's experiment or Billet's split lens [3]. Once a lens is split in multiple pieces, the resulting interference will involve multiple beams and the configuration of multiple paths, creating a relatively complex situation for beam propagation and interference.
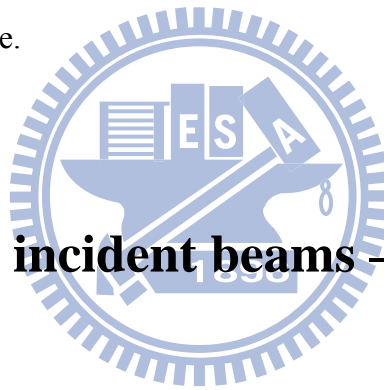
1.3   Revisit on incident beams – vector fields in an optical system

In an optical system with a large relative aperture, the polarization effect has been considered. For an aplanatic system illuminated by a linearly polarized incident beam, the diffracted electromagnetic fields by vector Debye theory are [4]

$$
\begin{aligned}
E_x &= -iB\left(L_0 + L_2 \cos 2\psi\right), \\
E_y &= -iB\left(L_2 \sin 2\psi\right), \\
E_z &= -iB\left(2L_1 \cos\psi\right),
\end{aligned}
\tag{1-22}
$$

The factor B is

$$B = \frac{\pi E_0 f}{\lambda}, \qquad (1\text{-}23)$$

and the L functions are defined as

$$L_0 = \int_0^\alpha \sqrt{\cos\theta} \sin\theta (1+\cos\theta) J_0(k\rho\sin\theta) \exp[ikz\cos\theta] d\theta, \qquad (1\text{-}24a)$$

$$L_1 = \int_0^\alpha \sqrt{\cos\theta} \sin^2\theta J_1(k\rho\sin\theta) \exp[ikz\cos\theta] d\theta, \qquad (1\text{-}24b)$$

$$L_2 = \int_0^\alpha \sqrt{\cos\theta} \sin\theta (1-\cos\theta) J_2(k\rho\sin\theta) \exp[ikz\cos\theta] d\theta \qquad (1\text{-}24c)$$

where $\alpha = \sin^{-1}(a/f)$.

For radially polarized illumination, the diffracted electromagnetic fields by vector

Debye theory are [6]

$$E_\rho = B\int_0^\alpha \sqrt{\cos\theta} \sin(2\theta) l(\theta) J_1(k\rho\sin\theta) \exp[ikz\cos\theta] d\theta,$$
$$E_\phi = 0, \qquad (1\text{-}25)$$
$$E_z = 2iB\int_0^\alpha \sqrt{\cos\theta} \sin^2\theta \, l(\theta) J_0(k\rho\sin\theta) \exp[ikz\cos\theta] d\theta.$$

For azimuthally polarized illumination, the diffracted electromagnetic fields by vector

Debye theory are [6]

$$E_\rho = 0,$$
$$E_\phi = 2B\int_0^\alpha \sqrt{\cos\theta} \sin\theta \, l(\theta) J_1(k\rho\sin\theta) \exp[ikz\cos\theta] d\theta, \qquad (1\text{-}26)$$
$$E_z = 0,$$

where $l(\theta) = \exp\left[-\beta_0^2\left(\frac{\sin\theta}{\sin\alpha}\right)^2\right] J_1\left(2\beta_0\frac{\sin\theta}{\sin\alpha}\right)$ and β_0 is the ratio of the pupil

radius and the beam waist. It is taken as 3/2 in the numerical simulations.

The time-averaged electric and magnetic energy densities for the diffracted fields are

defined as $W_e \equiv \dfrac{1}{16\pi} \langle \mathbf{E} \cdot \mathbf{E} * \rangle$.

Fig. 1-12 shows the intensity distribution of three components of electric fields at the

focal plane by linearly polarized (along the *x*-axis) illumination with NA=0.866 and

the focal length *f*=30,000*λ*. The intensity distribution in the left column shows by

linear scaling and in the right column displays with the logarithmic scaling. The z

component shows clearly an oscillating electric dipole.
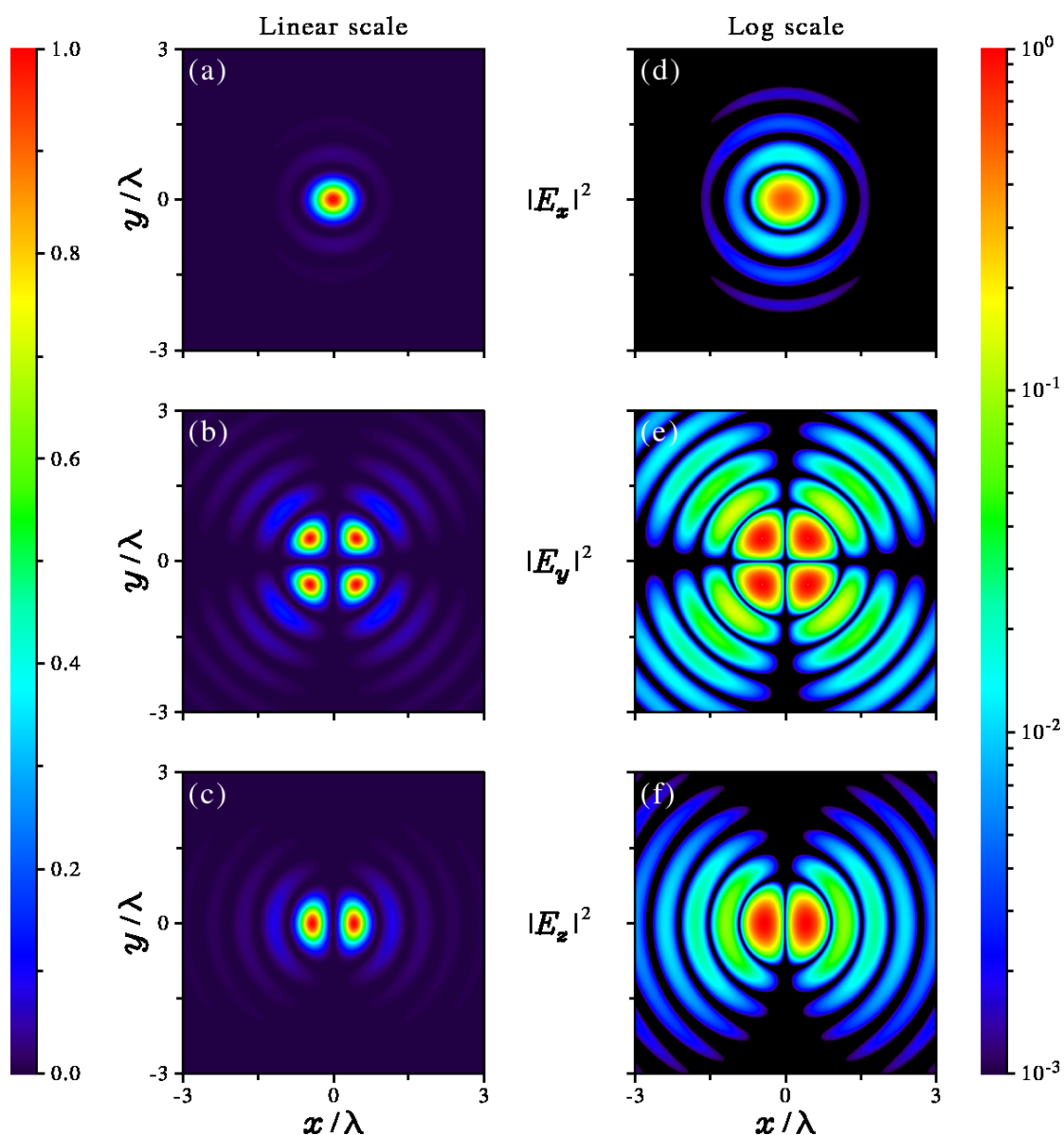
Fig. 1-12 Intensity distribution at the focal plane of an aplanatic lens with NA=0.866 and focal length f=30,000λ, illuminated by a linearly polarized plane wave. Frames (a)-(c) display the intensity plot with linear scaling, while frames (d)-(f) show the intensity distribution with logarithm scaling. The peak intensities in (a), (b), (c) are in the ratios 1.0:0.0036:0.13, respectively.
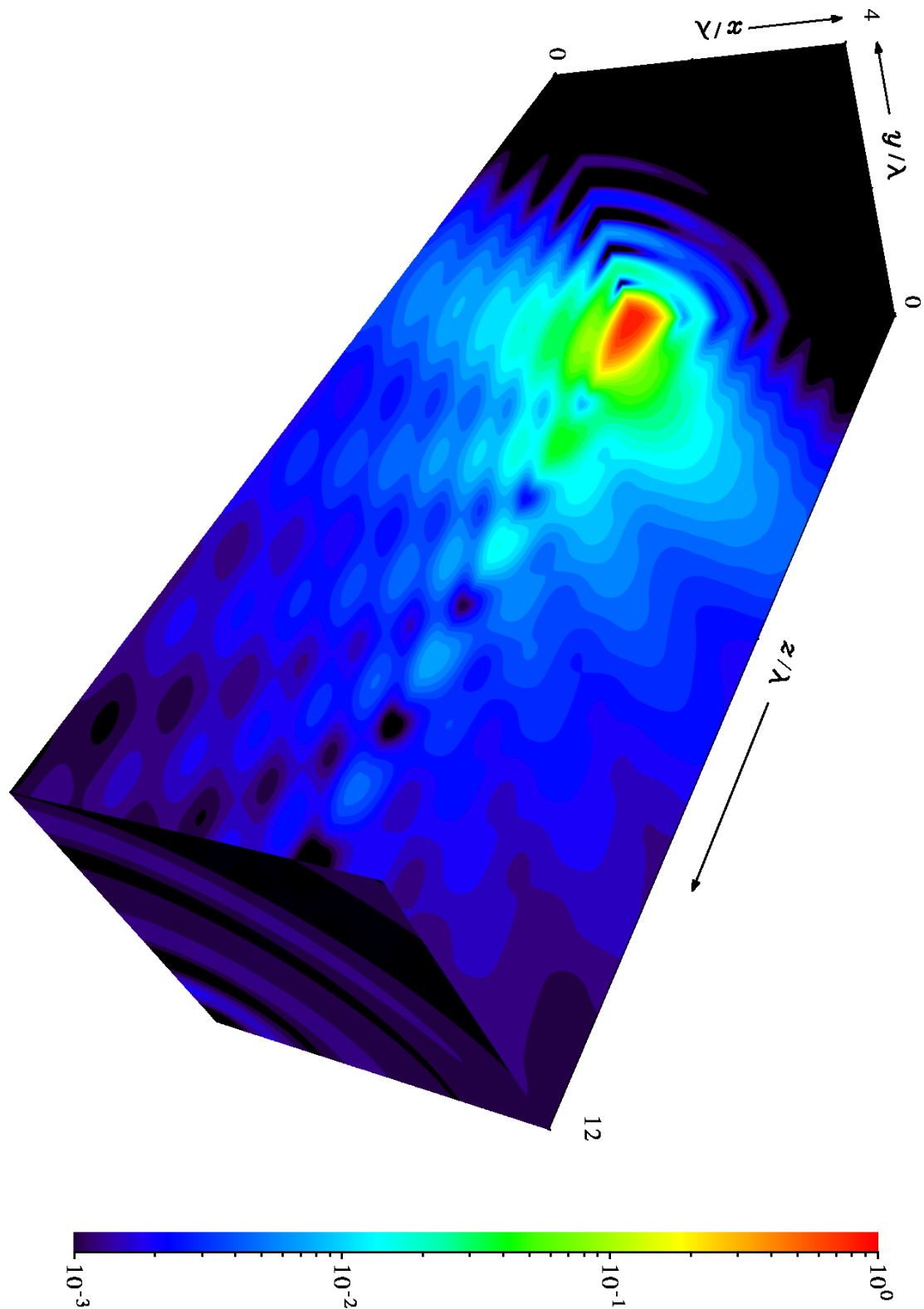
Fig. 1-13 The electric energy density near the focal region of an aplanatic lens with NA=0.866 and focal length f=30,000λ, illuminated by a linearly polarized plane wave. The logarithmic scaling is used here.

Fig. 1-13 shows the electric energy density in the image space near the focus by slicing the *XZ*- and *YZ*-planes together with the *XY*-plane at the focus and $z=12\lambda$. The logarithmic scaling is used here. The electric energy density is not rotationally symmetric about the optical axis because of the bending of the polarization is clearly observed. The diverging characteristic beyond the focus can also be seen.

Fig. 1-14 shows the intensity distribution of two components of electric fields at the focal plane with radially polarized illumination with NA=0.866 and the focal length $f=30,000\lambda$. The intensity distribution in the left column shows by linear scaling and in the right column displays with the logarithmic scaling. Fig. 1-15 shows the electric energy density in the image space near the focus by slicing the *XZ*- and *YZ*-planes together with the *XY*-plane at the focus and $z=18\lambda$. The logarithmic scaling is used here. The electric energy density is rotationally symmetric about the optical axis can be clearly observed. The diverging characteristic beyond the focus can also be seen.

Fig. 1-16 shows the intensity distribution of two components of electric fields at the focal plane with azimuthally polarized illumination with NA=0.866 and the focal length $f=30,000\lambda$. The intensity distribution in the left column shows by linear scaling and in the right column displays with the logarithmic scaling. Fig. 1-17 shows the electric energy density in the image space near the focus by slicing the *XZ*- and *YZ*-planes together with the *XY*-plane at the focus and $z=18\lambda$. The logarithmic scaling

is used here. The electric energy density is rotationally symmetric about the optical

axis can be clearly observed. The diverging characteristic beyond the focus can also

be seen.
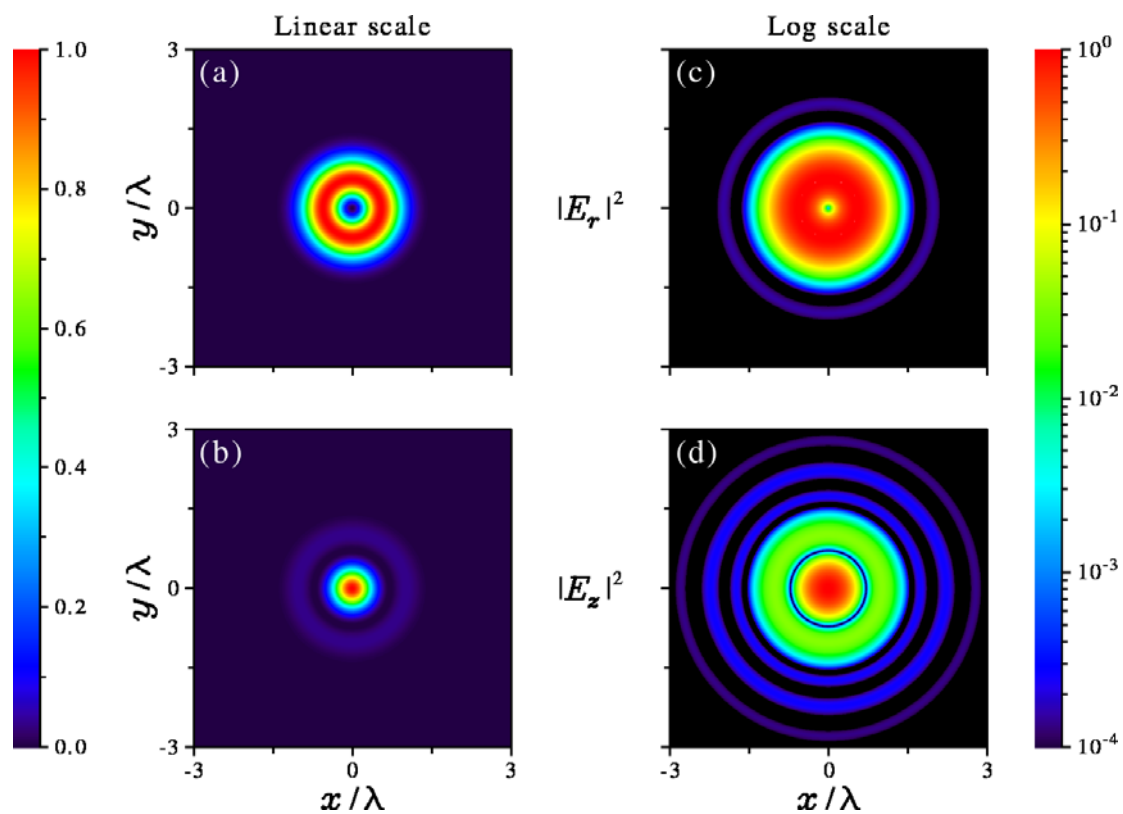
Fig. 1-14 Intensity distribution at the focal plane of an aplanatic lens with NA=0.866 and focal length f=30,000λ, illuminated by a radially polarized plane wave. Frames (a)-(b) display the intensity plot with linear scaling, while frames (c)-(d) show the intensity distribution with logarithm scaling. The peak intensities in (a), (b) are in the ratios 0.73:1.0, respectively.
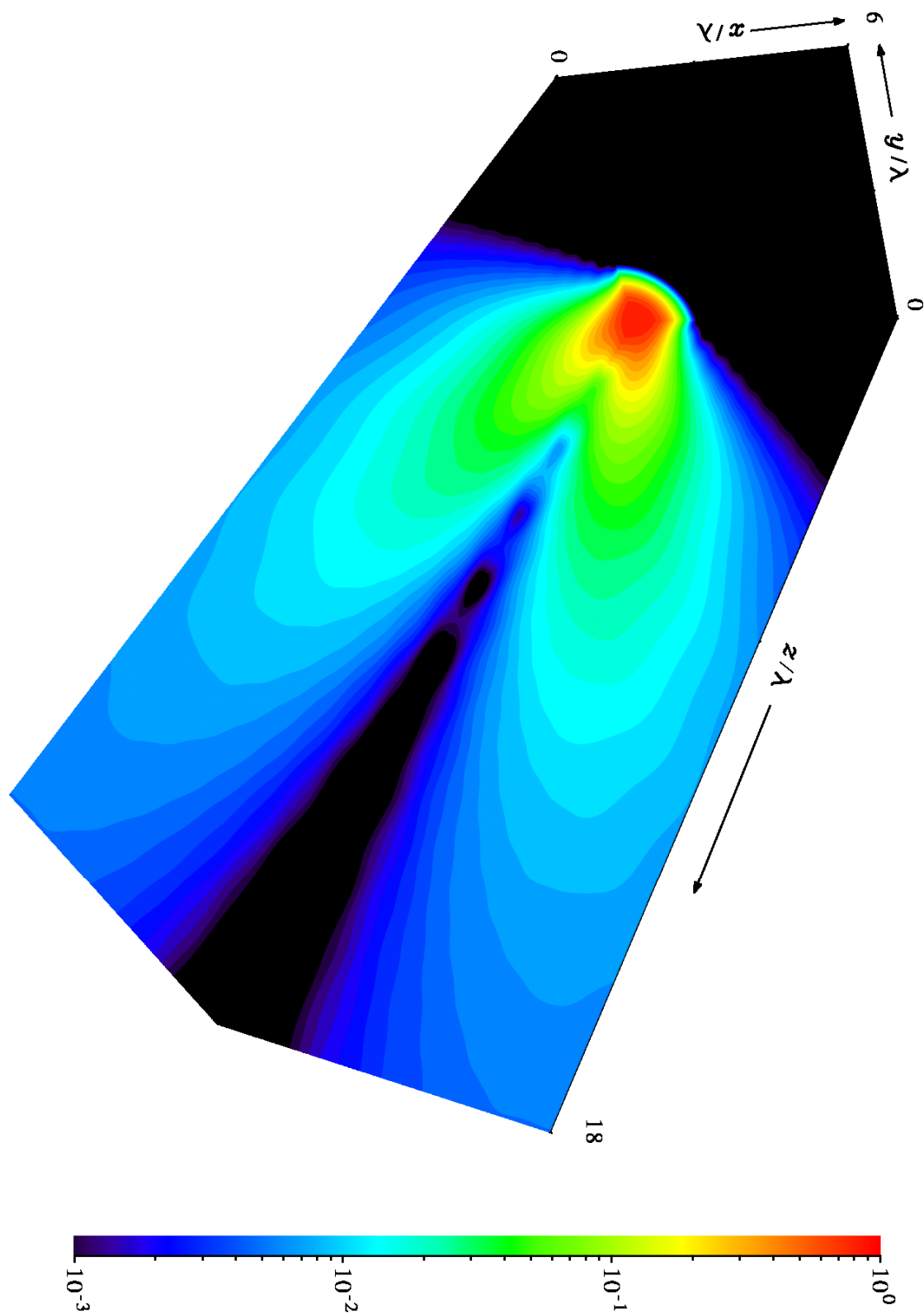
Fig. 1-15 The electric energy density near the focal region of an aplanatic lens with NA=0.866 and focal length f=30,000λ, illuminated by a radially polarized Bessel-Gauss wave. The logarithmic scaling is used here.
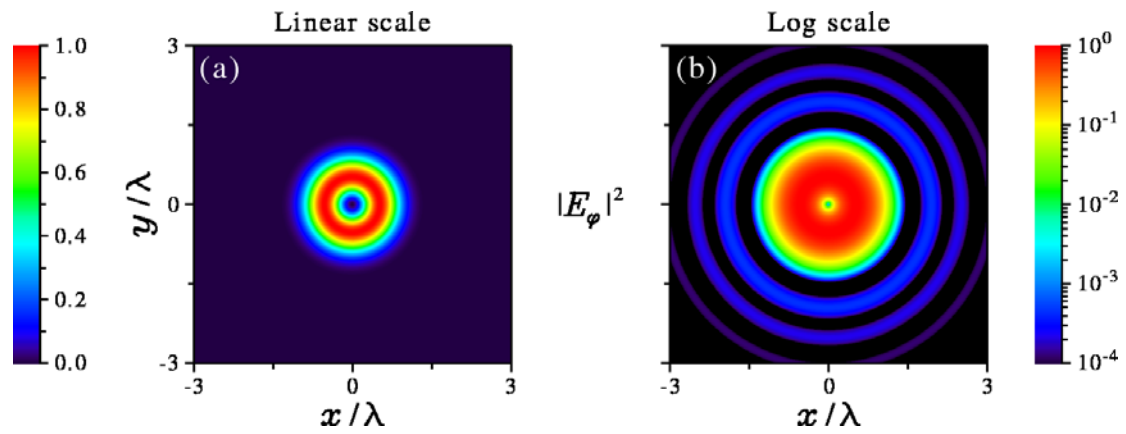
Fig. 1-16 Intensity distribution at the focal plane of an aplanatic lens with NA=0.866 and focal length f=30,000λ, illuminated by an azimuthally polarized plane wave. Frame (a) displays the intensity plot with linear scaling, while frame (b) shows the intensity distribution with logarithm scaling.
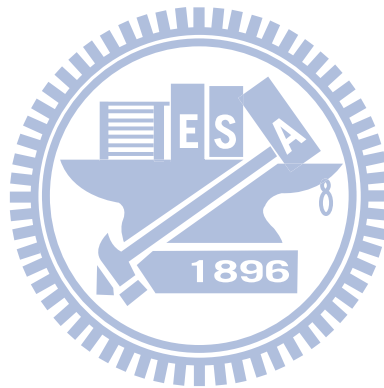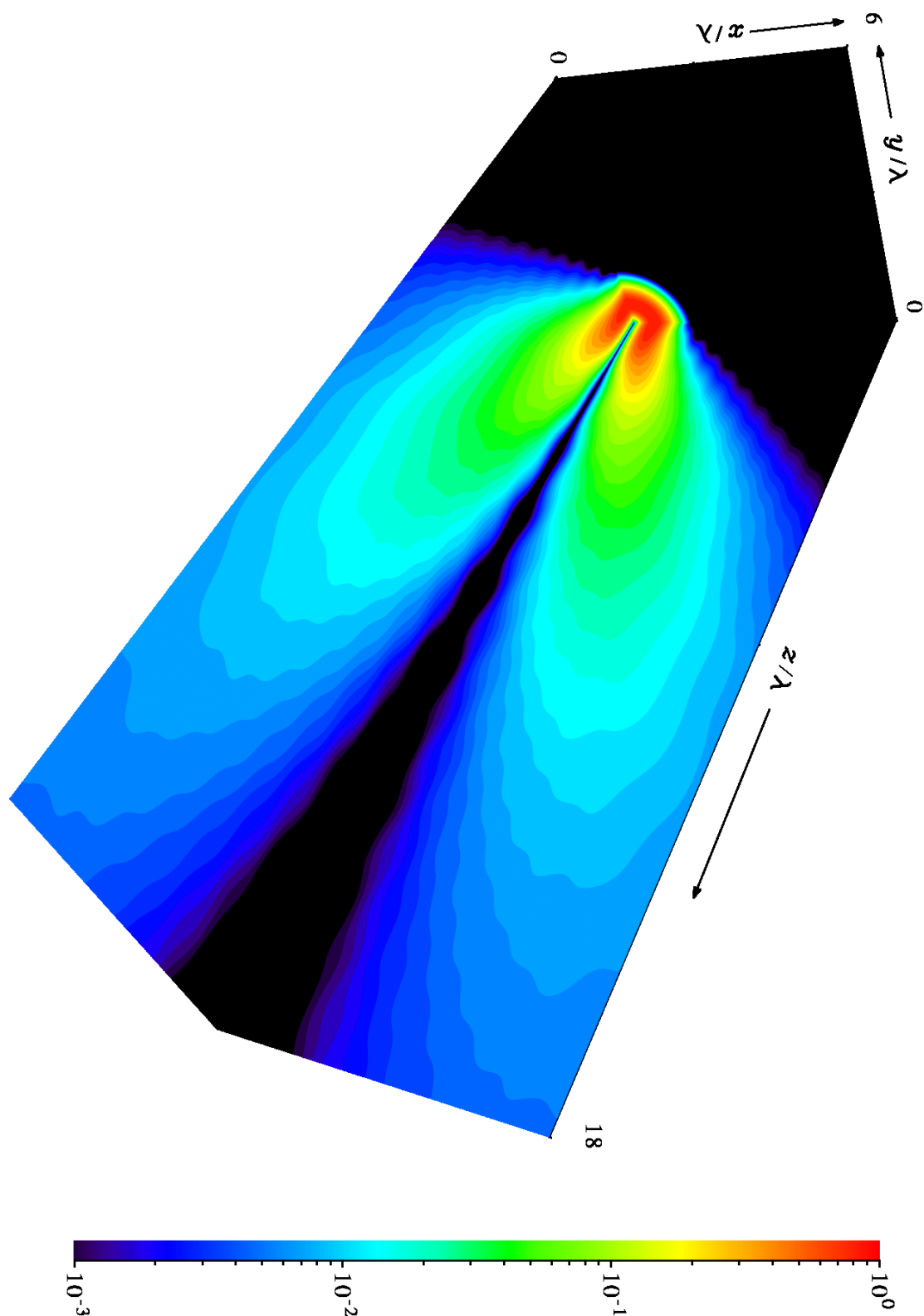
Fig. 1-17 The electric energy density near the focal region of an aplanatic lens with NA=0.866 and focal length *f*=30,000λ, illuminated by an azimuthally polarized Bessel-Gauss wave. The logarithmic scaling is used here.

1.4   Organization of this dissertation

This dissertation is organized as follow. The split lenses are studied in Chapter 2 and

Chapter 3 in terms of the transversal and longitudinal arrangement of foci,

respectively. In Chapter 2, the transversal arrangement i.e., Billet's N-split lens, is

discussed and focused on the symmetry properties of the interference patterns. The

longitudinal arrangement of foci i.e., Meslin's N-split lens is studied in Chapter 3 for

the symmetry properties of field distribution. The Quasi J_0 Bessel beam generated by

Billet's N-split lens is investigated in Chapter 4 by the numerical simulations and the

asymptotic solution. In Chapter 5, The focal shifts has been investigated by the

application of the vector Kirchhoff diffraction theory on vector beams including

linearly, radially and azimuthally polarization. A comparison has also made among

these three vector beams. Finally we draw our conclusions and future works in

Chapter 6.

2

Transversal foci: Billet's *N*-split lens

2.1 Introduction

This chapter discusses a split having transversal foci arrangement where the focal points of sectors locating in the same plane, the original focal plane and therefore the interference pattern varies with the number of sectors of the split lens. First, we revisit the original Billet's split lens where there are two foci located either in the *X*- or *Y*-axes and there are two kinds of interference pattern in the *XY*-plane can be observed in the far field away from the focal plane. One is the straight line and the other is the hyperbolas. The interference pattern of equidistant straight lines are running perpendicular to the connection line of two foci and the interference pattern of hyperbolas are the cross section of the hyperboloids of revolution having the two focal points as common foci. In the Billet's *N*-split lens, we cut a conventional lens into *N* sectors and placing the focal points of sectors on a circle. Note that the arrangement of sectors foci is not restricted to a circle only. The interference pattern of hyperbolas lies between two adjacent equidistant straight lines and having a radian of π/N. This type of lens splitting selected causes both the interference patterns of
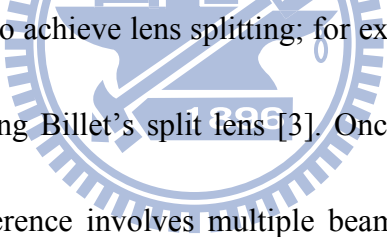
equidistant straight lines and of hyperbolas in the original Billet's lens to form an

N-fold angularly distributed pattern with an angle difference of $2\pi/N$. For an odd

number of splitting N, there is an additional angle shift of π/N for the azimuthally

distributed patterns of equidistant straight lines and hyperbolas. Moreover, there is an

N-peak interference pattern near the optical axis, resembling a concentric-circle-like

interference, can be readily observed when N is large as a result of N-beam

interference.

The study of field propagation and its associated diffraction behavior is a

classical topic in optics research [7]. Previous studies show that this topic has many

important applications in optical testing [8] and the development of new optical

devices using nano-technology [9]. The current design approach for creating optical

products is still primarily based on ray optics, while diffraction-based theory generally

provides a reference and base line of resolution and performance limitations.

Nevertheless, the diffraction theory of optical fields remains an important research

topic. Researchers continue to make active progress in this area, as indicated by the

selected works of E. Wolf [10]. In viewing the demands of technology development

and academic interest, Chu and Chern are dedicated to exploring far-field behavior

with sub-wavelength variations, where aperture (stop) plays a key role in information

retrieval [11]. In existing literature, the aperture stop (circular and rectangular) and

perfect lens are classical platforms for exploring diffraction behavior. Studies on this

topic generally fall into one of two categories:

(1) Light sources could be different, e.g., a cylindrical beam or a vector polarized

    beam.

(2) The lens can have aberrations, e.g., defocus, spherical aberration, coma and

    astigmatism.

The current study considers a different approach that may be able to provide an

additional basic reference for diffraction study, namely the generalized form of a split

lens.

There are many ways to achieve lens splitting; for example, in a configuration of

Meslin's experiment or using Billet's split lens [3]. Once a lens is split in multiple

pieces, the resulting interference involves multiple beams and the configuration of

multiple paths. This creates complicated beam propagation and interference.

Nevertheless, if this generalization is implemented symmetrically, the field

distribution exhibits an embedded symmetry, which reduces and simplifies the

complexity of analysis and calculation. Thus, exploring the diffraction behavior with

such a generalization, particularly the symmetry properties, is worthy of further

research. Therefore, this study presents such a generalization of Billet's split lens.

Note that previous research has developed such a Billet's split lens for multiple

imaging and multichannel optical processing [12].

2.2 Symmetry properties

The bottom of Fig. 2-1 shows a schematic diagram of Billet's split bi-sector lens,

where a conventional focusing lens is split into two identical halves (two sectors). The

upper half and the lower half are then moved a distance d up and down the Y-axis,

respectively. This split lens creates a collimated uniform monochromatic wave with a

wavelength of λ for two different foci, F_1 and F_2, in the focal plane. The diffraction

theory applied here assumes that the aperture radius $a \gg \lambda$, the focal length $f \gg a \gg$

λ, and the Fresnel number $a^2/\lambda f$ is much larger than unity. When the (half) translation

length d is zero, the two foci will coincide and the integral representation of the

disturbance $U(P)$ at a point $P(x,y,z)$ in the image space is [3]

$$U(P) = -\frac{i}{\lambda}\frac{a^2 A}{f^2}e^{i(\frac{f}{a})^2 u}\int_0^1\int_0^{2\pi} e^{-i\left[v\rho\cos(\theta-\psi)+\frac{1}{2}u\rho^2\right]}\rho\,d\rho\,d\theta\,, \qquad (2\text{-}1)$$

where the optical units u, v, and ψ represent the Cartesian coordinate positions of P (x,

y, z). These values are $u=\dfrac{2\pi}{\lambda}\left(\dfrac{a}{f}\right)^2 z$, $v=\dfrac{2\pi}{\lambda}\left(\dfrac{a}{f}\right)r=\dfrac{2\pi}{\lambda}\left(\dfrac{a}{f}\right)\sqrt{x^2+y^2}$, where

$x = r \cos \psi$ and $y = r \sin \psi$. Fig. 2-2 shows the coordinate system. The disturbance

$U(P)$ is

$$U(P) = C \int_0^1 e^{-i\frac{1}{2}u\rho^2} \int_0^{2\pi} e^{-i\left[\frac{2\pi}{\lambda}\frac{a}{f}\rho[x\cos\theta + y\sin\theta]\right]} d\theta \rho d\rho , \qquad (2\text{-}2)$$

where $C = -\frac{i}{\lambda}\frac{a^2 A}{f^2} e^{i(\frac{f}{a})^2 u}$.
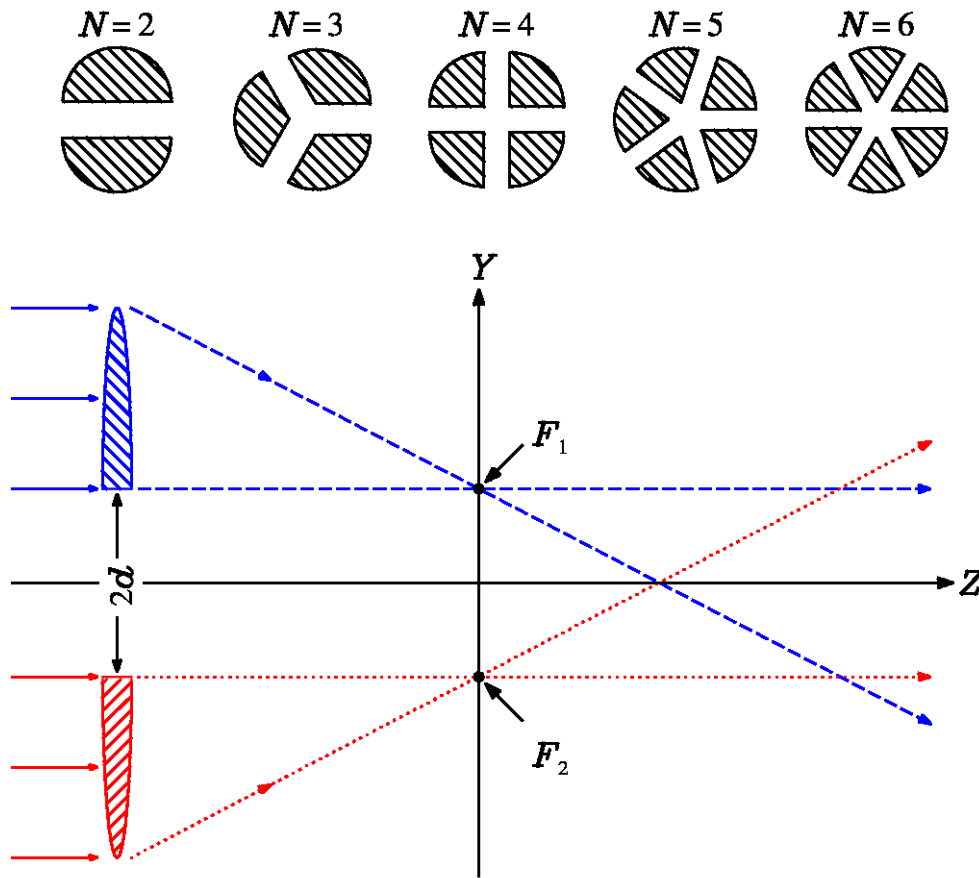
Fig. 2-1 **Top**: Front view from the left side, showing the arrangements of sectors when
N=2, 3, 4, 5, and 6, where N is the number of sectors. **Bottom**: Schematic diagram of
Billet split bi-sector lens. F_1 and F_2 are the first focus and second focus, respectively,
and 2d is the separation distance between the foci of the two sectors.

To generalize lens splitting, a focusing lens is divided into N equiangular

sectors. Each sector is exploded and translated a distance d in the r direction along the

perpendicular bisector of the angle. Fig. 2-1 shows the schematic layouts of the

simplest cases of N=2, 3, 4, 5, and 6. Ray-based analysis shows that the foci of all

sectors constitute a regular N-sided polygon in the focal plane. Therefore, the focal

point of each sector is

$$
\begin{aligned}
x_m &= d\cos\psi_m, \\
y_m &= d\sin\psi_m, \\
\psi_m &= \frac{2\pi}{N}(m+1/2), \quad m=0,1,..,N-1
\end{aligned}
\tag{2-3}
$$
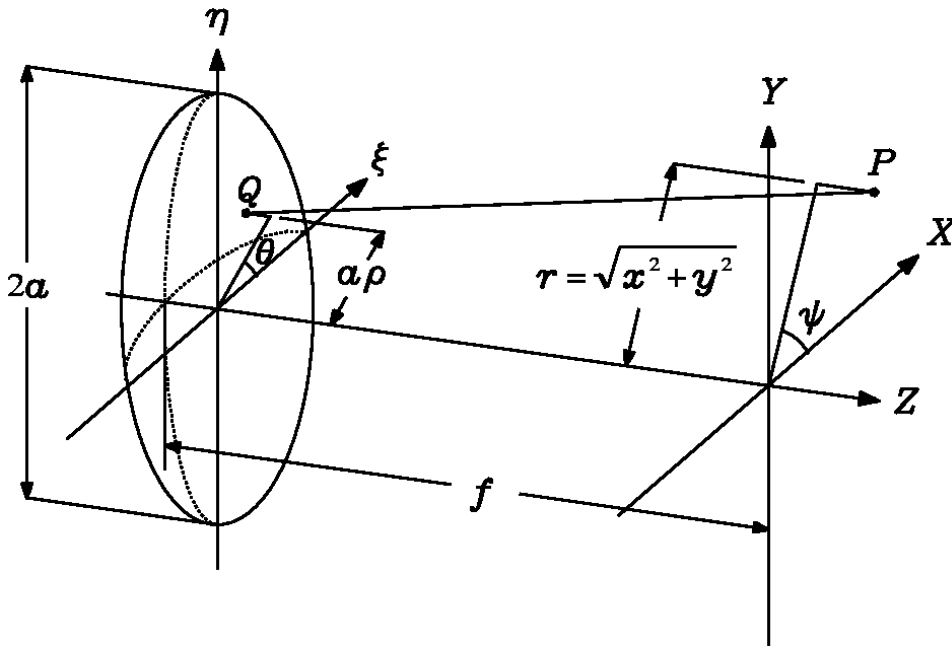
Fig. 2-2 Notation representation of the coordinate system of beam propagation.

By applying coordinate translation and summing the contributions from all sectors,

the disturbance $U(P)$ is

$$
U(P)=C\int_0^1 e^{-i\frac{1}{2}u\rho^2}\sum_{m=0}^{N-1}\int_{m\frac{2\pi}{N}}^{(m+1)\frac{2\pi}{N}} e^{-i\left[\frac{2\pi}{\lambda}\frac{a}{f}\rho[(x-x_m)\cos\theta+(y-y_m)\sin\theta]\right]}d\theta\rho d\rho,
\tag{2-4}
$$

Substituting Eq. (2-3) into Eq. (2-4) leads to

$$U(P) = C\int_0^1 e^{-i\frac{1}{2}u\rho^2} \sum_{m=0}^{N-1} \int_{m\frac{2\pi}{N}}^{(m+1)\frac{2\pi}{N}} e^{-i\left\{\frac{2\pi}{\lambda}\frac{a}{f}\rho[r\cos(\theta-\psi)-d\cos(\theta-\psi_m)]\right\}} d\theta\rho d\rho \qquad (2\text{-}5)$$

We can change the interval of integration for each segment to be the same value from

0 to $2\pi/N$ and the disturbance is

$$U(P) = C\int_0^1 e^{-i\frac{1}{2}u\rho^2} \sum_{m=0}^{N-1} \int_0^{\frac{2\pi}{N}} e^{-i\left\{\frac{2\pi}{\lambda}\frac{a}{f}\rho\left[r\cos\left(\theta+m\frac{2\pi}{N}-\psi\right)-d\cos\left(\theta+m\frac{2\pi}{N}-\psi_m\right)\right]\right\}} d\theta\rho d\rho \qquad (2\text{-}6)$$

After substituting Eq. (2-3) into Eq. (2-6), the d term in the brackets of exponential

function is no longer a function of m. The summation can be put into the integrand of

r term only, i.e.,

$$U(P) = C\int_0^1 e^{-i\frac{1}{2}u\rho^2} \int_0^{\frac{2\pi}{N}} e^{iv_d\rho\cos\left(\theta-\frac{\pi}{N}\right)} \times \sum_{m=0}^{N-1} e^{-iv\rho\cos\left(\theta-\psi+m\frac{2\pi}{N}\right)} d\theta\rho d\rho, \qquad (2\text{-}7)$$

where $v_d = \frac{2\pi}{\lambda}\left(\frac{a}{f}\right)d$. Now, the azimuthally symmetrical property at a specific z

plane with respect to the optical axis is

$$U(u,v,\psi-\frac{2\pi}{N}) = U(u,v,\psi), \qquad (2\text{-}8)$$

This shows that a disturbance on a specified z plane is rotationally symmetrical with

an angle of $2\pi/N$. In other words, the disturbance repeats itself every $2\pi/N$ along the

azimuthal direction, and hence, an *N*-fold rotational symmetry originates from the symmetry in the split form in the lens.

2.3   Billet's *N*-split lens

The light distributions of Billet's *N*-split lens are explored by using numerical simulations. To fulfill the condition of diffraction beam, i.e., the numerical aperture should be around 0.1, we used a typical lens with a focal length of a few ten mm, e.g., *f*=30,000*λ*, to create an aperture radius *a*=3,000*λ*. This lens also has the (half) separation distance *d*=100*λ*. For the numerical example of *λ*=630 *nm,* these settings lead to *f*=18.9*mm, a*=1.89*mm,* and *d*=0.063*mm.* The plot of intensity distributions was normalized to 100. As a base reference, we revisited the classical Billet spilt lens, i.e., *N*=2. After the focal plane, the interference pattern in the *XY*-plane formed within the overlap region lit by two sectors. The intensity distribution in Fig. 2-3(a) reflects this result, clearly showing a two-fold symmetry [3]. The diffraction pattern contributed from each sector beyond the focal plane is similar to the original half sector, but rotated *π* radians around the new translated axis. This new translated axis is parallel to the optical axis throughout the focus of each sector. The lights from the two semicircles form an overlapped region near the optical axis and create interference. The interference patterns, therefore, are equidistant straight lines parallel to the lines

that cut the spherical wavefront into two hemispheres, and are perpendicular to the

line through two focal points F_1 and F_2. On the other hand, the diffraction patterns

outside the overlapped region lit by two sectors are hyperbolas, which are sections of

hyperboloids of revolution about the F_1F_2 axis and have F_1 and F_2 as common foci

[3].
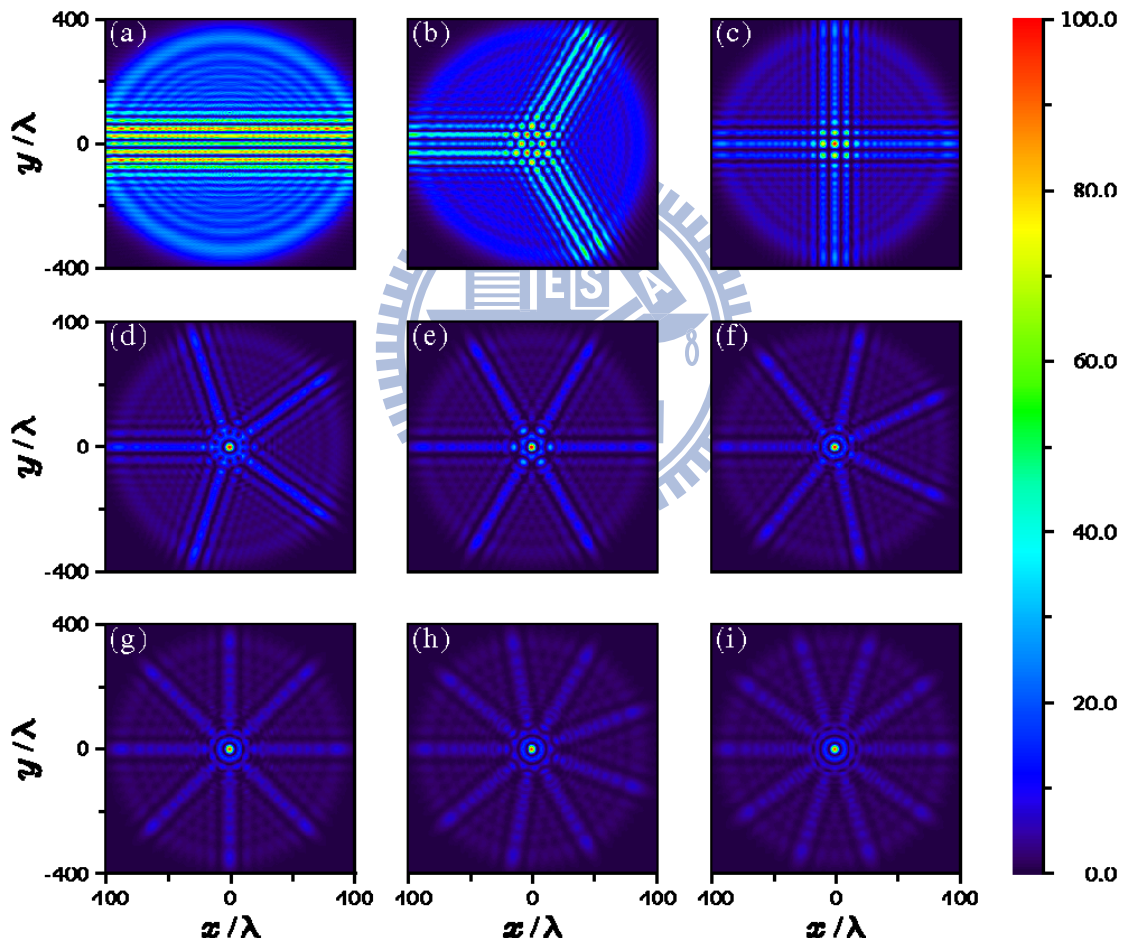
Fig. 2-3 Density plot of normalized intensity distribution of the generalized N-split lens in the XY-plane at $z=5000\lambda$ where (a) N=2, (b) N=3, (c) N=4, (d) N=5, (e) N=6, (f) N=7, (g) N=8, (h) N=9, and (i) N=10.

2.3.1 Interference pattern of straight lines

To identify how splitting a lens changes the intensity distribution, this study evaluates

the distributions for $N=2$ to $N=10$ in the far field (here, $z=5000\lambda=3.15$mm, if

$\lambda=630$nm). Fig. 2-3(b) shows that a 3-fold symmetry is readily apparent when $N=3$.

However, the fringes of hyperbolas must have near $2\pi/3$ radians, instead of π radians

in the case of $N=2$. In the case of $N=2$, they are in the opposite direction of the

equidistant straight lines, and the fringes of equidistant straight lines in the *XY*-plane

appear inside the overlap region lit by each two sectors. On the other hand, for the

case of $N=3$, there are three distinct straight-line fringes that are parallel to three lines

located at the angles of $\pi/3$, π, and $5\pi/3$, respectively. Nevertheless, these three lines

do not coincide with the lines of sector division, but rotate an additional angle of $\pi/3$

around the optical axis. This is because the diffraction pattern of each sector (beyond

the focal plane) rotates π radians around each translated axis parallel to optical axis

through the focus of each sector. In addition, the two straight cutting edges of each

sector also rotate by π radians, and therefore interfere with each other after a rotation

of the azimuthal angle of π. When N is odd, the rotation prevents the interference

pattern of each straight line from coinciding with the original cutting edge of each

sector, and all fringes of straight lines resemble an angle of rotation of π/N-radian

(mod 2π) around the optical axis. When N is even, the rotation of the azimuthal angle

of π also shifts the interference pattern of straight line π radians, but the rotated

interference pattern of straight lines coincides with the original cutting edge of other

sectors due to reflection symmetry between the *X*- and *Y*-axes. Under these

circumstances, all straight line fringes look like they have not rotated, and remain

located within the cutting edge of each sector. Similarly, the interference pattern of

equidistant straight lines by an *N*-split lens is oriented at the angle of $m{\cdot}2\pi/N$ when *N*

is an even number but for the case of odd-number lens splitting, the interference

pattern is at the angle of $\pi/N + m{\cdot}2\pi/N$, which requires an additional angle shift of

π/N.
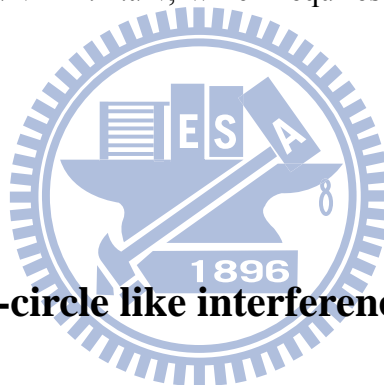
2.3.2   Concentric-circle like interference pattern

Next, consider the central region of intensity distribution near the optical axis. Fig.

2-3 indicates that as *N* becomes larger, the intensity distribution centered on a

specified location along the optical axis begins to resemble a concentric-circle-like

interference pattern, while for a small *N*, the distribution is more like a regular

N-sided polygon. This polygon basically represents the split distance *d*, i.e., the

circumradius is limited by *d*. The intensity distribution in the central region involves

multiple-beam interference, i.e., all sectors contribute to the total field. However, only

the beam interference of two sectors, i.e., the overlap of the field from two sectors

causes the straight-line-like interference pattern in the outward azimuthal regime. For

example, consider the case of N=12, where Fig. 2-4(b) plots the far-field intensity

distribution (z=5000λ for simplification). The central regime contains

concentric-circle-like interference patterns. The second bright ring actually has twelve

peaks, and each of which is located along the azimuthal direction with an angle

difference of π/6. However, the difference between the minimum and maximum

intensity of the second bright ring is too small to identify in Fig. 2-4(b). Therefore,

Fig. 2-4(c) presents an enlargement of Fig. 2-4(b). Here, the peak distributions are

readily apparent in the inner rings, and twelve peaks clearly appear in the second and

fourth bright rings. From the symmetrical properties deduced above, numerical

simulation reveal that the distance between two successive peaks is $\sim d\cos(\pi/12)$

$\sim$0.122mm, if λ=630nm, where the peak location is defined according to the maximum,

even at such a far-field distance. Numerical simulations also show that as N becomes

larger, the concentric-circle-like interference patterns inside the region of

circumscribed circle become significant at various XY-planes, i.e., at any specified

locations along the optical axis, provided that the interference occurs after the focal

plane. However, the symmetry properties deduced above remain the same.
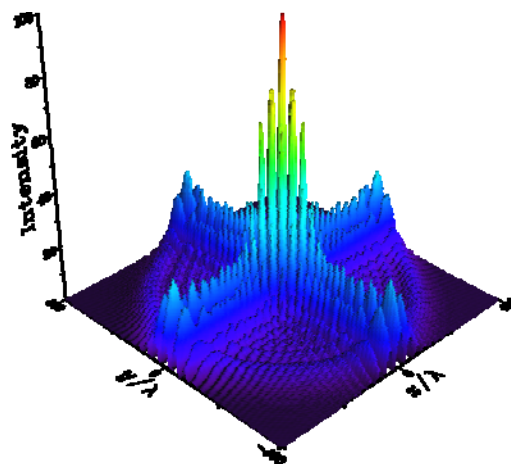
(a)
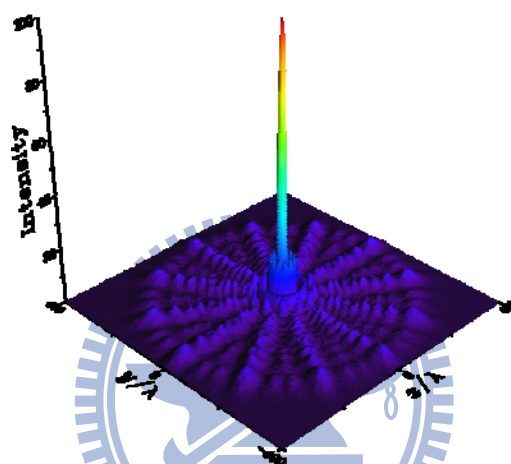
(b)
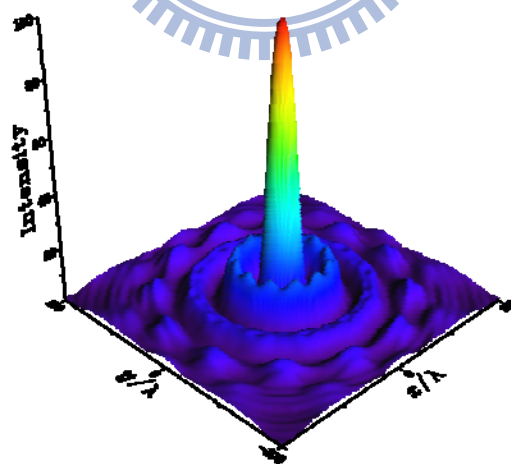
(c)

Fig. 2-4 Normalized intensity distribution of the generalized *N*-split lens in the *XY*-plane at *z*=5000*λ* where (a) *N*=4, (b) *N*=12, and (c) Enlargement of (b).

2.4 Summary

In summary, the diffraction behavior of a generalized Billet's N-split lens has been derived based on symmetry consideration. The intensity distributions vary significantly as the number of split sectors increases, particularly compared with the original Billet's split lens. Nevertheless, there is a symmetry relationship embedded in this class of split lenses. Due to lens-splitting form adopted in this study, the intensity distribution has an N-fold rotational symmetry with respect to the optical axis in the XY-plane. The interference patterns of equidistant straight lines are orientated at the angle of $m \cdot 2\pi/N$ when N is even, but at the angle of $\pi/N + m \cdot 2\pi/N$ when N is odd, where m=0, 1, 2,…, N-1. In other words, there are two kinds of symmetry even though the corresponding splitting operation is simple. The interference of the disturbance by two adjacent sectors of the split lens is the physical origin of the fringes of equidistant straight lines. In addition, this symmetrical property is physically traceable based on the symmetry embedded in the splitting form of lens.

A concentric-circle-like interference pattern near the optical axis appears when N is larger than 10. This feature is primarily due to multiple-beam interference. The multiple-beam interference inside the inner regime forms a polygon boundary of intensity distribution in which the distance between two successive maximum peaks

is $\sim d\cos(\pi/N)$. When the number of sectors in split lens becomes very large, the

polygon nearly becomes a circle.

Note that the symmetry embedded within the generalized split lens and the

straight-line provide two basic guidelines for forming the azimuthal light distribution

while the central regime hosts a concentric-like distribution. Practically, the proposed

approach to the generalized split lens provides more means of controlling light beams.

Though this study is limited to Billet's split lens, different symmetrical forms in lens

splitting will lead to different kinds of light distribution. It is also possible to

implement this generalized Billet's N-split lens with liquid crystal, i.e., a

segmented-aperture optical system in which phase-shifting material, here liquid

crystal, fills each segmented region [13-14].
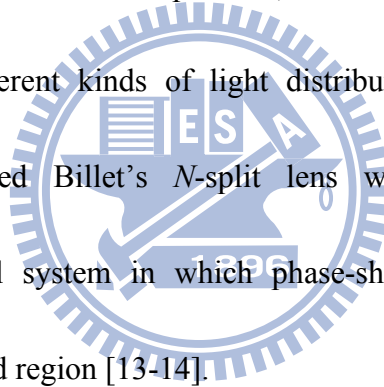
3

Longitudinal foci: Meslin's *N*-split lens

3.1 Introduction

In previous chapter, we have studied the generalization in Billet's configureation of split lens where the focal points are distributed in a *XY*-plane especially in a circular shape. Here we would like to consider a different approach which should be able to provide additional reference for the diffraction study of a split lens. In this chapter, we present our result of such a generalization in Meslin's configuration of split lens where the focal points are distributed along the optical axis. Typically, the lens splitting could be implemented in many different ways as may be referenced in the literatures of multiple-beam interference and interferometry [6,7]. We, however, focus on the characteristics of focal point which is the key of identification in considering beam propagation. It is worthwhile to note that the corresponding distributions of focal points in classical Meslin's experiment and Billet's split lens [6]. For Meslin's experiment, the two focal points are along the optical axis, while for Billet's split lens, the two focal points are located vertically, i.e., on a plane normal to the optical axis. In other words, it is possible that by successive lens splitting, the lens becomes a

special lenslet array and the distribution of focal points becomes a line either along

the optical axis or on a plane that is normal to the optical axis.

It could be understood that once lens is split in multiple pieces, the incident beam

will be separated into multiple beams in a multiple configurations of path, which

result in a quite complicated situation in beam propagation and interference pattern.

Nevertheless, if the generalization is implemented with symmetry, the field

distribution is expecting to exhibit the embedded symmetry, and hence the complexity

of analysis may be reduced and the calculation could be simplified. As an academic

exploration, it should be worthwhile to investigate the diffraction behavior with such

a generalization, particularly the symmetrical property. In this chapter, we present our

result of such a generalization in Meslin's configuration of split lens where the focal

points are distributed along the optical axis, the longitudinal arrangement of foci.

3.2   Theoretical formalism

Referring to Fig. 3-1(a), the notation of the coordinate system for the beam

propagation with a perfect lens is provided. The perfect lens, having focal length f and

aperture radius a, brings a collimated uniform monochromatic wave of wavelength λ

to the image space. If $f \gg a \gg \lambda$, and if, in addition, the Fresnel number $a^2/\lambda f$ is

much larger than unity, the Debye integral, will give a good approximation of the

disturbance $U(P)$ at the point $P(x,y,z)$ in image space which follows [3]

$$U(P) = -\frac{i}{\lambda}\frac{a^2 A}{f^2} e^{i(\frac{f}{a})^2 u} \int_0^1 \int_0^{2\pi} e^{-i\left[v\rho\cos(\theta-\psi)+\frac{1}{2}u\rho^2\right]} \rho\,d\rho\,d\theta ,$$ (3-1)

where A is the amplitude of incident beam, and the optical units u and v together with

azimuthal angle ψ are used to specify the location, i.e., $u = \frac{2\pi}{\lambda}\left(\frac{a}{f}\right)^2 z$ and

$v = \frac{2\pi}{\lambda}\left(\frac{a}{f}\right)r = \frac{2\pi}{\lambda}\left(\frac{a}{f}\right)\sqrt{x^2+y^2}$. The disturbance $U(P)$ has a symmetric property,

i.e., $U(-u,v,\psi+\pi) = -[U(u,v,\psi)]^*$ or $U(-u,v,\psi) = -[U(u,v,\psi)]^*$ because of rotational

symmetry, where * is the complex conjugate as shown by Collett and Wolf [15]. It

can be readily shown that the symmetric properties of amplitude and the phase Φ

are

$$|U(-u,v,\psi)| = |U(u,v,\psi)| \text{ and } \Phi(-u,v,\psi) = -\Phi(u,v,\psi) - \pi .$$ (3-2)

The amplitude (intensity) has a symmetry of reflection about the focal plane $z=0$,

while the phase has reflection anti-symmetry, apart from an additive factor π.
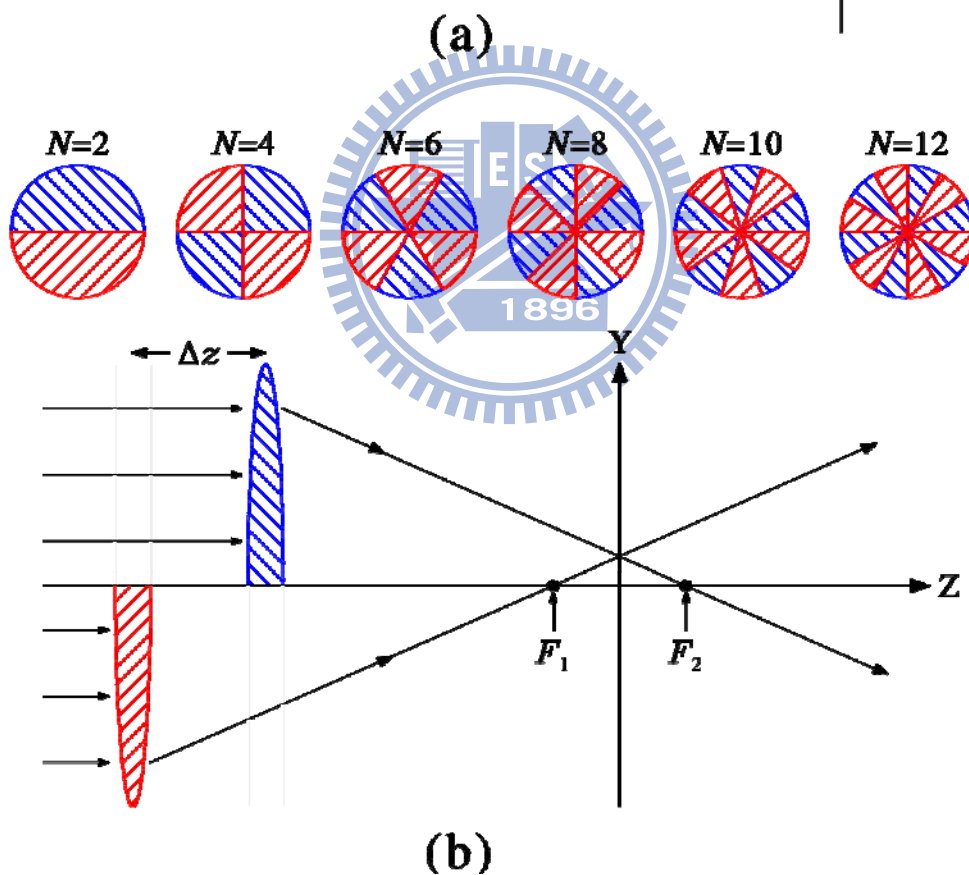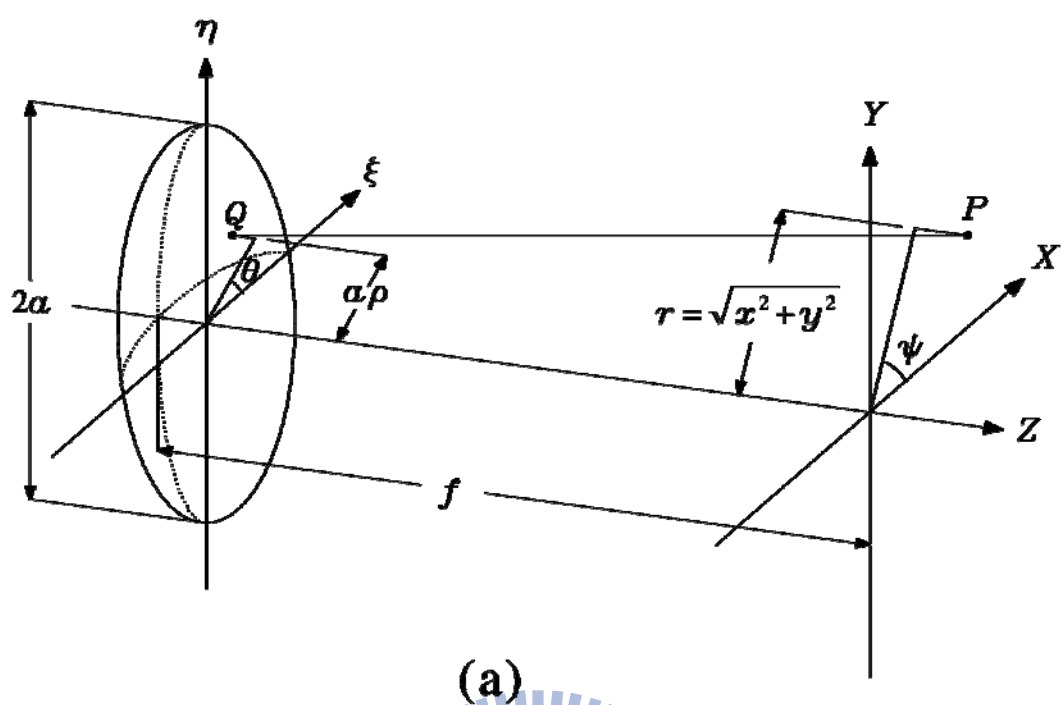
Fig. 3-1 (a) Notation of the coordinate system for beam propagation. (b) Schematic diagram of a split lens where N is the number of sectors. F_1 and F_2 are the first focus and second focus respectively and Δz is the separation between the two lenses. On the top, the sector arrangements for $N=2, 4, 6, 8, 10$, and 12 are shown.

Referring to Fig. 3-1(b), when the lens is split (the distance Δz is finite), a conventional focusing lens with a circular aperture becomes a split lens and two different foci, F_1 and F_2, appear along the Z-axis. *The major concern of this chapter is to explore the interference pattern in the XY-plane and together with the embedded symmetry properties could be changed by the lens splitting.* The motivation is to keep the focal points still along the optical axis. Hence, we follow the well-known Meslin's experiment configuration to split lens in N equiangular sectors, i.e., the sectors are alternatively shifted and un-shifted as illustrated on the top of Fig. 3-1(b). For simplification, we only consider the case of even-number N. The new origin of coordinate system (z=0) is set at the mid-point between two foci.
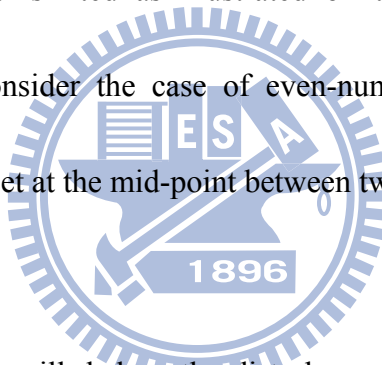
In the following we will deduce the disturbance first. There are mainly two kinds of operation in exploring the symmetry.

(1) $u \rightarrow -u$, which is to identify the reflection symmetry with respect to the mid-focus point at z=0.

(2) $u = u^*$, which is a fixed value to explore the rotational symmetry on the XY-plane.

To evaluate the disturbance we consider the contributions from the shifted sectors and the un-shifted ones. The optical units for these two kind of sectors are now

written as $u_1 = \frac{2\pi}{\lambda}\left(\frac{a}{f}\right)^2\left(z - \frac{\Delta z}{2}\right)$ and $u_2 = \frac{2\pi}{\lambda}\left(\frac{a}{f}\right)^2\left(z + \frac{\Delta z}{2}\right)$, and the disturbance at

point P follows

$$U(P) = -iA'\left\{ e^{i\left(\frac{f}{a}\right)^2 u_1} \int_0^1 e^{-i\frac{u_1}{2}\rho^2} \times \sum_{k=0}^{N/2-1} \int_{2k\frac{2\pi}{N}}^{(2k+1)\frac{2\pi}{N}} e^{-i[\nu\rho\cos(\theta-\psi)]} d\theta \times \rho d\rho \right.$$
$$\left. + e^{i\left(\frac{f}{a}\right)^2 u_2} \int_0^1 e^{-i\frac{u_2}{2}\rho^2} \times \sum_{k=0}^{N/2-1} \int_{(2k+1)\frac{2\pi}{N}}^{(2k+2)\frac{2\pi}{N}} e^{-i[\nu\rho\cos(\theta-\psi)]} d\theta \times \rho d\rho \right\}, \qquad (3\text{-}3)$$

with $A' = \frac{a^2 A}{\lambda f^2}$. The first part of integrand is for the shifted sectors and the second

part is for the un-shifted ones. As to be shown below, it is not straightforward that the

symmetry properties could be categorized in two kinds following the splitting number

is double of an even number (e.g., N=4, 8, 12, …, defined as "double-even") or

double of an odd number (e.g., N=2, 6, 10, …, defined as "double-odd").

3.2.1 N is double of even number

We first discuss the number of sectors N is double-even. Based on Eq. (3-3),

we separate the set of angular integration into two sets of equal length. The former

one is with the index k from 0 to $N/4 - 1$ and the latter one is from $N/4$ to $N/2 - 1$, i.e.,

$$U(P) = -iA' \left\{ e^{i(\frac{f}{a})^2 u_1} \int_0^1 e^{-i\frac{u_1}{2}\rho^2} \times \left(\sum_{k=0}^{N/4-1} \int_{2k\frac{2\pi}{N}}^{(2k+1)\frac{2\pi}{N}} e^{-i[v\rho\cos(\theta-\psi)]} d\theta + \sum_{k=N/4}^{N/2-1} \int_{2k\frac{2\pi}{N}}^{(2k+1)\frac{2\pi}{N}} e^{-i[v\rho\cos(\theta-\psi)]} d\theta \right) \rho d\rho \right.$$
$$\left. + e^{i(\frac{f}{a})^2 u_2} \int_0^1 e^{-i\frac{u_2}{2}\rho^2} \times \left(\sum_{k=0}^{N/4-1} \int_{(2k+1)\frac{2\pi}{N}}^{(2k+2)\frac{2\pi}{N}} e^{-i[v\rho\cos(\theta-\psi)]} d\theta + \sum_{k=N/4}^{N/2-1} \int_{(2k+1)\frac{2\pi}{N}}^{(2k+2)\frac{2\pi}{N}} e^{-i[v\rho\cos(\theta-\psi)]} d\theta \right) \rho d\rho \right\}$$

$$(3\text{-}4)$$

Now we can shift each term in the later set by an angle of π and the index k of latter

set is also shifted to have the same interval with the former set.

$$U(P) = -iA' \left\{ e^{i(\frac{f}{a})^2 u_1} \int_0^1 e^{-i\frac{u_1}{2}\rho^2} \times \left(\sum_{k=0}^{N/4-1} \int_{2k\frac{2\pi}{N}}^{(2k+1)\frac{2\pi}{N}} e^{-i[v\rho\cos(\theta-\psi)]} d\theta + \sum_{k=0}^{N/4-1} \int_{2k\frac{2\pi}{N}}^{(2k+1)\frac{2\pi}{N}} e^{-i[v\rho\cos(\theta-\psi+\pi)]} d\theta \right) \rho d\rho \right.$$
$$\left. + e^{i(\frac{f}{a})^2 u_2} \int_0^1 e^{-i\frac{u_2}{2}\rho^2} \times \left(\sum_{k=0}^{N/4-1} \int_{(2k+1)\frac{2\pi}{N}}^{(2k+2)\frac{2\pi}{N}} e^{-i[v\rho\cos(\theta-\psi)]} d\theta + \sum_{k=0}^{N/4-1} \int_{(2k+1)\frac{2\pi}{N}}^{(2k+2)\frac{2\pi}{N}} e^{-i[v\rho\cos(\theta-\psi+\pi)]} d\theta \right) \rho d\rho \right\}$$

$$(3\text{-}5)$$

The additional angle of π in the cosine makes the former and latter sets to be complex

conjugates to each other. Therefore, the imaginary part of the integrand of polar angle

can be canceled out. By changing the integration interval of each term to be the same,

the disturbance becomes:

$$U(P) = -2iA' \left\{ e^{i(\frac{f}{a})^2 u_1} \int_0^1 e^{-i\frac{u_1}{2}\rho^2} \times \int_0^{\frac{2\pi}{n}} \sum_{k=0}^{N/4-1} \cos\left[v\rho\cos\left(\theta-\psi+k\frac{4\pi}{N} \right) \right] d\theta \rho d\rho \right.$$
$$\left. + e^{i(\frac{f}{a})^2 u_2} \int_0^1 e^{-i\frac{u_2}{2}\rho^2} \times \int_0^{\frac{2\pi}{n}} \sum_{k=0}^{N/4-1} \cos\left[v\rho\cos\left(\theta-\psi+k\frac{4\pi}{N}+\frac{2\pi}{N} \right) \right] d\theta \rho d\rho \right\}$$

$$(3\text{-}6)$$

We introduce a factor $u_{\Delta z/2} = \dfrac{2\pi}{\lambda}\left(\dfrac{a}{f}\right)^2 \dfrac{\Delta z}{2}$ to replace the u_1 and u_2, i.e.,

$u_1 = u - u_{\Delta z/2}$ and $u_2 = u + u_{\Delta z/2}$. The disturbance $U(P)$ could be changed to

$$U(P) = -2iA'e^{i\left(\frac{f}{a}\right)^2 u}\int_0^1 e^{-i\frac{\rho^2}{2}u} \times \left\{ \exp\left[-i\chi\left(\rho,u_{\Delta z/2}\right)\right] \times \int_0^{\frac{2\pi}{N}} \sum_{k=0}^{N/4-1} \cos\left[v\rho\cos\left(\theta - \psi + k\frac{4\pi}{N}\right)\right]d\theta \right.$$

$$\left. + \exp\left[i\chi\left(\rho,u_{\Delta z/2}\right)\right] \times \int_0^{\frac{2\pi}{N}} \sum_{k=0}^{N/4-1} \cos\left[v\rho\cos\left(\theta - \psi + k\frac{4\pi}{N} + \frac{2\pi}{N}\right)\right]d\theta \right\}\rho\,d\rho,$$

(3-7)

with $\chi\left(\rho,u_{\Delta z/2}\right) = \left[\left(\dfrac{f}{a}\right)^2 - \dfrac{\rho^2}{2}\right]u_{\Delta z/2}$. With Eq. (3-7), it is readily verified that the

disturbance has a symmetrical property, $U(-u,v,\psi+\dfrac{2\pi}{N}) = -\left[U(u,v,\psi)\right]^*$. In other

words, the amplitude and the phase with respect to the *XY*-plane of *z*=0 follow

$$\left|U(-u,v,\psi+\frac{2\pi}{N})\right| = \left|U(u,v,\psi)\right| \text{ and } \Phi(-u,v,\psi+\frac{2\pi}{N}) = -\Phi(u,v,\psi) - \pi. \quad (3\text{-}8)$$

Next let us explore the symmetry property on the XY plane, particularly for *z*=0. Also

with Eq. (3-7), when $u = \tilde{u}$, a fixed value, it could be shown that

$U(u = \tilde{u}, v, \psi + \dfrac{4\pi}{N}) = U(u = \tilde{u}, v, \psi)$. In other words, the amplitude follows

$\left|U(u = \tilde{u}, v, \psi + \dfrac{4\pi}{N})\right| = \left|U(u = \tilde{u}, v, \psi)\right|$ and   the   phase

has $\Phi(u = \tilde{u}, v, \psi + \dfrac{4\pi}{N}) = \Phi(u = \tilde{u}, v, \psi)$. In addition, the disturbance in the *XY*-plane

at mid-focus *z*=0 can be further reduced as $U(0,v,\psi+\dfrac{2\pi}{N}) = -\left[U(0,v,\psi)\right]^*$ and thus

the rotational symmetry of intensity distribution in this plane is

$I(0,v,\psi + \frac{2\pi}{N}) = I(0,v,\psi)$, i.e., an *N*-fold rotational symmetry. The rotational

symmetry of phase distribution in this plane is $\Phi(0,v,\psi + \frac{2\pi}{N}) = -\Phi(0,v,\psi) - \pi$, i.e.,

an *N*-fold rotational antisymmetry, apart from a constant π. In other words, there is an

transition of symmetry, the symmetry changed from *N/2*-fold to *N*-fold and back to

N/2-fold as cross over *z=0* plane.

3.2.2 *N* is double of odd number

Next, we derive the disturbance for the case of double-odd. The disturbance is

$$U(P) = -iA'e^{i(\frac{f}{a})^2 u}\int_0^1 e^{-i\frac{\rho^2}{2}u} \times \left\{ \exp\left[-i\chi(\rho,u_{\Delta z/2})\right] \times \sum_{k=0}^{N/2-1}\int_{2k\frac{2\pi}{N}}^{(2k+1)\frac{2\pi}{N}} e^{-i[v\rho\cos(\theta-\psi)]}d\theta \right.$$

$$\left. + \exp\left[i\chi(\rho,u_{\Delta z/2})\right] \times \sum_{k=0}^{N/2-1}\int_{(2k+1)\frac{2\pi}{N}}^{(2k+2)\frac{2\pi}{N}} e^{-i[v\rho\cos(\theta-\psi)]}d\theta \right\}\rho d\rho. \tag{3-9}$$

By changing the order of later set and splitting into two sets with equal length, $U(P)$

becomes

$$U(P) = -iA'e^{i(\frac{f}{a})^2 u}\int_0^1 e^{-i\frac{\rho^2}{2}u} \times \left\{ \exp\left[-i\chi(\rho,u_{\Delta z/2})\right] \times \sum_{k=0}^{\frac{N}{2}-1}\int_{2k\frac{2\pi}{N}}^{(2k+1)\frac{2\pi}{N}} e^{-i[v\rho\cos(\theta-\psi)]}d\theta \right.$$

$$\left. + \exp\left[i\chi(\rho,u_{\Delta z/2})\right] \times \left(\sum_{k=\frac{1}{2}(N/2-1)}^{N/2-1}\int_{(2k+1)\frac{2\pi}{N}}^{(2k+2)\frac{2\pi}{N}} e^{-i[v\rho\cos(\theta-\psi)]}d\theta + \sum_{k=0}^{\frac{1}{2}(N/2-3)}\int_{(2k+1)\frac{2\pi}{N}}^{(2k+2)\frac{2\pi}{N}} e^{-i[v\rho\cos(\theta-\psi)]}d\theta \right) \right\}\rho d\rho, \tag{3-10}$$

We further shift the angle of integration of former set by π and by $-\pi$ in later set such

that

$$U(P) = -iA'e^{i(\frac{f}{a})^2 u}\int_0^1 e^{-i\frac{\rho^2}{2}u} \times \left\{ \exp\left[-i\chi(\rho,u_{\Delta z/2})\right] \times \sum_{k=0}^{N/2-1}\int_{2k\frac{2\pi}{N}}^{(2k+1)\frac{2\pi}{N}} e^{-i[v\rho\cos(\theta-\psi)]}d\theta \right.$$

$$\left. + \exp\left[i\chi(\rho,u_{\Delta z/2})\right] \times \left(\sum_{k=0}^{\frac{1}{2}(N/2-1)}\int_{(2k)\frac{2\pi}{N}}^{(2k+1)\frac{2\pi}{N}} e^{-i[v\rho\cos(\theta-\psi+\pi)]}d\theta + \sum_{k=\frac{1}{2}(N/2+1)}^{N/2-1}\int_{(2k)\frac{2\pi}{N}}^{(2k+1)\frac{2\pi}{N}} e^{-i[v\rho\cos(\theta-\psi-\pi)]}d\theta \right) \right\}\rho d\rho.$$

(3-11)

By adding a negative sign and remove the π in the cosine in the later set, the

disturbance becomes

$$
U(P) = -iA'e^{i(\frac{f}{a})^2 u} \int_0^1 e^{-i\frac{\rho^2}{2}u} \times \left\{ \exp\left[-i\chi\left(\rho, u_{\Delta z/2}\right)\right] \times \sum_{k=0}^{N/2-1} \int_{2k\frac{2\pi}{N}}^{(2k+1)\frac{2\pi}{N}} e^{-i[v\rho\cos(\theta-\psi)]}d\theta \right.
$$
$$
\left. + \exp\left[i\chi\left(\rho, u_{\Delta z/2}\right)\right] \times \left(\sum_{k=0}^{\frac{1}{2}\left(N/2-1\right)} \int_{(2k)\frac{2\pi}{N}}^{(2k+1)\frac{2\pi}{N}} e^{i[v\rho\cos(\theta-\psi)]}d\theta + \sum_{k=\frac{1}{2}\left(N/2+1\right)}^{N/2-1} \int_{(2k)\frac{2\pi}{N}}^{(2k+1)\frac{2\pi}{N}} e^{i[v\rho\cos(\theta-\psi)]}d\theta \right) \right\} \rho d\rho.
$$

(3-12)

After reuniting the later set, Eq. (3-12) becomes

$$
U(P) = -iA'e^{i(\frac{f}{a})^2 u} \int_0^1 e^{-i\frac{\rho^2}{2}u} \times \left\{ \exp\left[-i\chi\left(\rho, u_{\Delta z/2}\right)\right] \times \sum_{k=0}^{N/2-1} \int_{2k\frac{2\pi}{N}}^{(2k+1)\frac{2\pi}{N}} e^{-i[v\rho\cos(\theta-\psi)]}d\theta \right.
$$
$$
\left. + \exp\left[i\chi\left(\rho, u_{\Delta z/2}\right)\right] \times \sum_{k=0}^{N/2-1} \int_{2k\frac{2\pi}{n}}^{(2k+1)\frac{2\pi}{N}} e^{i[v\rho\cos(\theta-\psi)]}d\theta \right\} \rho d\rho.
$$

(3-13)

The disturbance could be further simplified by changing the integration interval of

each term to be the same, i.e., the former and latter sets are complex conjugates to

each other. Then, the imaginary part of integrand of polar angle can be canceled out

and the disturbance follows

$$
U(P) = -2iA'e^{i(\frac{f}{a})^2 u} \int_0^1 e^{-i\frac{\rho^2}{2}u} \times \left\{ \cos\left[\chi\left(\rho, u_{\Delta z/2}\right)\right] \times \int_0^{\frac{2\pi}{N}} \sum_{k=0}^{N/2-1} \cos\left[v\rho\cos\left(\theta - \psi + k\frac{4\pi}{N}\right)\right]d\theta \right.
$$
$$
\left. - \sin\left[\chi\left(\rho, u_{\Delta z/2}\right)\right] \times \int_0^{\frac{2\pi}{N}} \sum_{k=0}^{N/2-1} \sin\left[v\rho\cos\left(\theta - \psi + k\frac{4\pi}{N}\right)\right]d\theta \right\} \rho d\rho.
$$

(3-14)

With Eq. (3-14), it could be seen that the disturbance has a symmetrical property with

respect to the *XY*-plane of *z*=0, i.e., $U(-u,v,\psi) = -[U(u,v,\psi)]^{*}$. As a result, the

symmetrical properties of amplitude and phase can be expressed as

$$|U(-u,v,\psi)| = |U(u,v,\psi)| \quad \text{and} \quad \Phi(-u,v,\psi) = -\Phi(u,v,\psi) - \pi. \qquad (3\text{-}15)$$

Next let us explore the rotational symmetry about the optical axis on various

XY-planes, where the location on the z-axis is fixed ($u = \tilde{u}$), follows

$U(u=\tilde{u},v,\psi+\dfrac{4\pi}{N}) = U(u=\tilde{u},v,\psi)$. In other words, the amplitude and the phase

with respect to the optical axis in various *XY*-planes follow

$$\left|U(u=\tilde{u},v,\psi+\frac{4\pi}{N})\right| = |U(u=\tilde{u},v,\psi)| \quad \text{and} \quad \Phi(u=\tilde{u},v,\psi+\frac{4\pi}{N}) = \Phi(u=\tilde{u},v,\psi)$$

respectively. Both the amplitude and phase have *N*/2-fold rotational symmetry about

the optical axis in various *XY*-planes. In addition, from Eq. (3-14) the disturbance in

the *XY*-plane of *z*=0 (*u*=0) is purely imaginary. Unlike that case of double even, there

is no symmetry transition for double-odd.
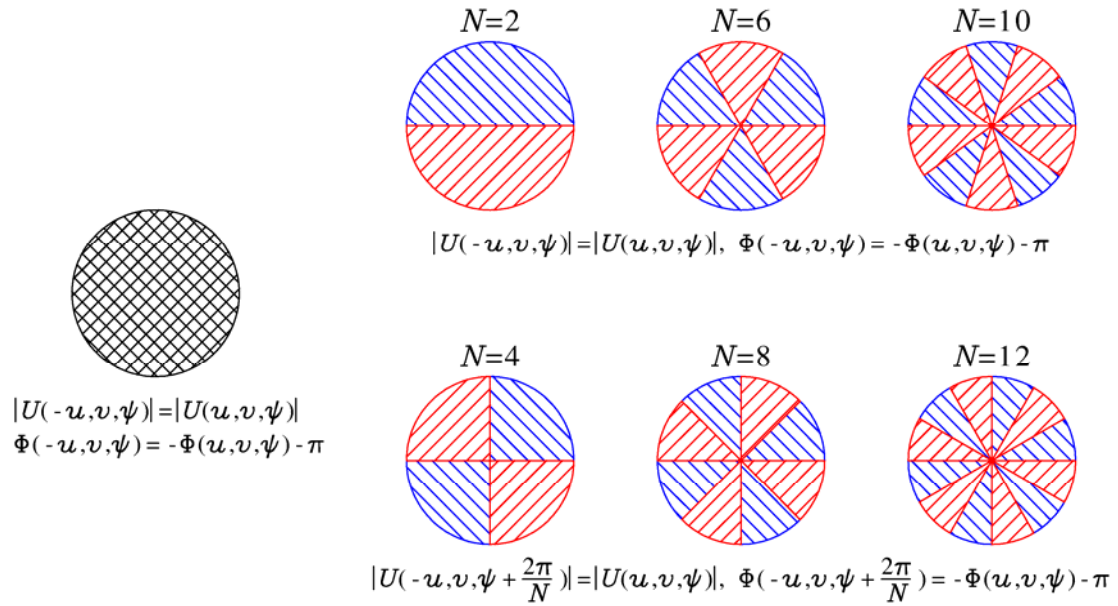
Fig. 3-2 Summary of symmetry relations with respect to the *XY*-plane of *z*=0: (left) classical form for perfect lens; (right) the top shows the case of double of odd number (*N*=2, 6, and 10) while the bottom shows the case of double of even number (*N*=4, 8, and 12).

A comparison of symmetry properties associated with the operation (1), $u \rightarrow -u$, is provided in Fig. 3-2. On the left, the classical result of symmetry property deduced by Collett and Wolf [15] is indicated; on the right-top the split case of double-odd is summarized while on the right-bottom, it contains the cases of double-even. The major difference is the appearance of angle shift, $2\pi/N$ in the double-even case, while in the case of even-odd, the reflection symmetry is kept in intensity distribution and phase distribution is still has reflection antisymmetry apart from an additive factor π.

For both of two cases, the axial disturbance can be expressed as

$$U(x = 0, y = 0, z) = A\left(\frac{e^{-i\frac{\pi}{\lambda}ZA(z)}(1 - e^{i\frac{\pi}{\lambda}ZA(z)\times AF})}{ZA(z)} - \frac{e^{i\frac{\pi}{\lambda}ZB(z)}(1 - e^{-i\frac{\pi}{\lambda}ZB(z)\times AF})}{ZB(z)} \right) \quad (3\text{-}16)$$

where $ZA(z) = \Delta z - 2z, \ ZB(z) = \Delta z + 2z, \ AF = \dfrac{a^2}{2f^2}$

And hence, the disturbance at origin is

$$U(0) = -2\frac{i}{\lambda}\frac{A}{\Delta z}\left\{ \sin\left(\frac{\pi}{\lambda}\Delta z\right) + \sin\left[\frac{\pi}{\lambda}\Delta z(AF - 1)\right] \right\} \quad (3\text{-}17)$$

with the Euler's formula:

$$U(0) = -4\frac{i}{\lambda}\frac{A}{\Delta z}\cos\left[\frac{\pi}{\lambda}\Delta z \cdot \left(1 - \frac{AF}{2}\right)\right] \times \sin\left[\frac{\pi}{\lambda}\Delta z \cdot \frac{AF}{2}\right] \quad (3\text{-}18)$$

For example, if the focal length f=30000λ, a=3000λ and $\triangle z$=300λ, so that the

disturbance at origin is $U(0) = \dfrac{iA}{150\lambda}$.
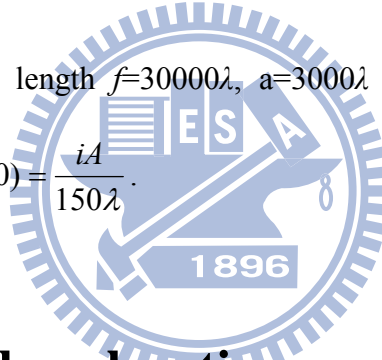
3.3   Numerical explorations

In this section, we provide the result of numerical exploration. Without loss of

generality, the focal length is taken as f=30,000λ, aperture radius a=3,000λ, and the

separation distance along the z axis Δz=300λ or Δz=400λ. The plots of intensity

distribution are normalized to 100. If with a He-Ne laser, the wavelength λ=632.8nm,

then f=18.984 mm which is a typical lens, and the aperture a=1.90 mm, while

Δz=0.18984 or =0.25312 mm are generally available. The observation plane is set at

z=0 where the interference pattern can be clearly seen as shown in Fig. 3 where the

intensity distribution and the phase distribution for the case of N=2 (i.e., 2X1) are

denoted with Fig. 3-3(1a) and Fig. 3-3(1b) respectively. The result (1a) is well known

in literature [3,7]. The corresponding phase Fig. 3-3(1b) shows winding broken strips

in distribution where the strip boundary indicates phase jumps as noted by the color

changes in the plot. The connection between intensity and phase could be identified

by the similarity sharing in the forms of distribution.

Next let us see the intensity distributions of N=6 (i.e., 2X3) and N=10 (i.e., 2X5),

which are denoted by Fig. 3-3(3a) and Fig. 3-3(5a), while the corresponding phase

distributions are shown in Fig. 3-3(3b) and Fig. 3-3(5b) respectively. Now, the

$N/2$-fold rotational symmetry about the optical axis is clearly observed whereas there

is no rotational symmetry for N=2, though it is still 2/2-fold, i.e., 1-fold. On the other

hand, the phase distribution displays the phase changes by π abruptly and as

numerically identified that there are only two kinds of value in phase, i.e., $\pm\pi/2$.

This is because the disturbance in this XY-plane is purely imaginary and this feature

was also observed in the focal plane focused by a conventional focusing lens [3]. The

origin is mainly the inversion symmetry in imaging for a conventional lens (singlet);

this also leads the same feature to the double-odd case.

Now we change to look on the cases of N=4 (i.e., 2X2), N=8 (i.e., 2X4), and

N=12 (i.e., 2X6). The results are dramatically different and they are denoted with Fig.

3-3(2a), (4a), and (6a) for the intensity distribution respectively, while the

corresponding phase distributions are labeled with Fig. 3-3(2b), (4b), and (6b)

respectively. The phase has N-fold rotational **anti**-symmetry apart from a factor π

about the optical axis in the XY-planes at z=0 as shown in Fig. 3-3 with the labels of

Fig. 3-3(2b), (4b), (6b) and the intensity pattern in this plane has N-fold rotational

symmetry as denoted by Fig. 3-3(2a), (4a), and (6a). The variations in phase

distribution are much wild; the phase values are no more kept with only two values

because of the disturbance is not purely imaginary.

In short, one could numerically identify that although the splitting operation is

simply with an even number, there are two kinds of distribution and they could be

further classified according the number of splitting, i.e., either double-even or

double-odd.

Fig. 3-4 plots the intensity and phase distribution in the XY-plane having the

same condition with Fig. 3-3 but the separation distance along the z-axis Δz now is

400λ. The embedded symmetry can still be observed but the intensity in the vicinity

of the optical axis is faint. This destructive interference is caused by the nearly -180°

Gouy phase shift of between two beams focused by the "shifted" and "un-shifted" half-lenses.

Fig. 3-5 and Fig. 3-6 show the intensity and phase distribution for $N=2$ in various XY-planes along the optical axis. From (a) to (i) the observation plane moves in a step of 50λ from the first focus at F_1, to the second focus, at F_2. The separation distance along the z-axis Δz now is 400λ. As expected, there is no rotational symmetry property with respect to the optical axis.

The intensity and phase distribution for $N=6$ are plotted in Fig. 3-7 and Fig. 3-8 having the same condition with Fig. 3-5 and Fig. 3-6, respectively. The symmetry properties around the XY-plane passing through the mid-point of two foci can be readily observed from these figures. The 3-fold symmetry properties with respect to the optical axis are clearly shown in the intensity and phase distribution.

Fig. 3-9 and Fig. 3-10 show the intensity and phase distribution for $N=4$ and the intensity distribution has 2-fold symmetry and phase has 2-fold anti-symmetry can be readily observed. In the case of $N=8$, the intensity distribution has 4-fold symmetry and the phase distribution has 4-fold anti-symmetry are shown in Fig. 3-11 and Fig. 3-12, respectively.

Fig. 3-13 shows the on-axis intensity with the separation distance along the z-axis $\Delta z=400\lambda$. The maximum intensity for the two beams are located at F_1 and F_2 as

shown in Fig. 3-13 but the total maximum intensities are not located at F_1 and F_2

because of constructive and deconstructive interference. As expected, the intensity in

the vicinity of the mid-point of two foci, $z=0$, are small due to the destructive

interference caused by the nearly -180° Gouy phase shift.
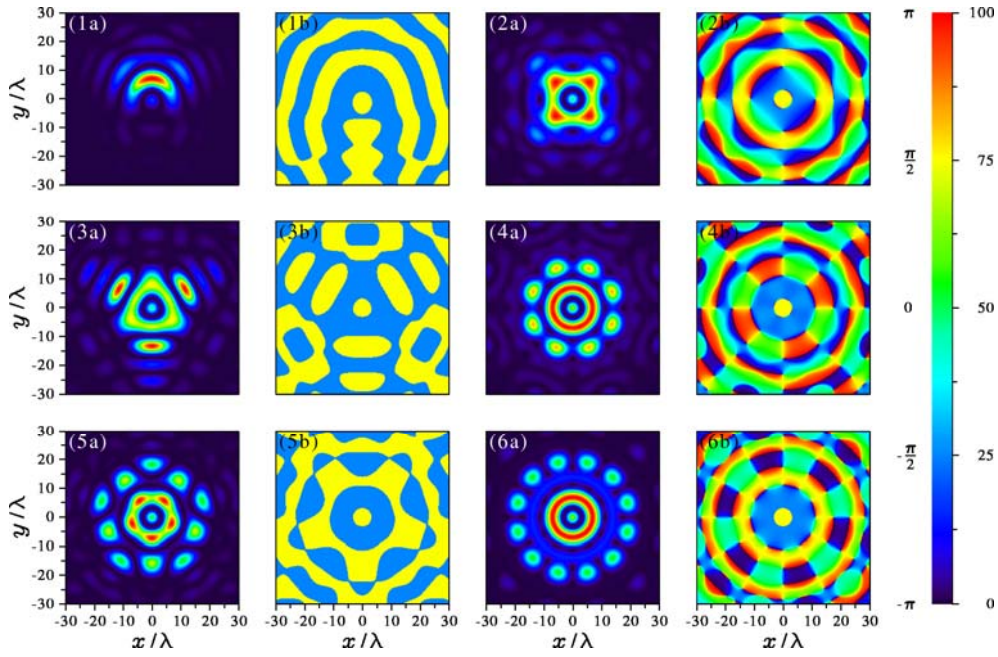
Fig. 3-3 Normalized intensity distribution and the corresponding phase one in the *XY*-plane through the mid-point between two foci where the symbol (a) is for intensity and the symbol (b) is for phase, while (1) for *N*=2, (2) for *N*=4, (3) for *N*=6, (4) for *N*=8, (5) for *N*=10, and (6) for *N*=12. The separation distance along the *z*-axis Δ*z*=300*λ*.
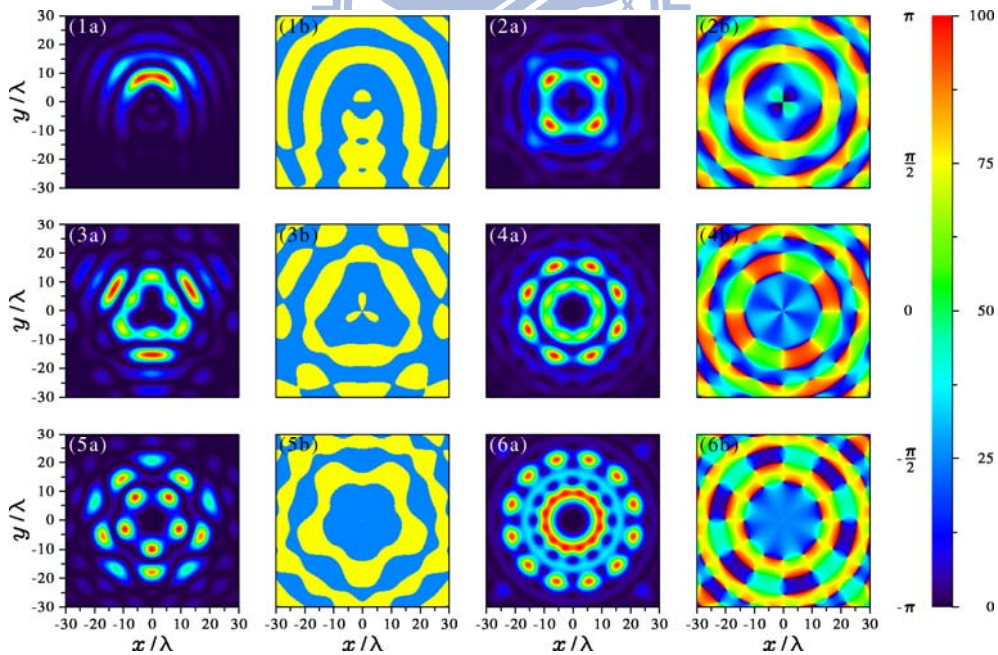
Fig. 3-4 Normalized intensity distribution and the corresponding phase one in the *XY*-plane through the mid-point between two foci where the symbol (a) is for intensity and the symbol (b) is for phase, while (1) for *N*=2, (2) for *N*=4, (3) for *N*=6, (4) for *N*=8, (5) for *N*=10, and (6) for *N*=12. The separation distance along the *z*-axis Δ*z*=400*λ*.

Fig. 3-5 Normalized intensity distribution for *N*=2 at various *XY*-planes along *z*-axis.
(a) *z*=-200*λ*, (b) *z*=-150*λ*, (c) *z*=-100*λ*, (d) *z*=-50*λ*, (e) *z*=0*λ*, (f) *z*=50*λ*, (g) *z*=100*λ*, (h) *z*=150*λ*, (i) *z*=200*λ*.
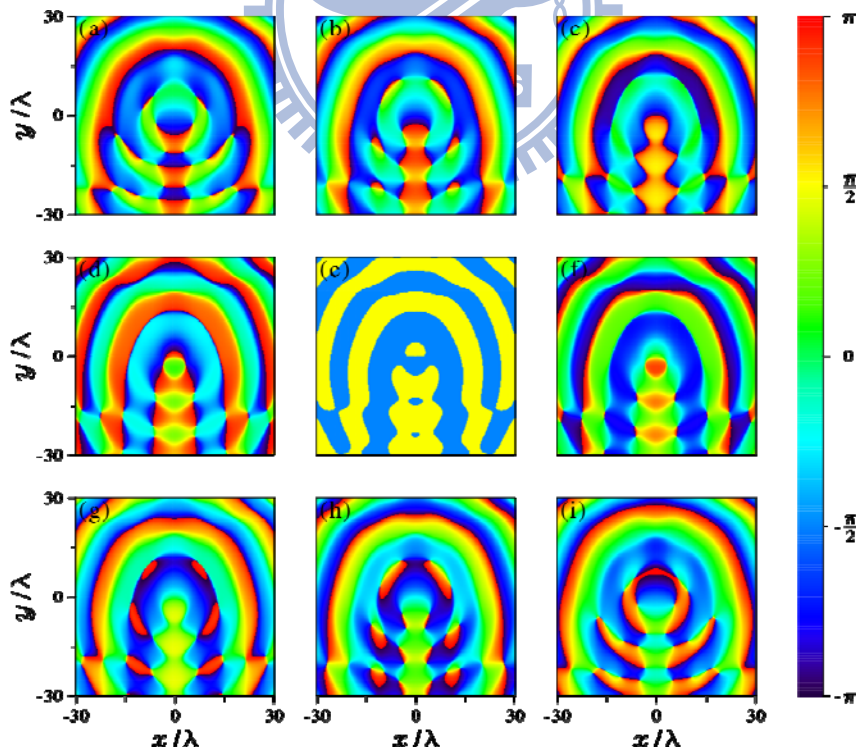
Fig. 3-6 The corresponding phase structure for *N*=2 at various *XY*-planes along *z*-axis.
(a) *z*=-200*λ*, (b) *z*=-150*λ*, (c) *z*=-100*λ*, (d) *z*=-50*λ*, (e) *z*=0*λ*, (f) *z*=50*λ*, (g) *z*=100*λ*, (h) *z*=150*λ*, (i) *z*=200*λ*.
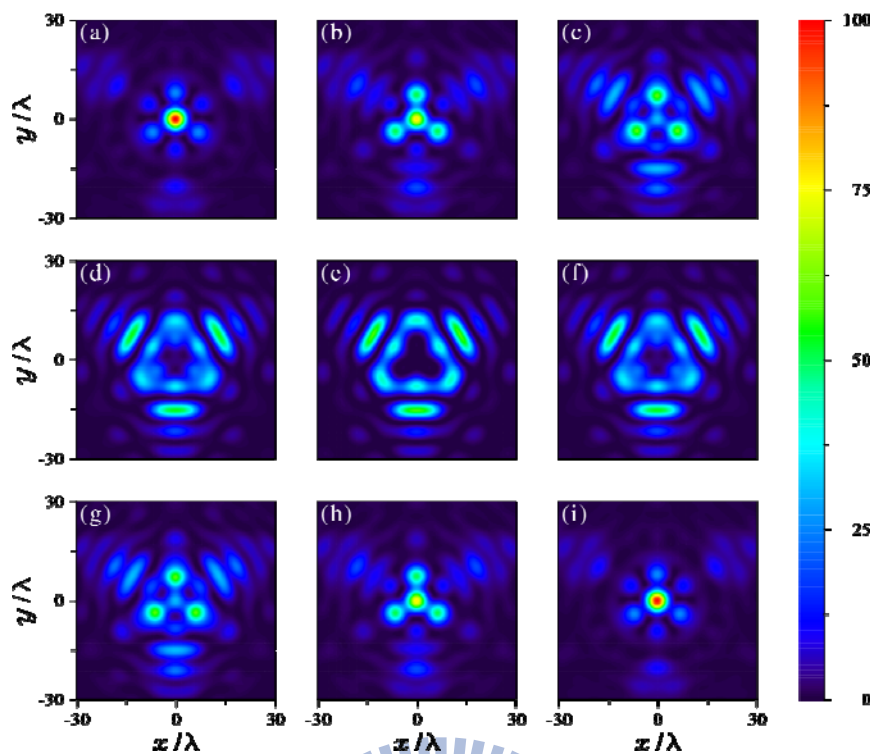
Fig. 3-7 Normalized intensity distribution for *N*=6 at various *XY*-planes along *z*-axis. (a) $z=-200\lambda$, (b) $z=-150\lambda$, (c) $z=-100\lambda$, (d) $z=-50\lambda$, (e) $z=0\lambda$, (f) $z=50\lambda$, (g) $z=100\lambda$, (h) $z=150\lambda$, (i) $z=200\lambda$.
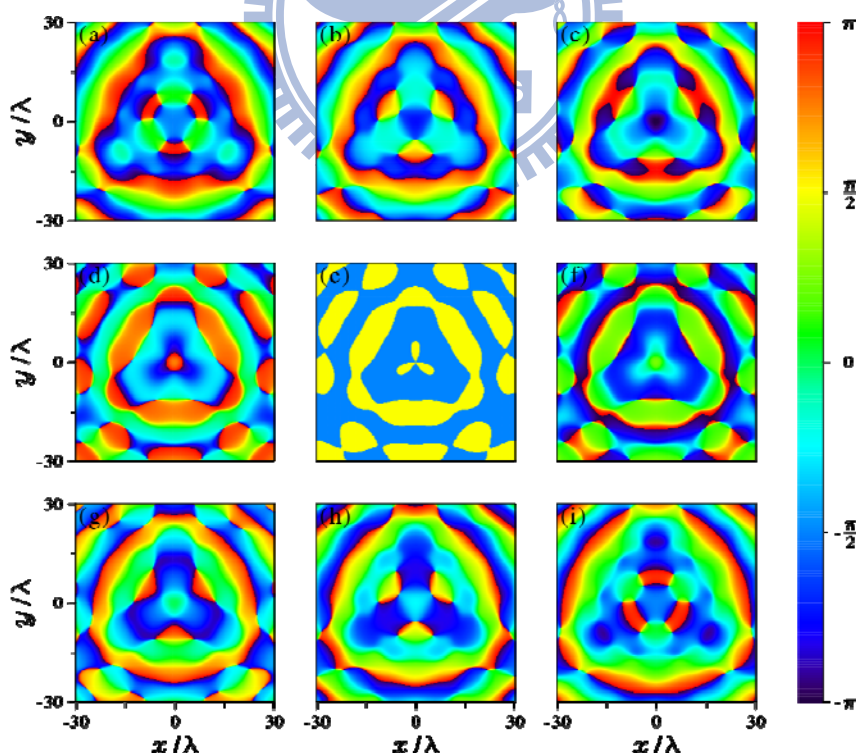
Fig. 3-8 The corresponding phase structure for *N*=6 at various *XY*-planes along *z*-axis. (a) $z=-200\lambda$, (b) $z=-150\lambda$, (c) $z=-100\lambda$, (d) $z=-50\lambda$, (e) $z=0\lambda$, (f) $z=50\lambda$, (g) $z=100\lambda$, (h) $z=150\lambda$, (i) $z=200\lambda$.
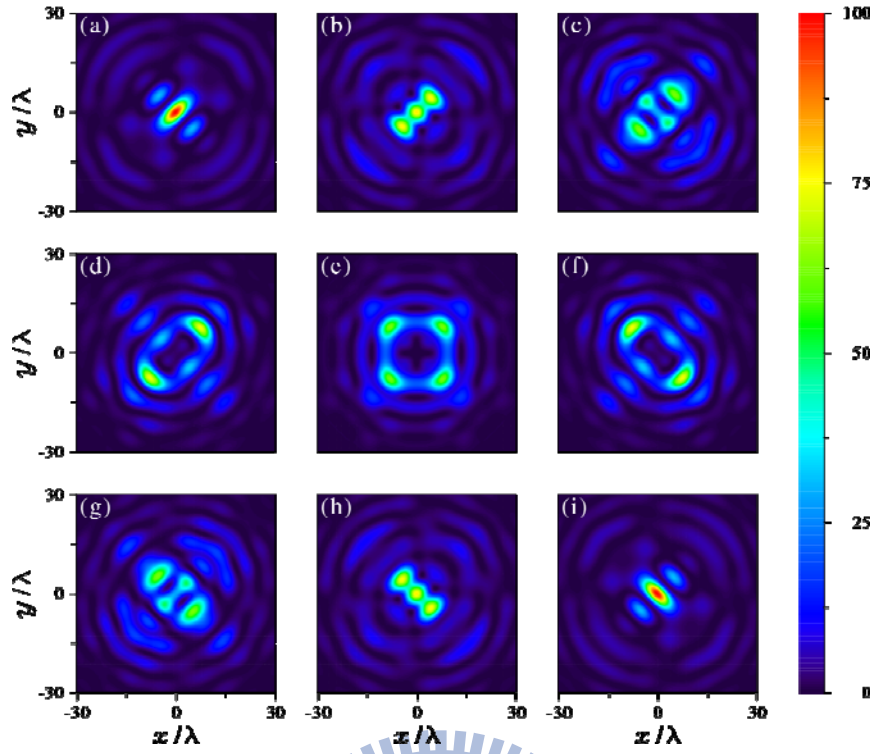
Fig. 3-9 Normalized intensity distribution for *N*=4 at various *XY*-planes along *z*-axis.
(a) *z*=-200*λ*, (b) *z*=-150*λ*, (c) *z*=-100*λ*, (d) *z*=-50*λ*, (e) *z*=0*λ*, (f) *z*=50*λ*, (g) *z*=100*λ*, (h) *z*=150*λ*, (i) *z*=200*λ*.
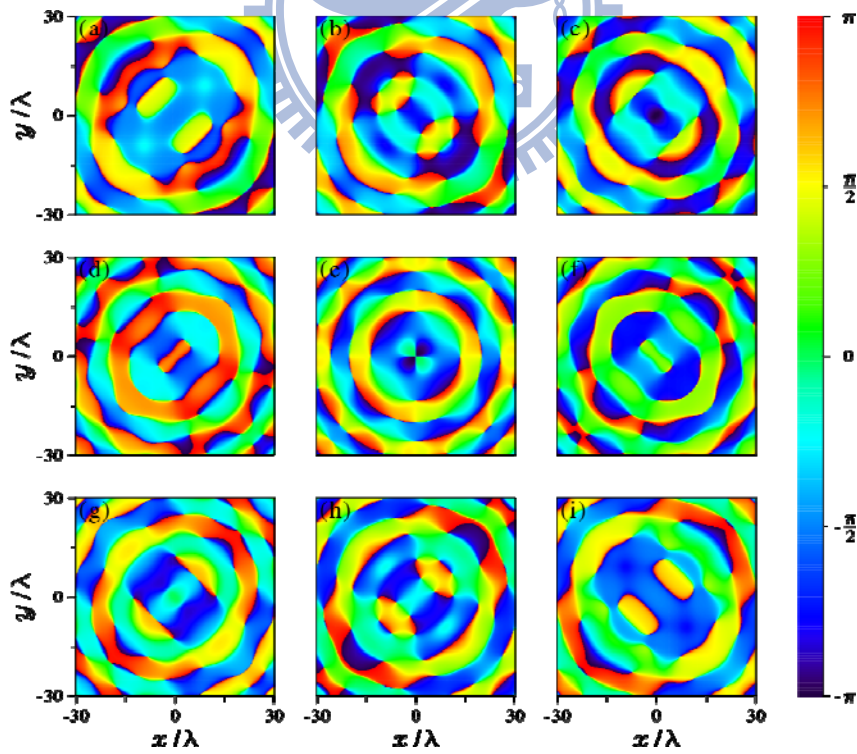
Fig. 3-10 The corresponding phase structure for *N*=4 at various *XY*-planes along *z*-axis.
(a) *z*=-200*λ*, (b) *z*=-150*λ*, (c) *z*=-100*λ*, (d) *z*=-50*λ*, (e) *z*=0*λ*, (f) *z*=50*λ*, (g) *z*=100*λ*, (h) *z*=150*λ*, (i) *z*=200*λ*.
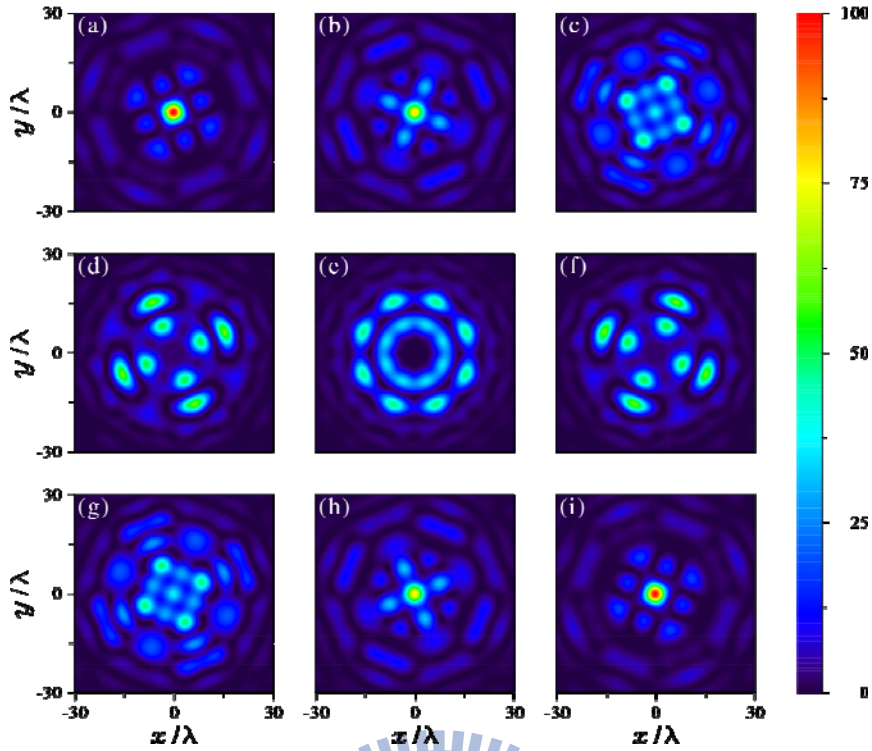
Fig. 3-11 Normalized intensity distribution for *N*=8 at various *XY*-planes along *z*-axis. (a) z=-200λ, (b) z=-150λ, (c) z=-100λ, (d) z=-50λ, (e) z=0λ, (f) z=50λ, (g) z=100λ, (h) z=150λ, (i) z=200λ.
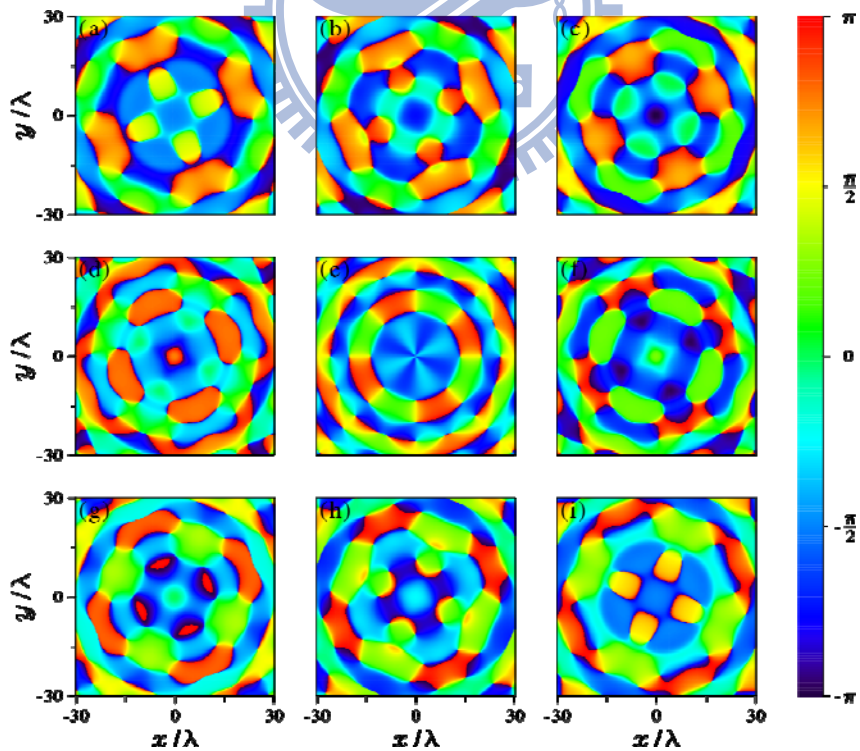
Fig. 3-12 The corresponding phase structure for *N*=8 at various *XY*-planes along *z*-axis. (a) z=-200λ, (b) z=-150λ, (c) z=-100λ, (d) z=-50λ, (e) z=0λ, (f) z=50λ, (g) z=100λ, (h) z=150λ, (i) z=200λ.
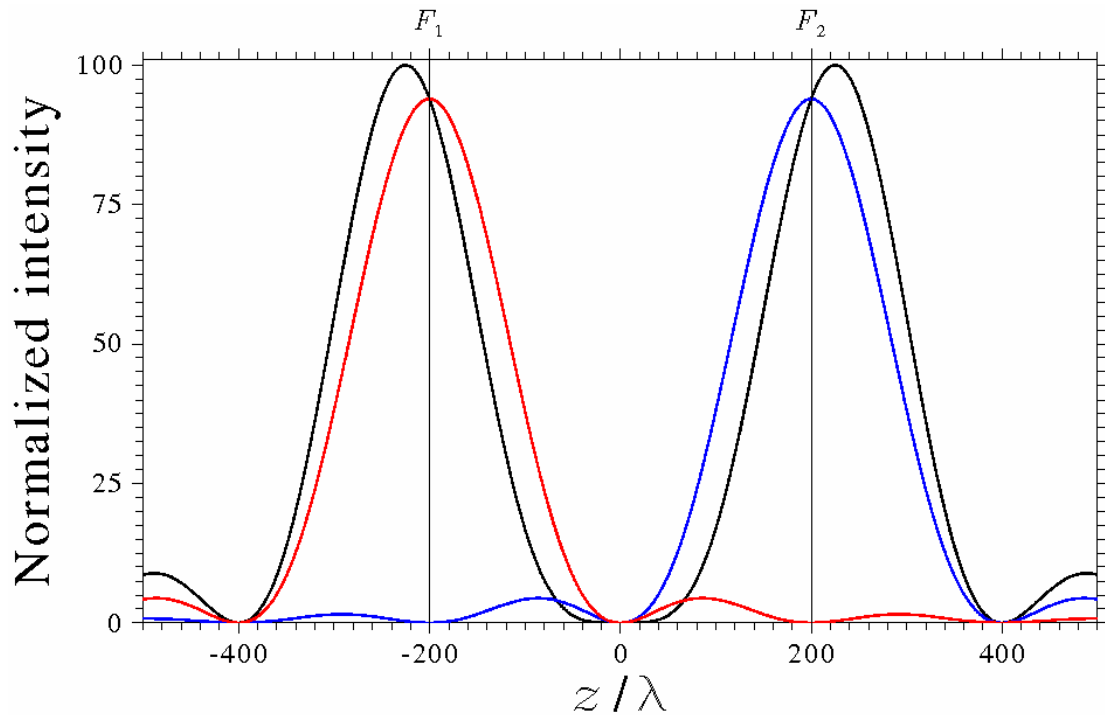
Fig. 3-13 The on-axis intensity and the intensity by two half-lenses are also plotted for comparison. The separation distance along the z-axis $\Delta z=400\lambda$.

Fig. 3-14 shows the intensity on mid-point of two foci varies with respect to the separation distance from Eq. (3-18). There is a region of small and zero intensity when the separation distance is in the vicinity of the multiplication of $2/AF$, e.g. it is 400λ, 800λ and 1200λ etc. here. The zero intensity is resulted from the deconstructive interference while the mid-point is located at the minimum intensity contributed from one lens.
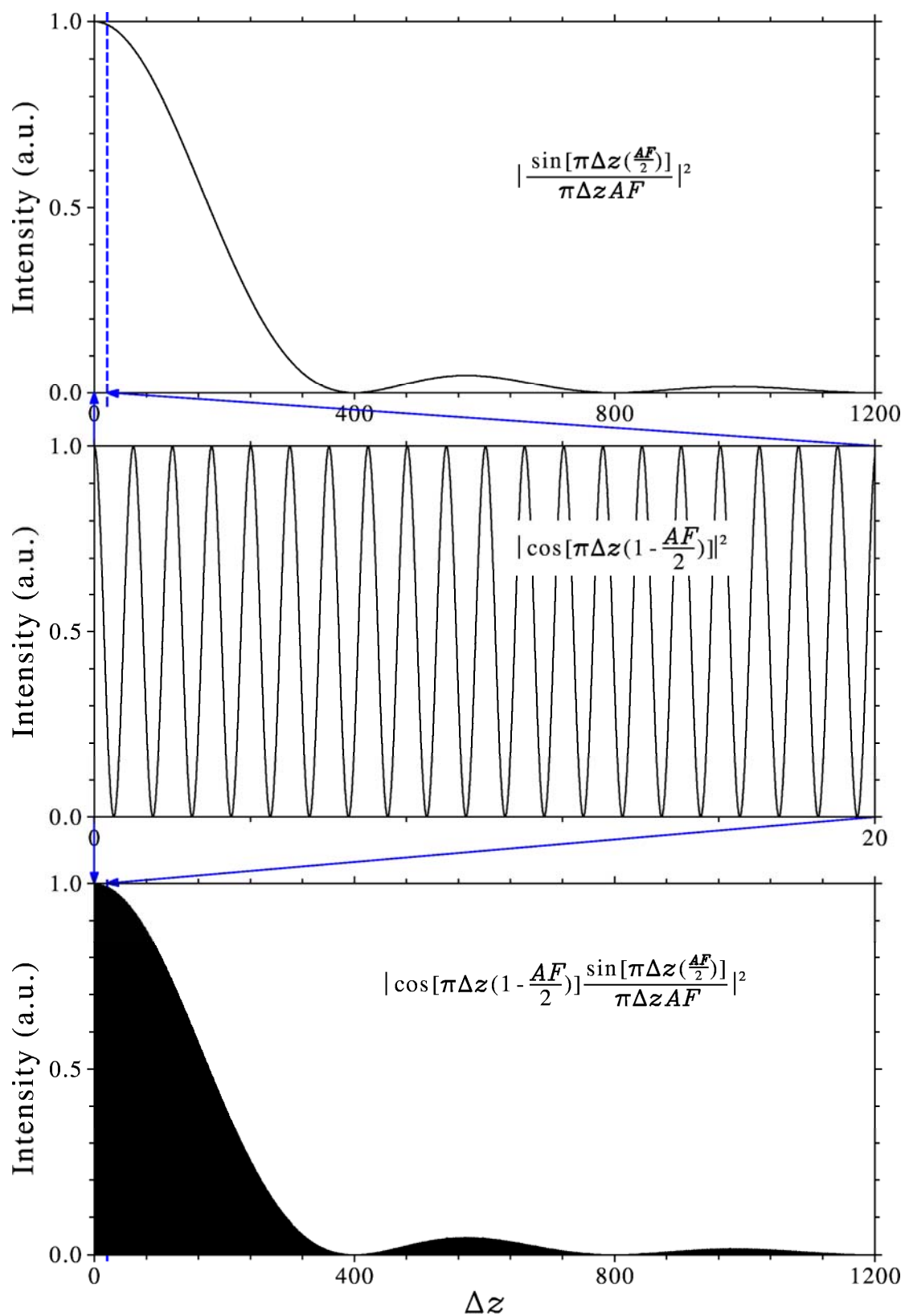
Fig. 3-14 Intensity on mid-point of two foci varies with respect to the separation

distance Δz.

Fig. 3-15 shows the normalized intensity distribution through two foci for the case of double-odd where (a) for $N=2$ and (b) for $N=6$ in the XZ-plane and (c) for $N=2$ and (d) for $N=6$ in the YZ-plane. The symmetry properties with respect to the XY-plane at mid-point of two foci are clearly observed. The intensity in the XZ-plane clearly shows the two foci by the two half-lenses and the dark region resulted from deconstructive interference in the vicinity of the mid-point of two foci
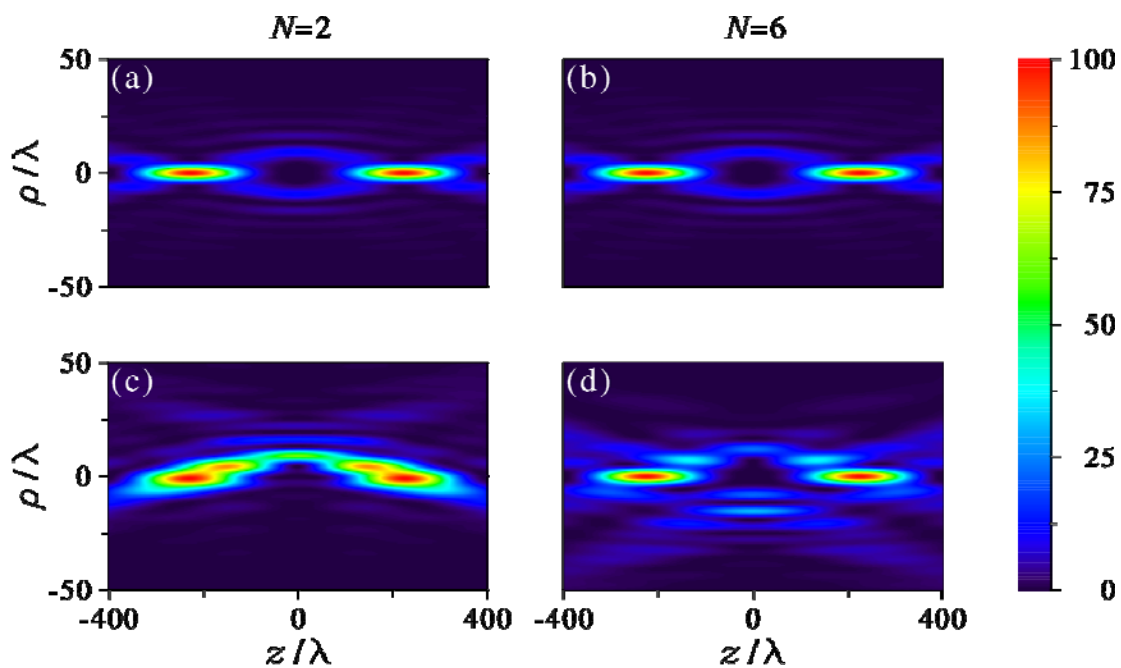
Fig. 3-15 Normalized intensity distribution near focus in the meridional plane. (a) $N=2$ and $\psi=0$, (b) $N=6$ and $\psi=0$, (c) $N=2$ and $\psi=\pi/2$, (d) $N=6$ and $\psi=\pi/2$.
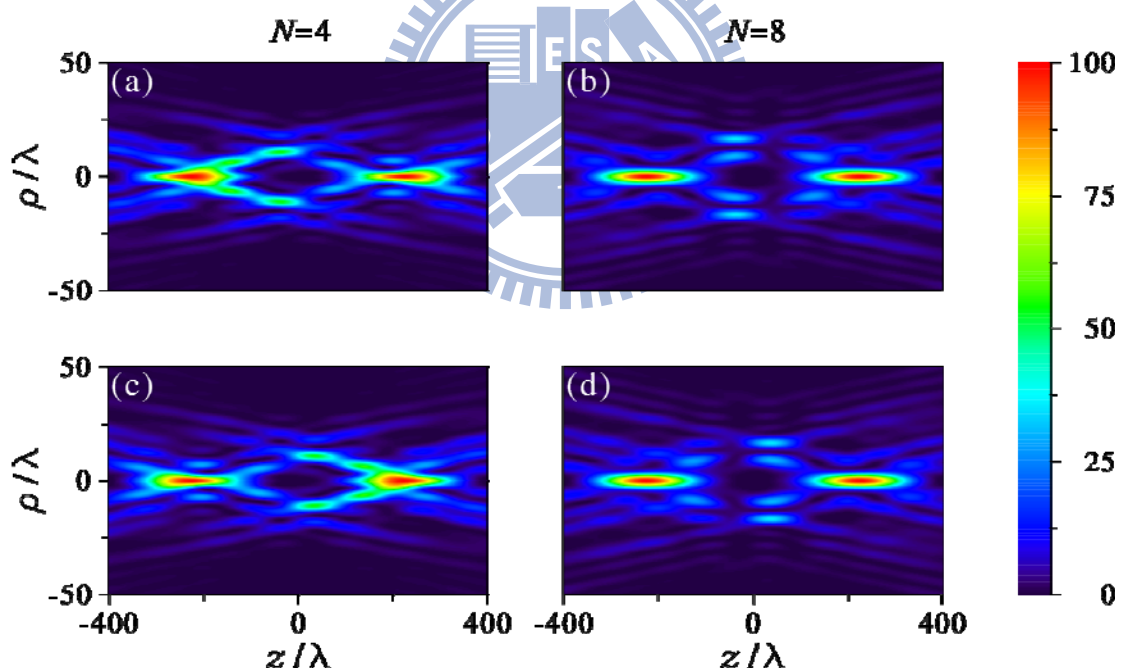
Fig. 3-16 Normalized intensity distribution near focus in the meridional plane. (a) $N=4$ and $\psi=\pi/4$, (b) $N=8$ and $\psi=\pi/8$, (c) $N=4$ and $\psi=3\pi/4$, (d) $N=8$ and $\psi=3\pi/8$.

Fig. 3-16 shows the normalized intensity distribution through two foci for the case of double-even where (a) for N=4 and $\psi=\pi/4$, (b) N=8 and $\psi=\pi/8$, (c) N=4 and $\psi=3\pi/4$, (d) N=8 and $\psi=3\pi/8$. The symmetry properties with respect to the XY-plane at mid-point of two foci are clearly observed. The intensity in the meridional plane clearly shows the two foci by the two half-lenses.

3.4 Summary

In summary, the disturbances of a generalized N-split lens based on the configuration of the Meslin's split-lens experiment have been derived analytically. It has been shown that the distributions have to be categorized into two different cases depending on whether the number of sectors N is double of an odd number (double-odd) or double of an even number (double-even). If the splitting is with double-even, the amplitude and the phase follow $\left|U(-u,v,\psi+\dfrac{2\pi}{N})\right|=\left|U(u,v,\psi)\right|$ and $\Phi(-u,v,\psi+\dfrac{2\pi}{N})=-\Phi(u,v,\psi)-\pi$ respectively. On the other hand, for the case of double-odd, the relation changes to hold with $\left|U(-u,v,\psi)\right|=\left|U(u,v,\psi)\right|$ and $\Phi(-u,v,\psi)=-\Phi(u,v,\psi)-\pi$. The symmetrical properties are distinct with conventional lens.

It is worthwhile to note that there is a symmetry transition for the case of

double-even: the symmetry enforces the all N sectors of interference to have the same

behaviors both in intensity and phase as the observation is right on the $z=0$ plane.

Essentially, there is one difference of angular rotation for the *N/2-fold* symmetries

embedded in the distributions on the planes before and after $z=0$. However, there is no

such symmetry transition for double-odd. It should be emphasized that the section of

such a split-lens generalization is based on a consideration of focal-point distribution.

Based on classical Meslin's split lens configuration, one could have the focal points to

be distributed along the optical axis.
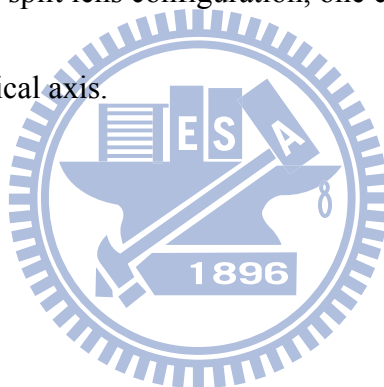
4

Quasi J_0 Bessel beam by Billet's N-split

lens

4.1   Introduction

This chapter studies the utilization of the focal property of a classical Billet's split

lens to create more focal points by splitting the lens and presents the results of a

generalized Billet's split lens, paying special attention to beam propagation. The

generalization is implemented by splitting the lens further, i.e., by creating more focal

points on the focal plane by distributing them circularly. The phenomena of field

distribution and propagation associated with such a generalized split lens are quite

complicated. This chapter explores the characteristics of beam propagation and

analytically derives the asymptotic characteristics of beam propagation based on the

stationary phase approximation and the moment-free Filon-type method. The

underlying symmetry properties of these phenomena have previously explored [16].

Note that a Billet's split lens has already been developed for multiple imaging and

multichannel optical processing [15]. This chapter shows that a *non-diffracting* Bessel

beam [17] can be achieved with by the use of the unique Billet's *N*-split lens if the number of splitting *N* is large enough, e.g., *N≧24*.

The Bessel beam is novel because of its propagation invariant since Durnin *et al*. [17] first reported the non-diffracting Bessel beam generated by an annular aperture [18]. The non-diffracting Bessel beams can also be generated by a phase optical element [19]. In additional to Bessel beam, the non-diffracting Mathiue-Gauss and parabolic Gauss beams are introduced by Gutierrez-Vega *et al.* [20]. Moreover, the non-diffracting beam with mosaic pattern can be created by an apertured axicon [21] and the non-diffracting vortex beams have been studied by using an annular ring mask [22] or by focusing an array of laser arranged in a ring [23]. The width of annular aperture has to be small to produce a non-diffracting beam of long range [24-25] and hence, the energy loss is large. Diffractive optical element can generate an array of arbitrary focuses [26-27] and it is utilized as optical tweezers to trap and arrange particles in a particular shape [28-29], but it usually requires a complicated iterative calculation to obtain the phase/amplitude function. The advantage of the split-lens approach is that, unlike the annual aperture, this simple lens approach allows a much more throughput in creating the Bessel beam and hence the Bessel beam has more optical energy.

4.2   Theoretical Formalism

To illustrate the feature analytically, first consider a conventional focusing lens that is split into two identical halves (two sectors), where the upper half and lower half are moved a distance d up and down the Y-axis, respectively. This is the classical form of the Billet split lens [3] schematically depicted in Fig. 4-1(a). This spilt lens produces a collimated uniform monochromatic wave of wavelength λ to two different foci, F_1 and F_2, on the focal plane. The diffraction theory employed here assumes that the aperture radius $a \gg \lambda$, the focal length $f \gg a \gg \lambda$, and the Fresnel number $F = a^2/\lambda f$ is much larger than unity. Fig. 4-1(b) shows the coordinate system. Recall the eq. (2-7), the disturbance after the Billet's N-split lens is

$$U(P) = C\int_0^1 e^{-i\frac{1}{2}u\rho^2} \int_0^{\frac{2\pi}{N}} e^{iv_d\rho\cos\left(\theta-\frac{\pi}{N}\right)} \times \sum_{m=0}^{N-1} e^{-iv\rho\cos\left(\theta-\psi+m\frac{2\pi}{N}\right)} d\theta\rho d\rho , \qquad (4\text{-}1)$$

where $v_d = \dfrac{2\pi}{\lambda}\left(\dfrac{a}{f}\right)d$ and A is the incident amplitude together with $C = -\dfrac{i}{\lambda}\dfrac{a^2 A}{f^2}e^{i(\frac{f}{a})^2 u}$. The optical units $u = \dfrac{2\pi}{\lambda}\dfrac{a^2}{f^2}z$ and $v = \dfrac{2\pi}{\lambda}\left(\dfrac{a}{f}\right)r = \dfrac{2\pi}{\lambda}\left(\dfrac{a}{f}\right)\sqrt{x^2 + y^2}$, denote the Cartesian coordinate position of P (x, y, z) where $x = r\cos\psi$ and $y = r\sin\psi$. N is the number of sectors and m is the index of sectors.
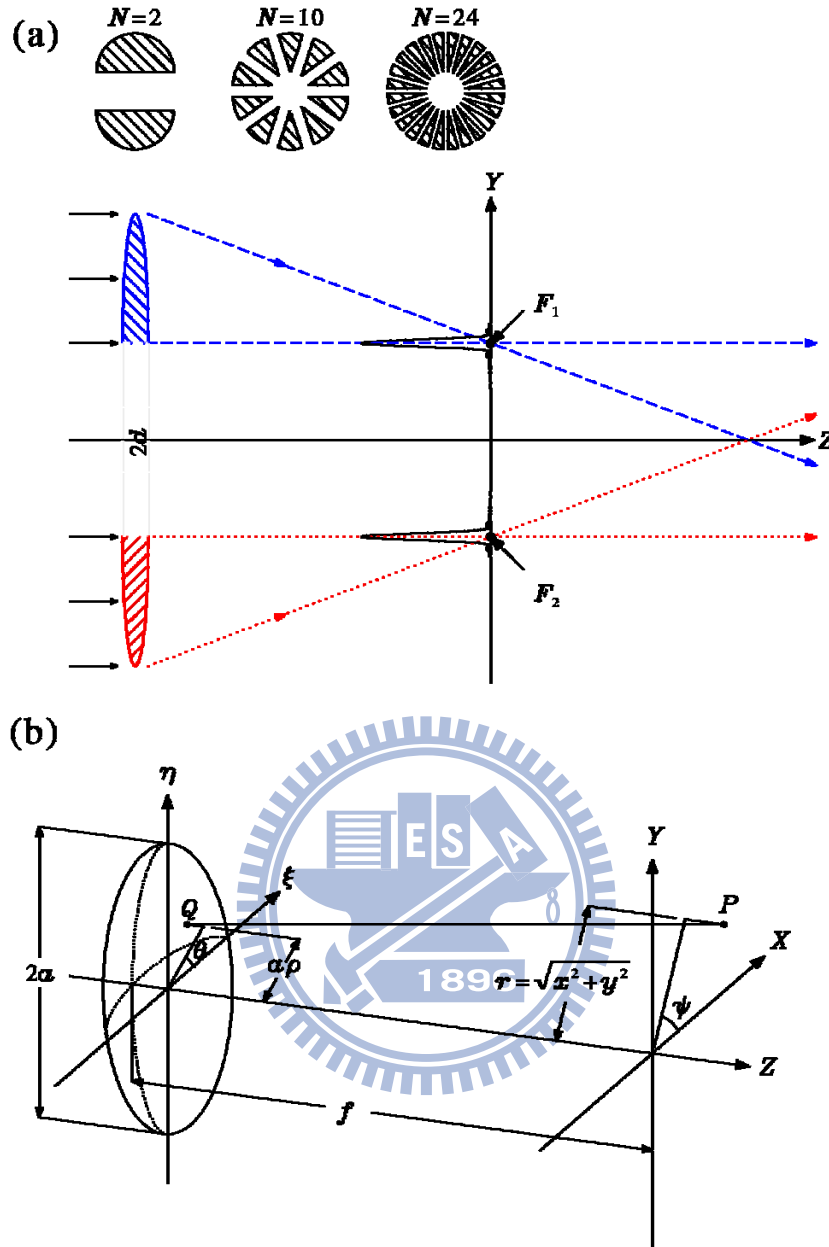
Fig. 4-1 (a) Schematic diagram of the Billet split bi-sector lens. F_1 and F_2 are the first focus and second focus, respectively, and $2d$ is the separation distance between the foci of the two sectors. A front view on the left side shows the arrangement of sectors with $N=2$, 10, and 24, where N is the number of sectors. (b) Notation representation of the coordinate system of beam propagation.

If the sector number N is large, $\cos(\theta-\pi/N)$ can be approximate to unity where θ is

between the interval of 0 and $2\pi/N$ and hence the disturbance can be reduced

$$U(P) = C\int_0^1 e^{-i\left(\frac{1}{2}u\rho^2 - v_d\rho\right)}\int_0^{2\pi}\frac{2\pi}{N}\sum_{m=0}^{N-1}e^{-iv\rho\cos\left(\theta - \psi + m\frac{2\pi}{N}\right)}d\theta\rho d\rho ,\qquad(4\text{-}2)$$

The azimuthal integration can be done by the zero-order Bessel function of the first kind J_0 and the disturbance takes the form

$$U(P) = 2\pi C\int_0^1 J_0(v\rho)e^{-i\left(\frac{1}{2}u\rho^2 - v_d\rho\right)}\rho d\rho ,\qquad(4\text{-}3)$$

The following discussion uses the stationary phase approximation to evaluate the disturbance *when z is much larger than d/*NA, where NA is the numerical aperture. This leads to

$$U(P) = -\frac{2\pi i a^2 A}{\lambda f^2}e^{i\left(\frac{f}{a}\right)^2 u}\sqrt{\frac{2\pi}{u}}\exp^{-\frac{\pi}{4}i}J_0\left(v\frac{v_d}{u}\right)\frac{v_d}{u}e^{i\frac{v_d^2}{2u}} .\qquad(4\text{-}4)$$

The amplitude can be written as

$$|U(P)| = \frac{2\pi a^2 A}{f^2}\sqrt{\frac{2\pi}{|u|}}J_0\left(v\frac{v_d}{u}\right)\frac{v_d}{u}\qquad(4\text{-}5)$$

*When z is smaller than d/*NA, use the moment-free Filon-type method [18] or integration by parts to evaluate the asymptotic approximation of Eq. (4-3) with an error of order $O\left(v_d^{-2}\right)$. This leads to

$$U(P) = \frac{-2\pi i}{v_d - u}e^{i\left(v_d - \frac{u}{2}\right)}J_0(v),\qquad(4\text{-}6)$$

and the amplitude is

$$|U(P)| = 2\pi \frac{J_0(v)}{v_d - u},$$ (4-7)

Equations (4-5) and (4-7) show that the amplitude in the radial direction near the

optical axis is a J_0 Bessel function. This profile is not a function of u, and is

collimated when the propagation distance z is smaller than d/NA, and, conversely, the

profile of J_0 Bessel is a function of u^{-1} and the beam propagates when z exceeds

d/NA.

4.3 Numerical Identification

This section numerically verifies the feature described above. To meet the diffraction

beam requirements, i.e., the numerical aperture (NA) should be small (around 0.05),

take a typical lens with a focal length of a few ten mm, e.g., f=80,000λ, such that the

aperture radius a=4,000λ. Then set the (half) separation distance d=1000λ. For the

numerical example of λ=630 *nm,* we have f=50.4*mm, a*=2.52*mm,* and *d*=0.63*mm.*
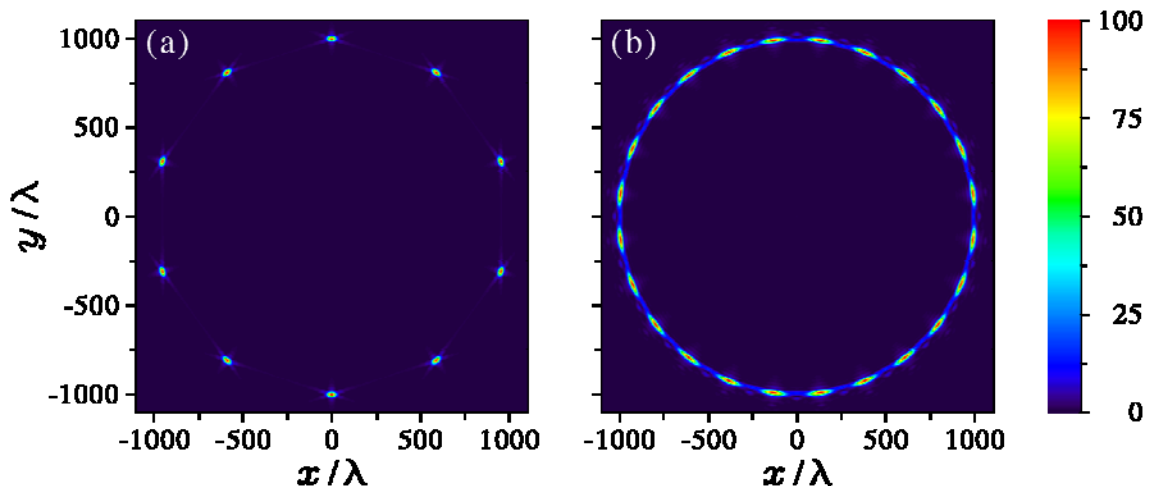
Fig. 4-2 Normalized intensity distribution of the generalized *N*-split lens in the focal plane, where (a) *N*=10 and (b) *N*=24.
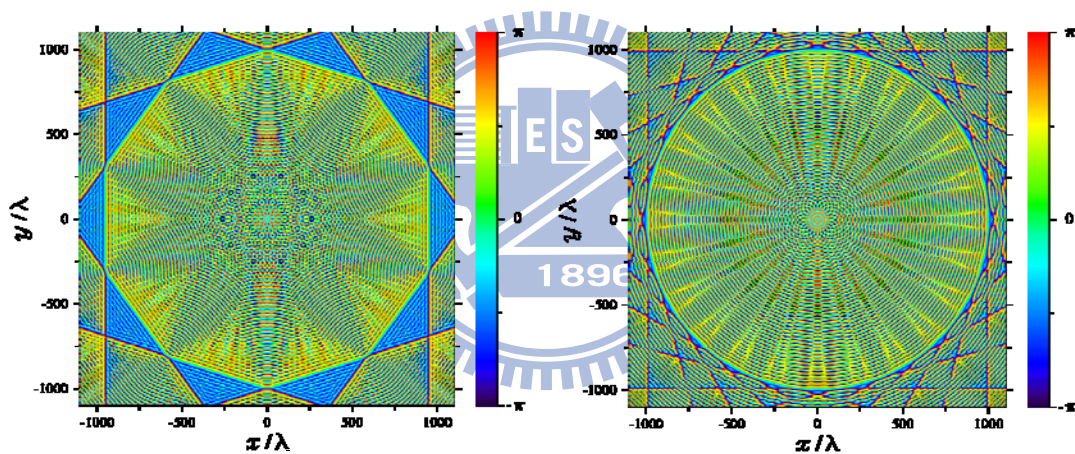
Fig. 4-3 Phase distribution of the generalized *N*-split lens in the focal plane, where (a) *N*=10 and (b) *N*=24.

Fig. 4-2(a) illustrates the intensity distribution in the *XY*-plane of *z*=0, which is

the focal plane, for the case of *N*=10, while Fig. 4-2(b) illustrates that for *N*=24. The

plots of intensity distribution in Fig. 4-2 are normalized to 100. Fig. 4-2 (a) shows that

there are ten focal spots along the azimuthal direction because the number of sectors

N is ten. These ten spots form ten vertexes that resemble a regular ten-sided polygon,

where the circumscribed radius is d=1,000λ and the center is at the origin. On the

other hand, when the number of sectors increases, e.g., N=24, there are twenty four

focal spots resembling a better annular ring pattern with the circumscribed radius of

1,000λ in the focal plane, as Fig. 4-2(b) shows. The annular ring pattern is similar to

an annular slit, and the width of the slit is based on numerical aperture of Billet's

N-split lens. Compared with these focal spots, the intensity near the optical axis is too

dim to observe the Bessel profile in Fig. 4-2. The corresponding phase structures of

Fig. 4-2 are shown in Fig. 4-3.

Next, consider the intensity distribution in the meridional plane with ψ =0

(*XZ*-plane). Fig. 4-4(a) and (b) illustrate the cases of N=10 and 24, respectively. These

figure reveal a quasi Bessel beam profile beyond z=d/NA, particularly for N=24,

which is essentially caused by the ring-like pattern forming on the focal plane. The

intensity maximum is not located on the focal plane, but located approximately at

z=d/NA instead. The location of maximum z_{max} can be numerically evaluated to be

22,187λ and 22,421λ when N=10 and 24, respectively.
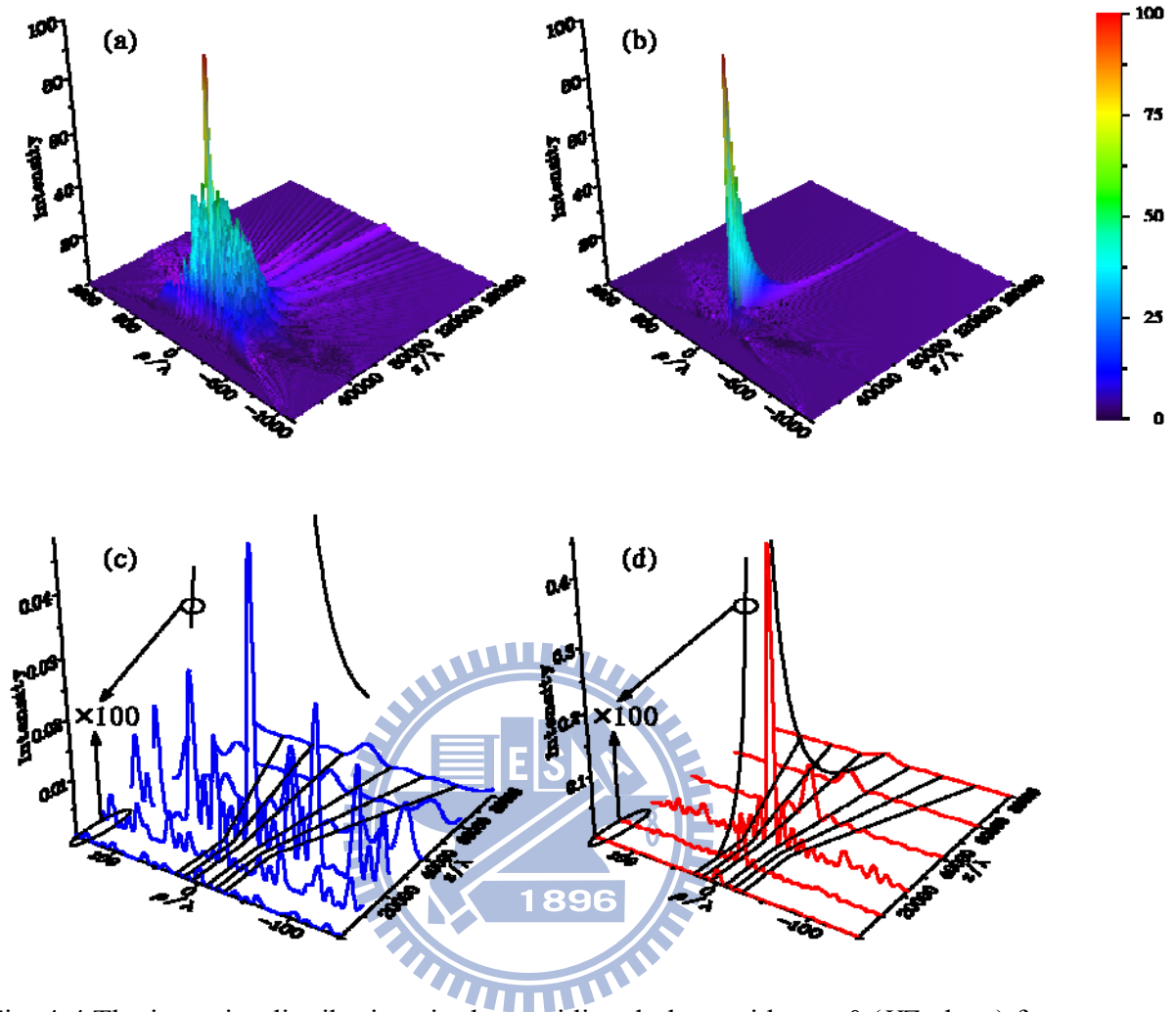
Fig. 4-4 The intensity distributions in the meridional plane with ψ =0 (*XZ*-plane) for different number of split sectors, (a) *N*=10 and (b), *N*=24, where the intensity is normalized to 100. Plots with enlarged scale are shown in (c), *N*=10, and (d), *N*=24, where the first three dark rings of the J_0 are illustrated at the bottom. The on-axis intensity of asymptotic approximations is denoted with solid lines. The intensity within *z*=*d*/NA has been multiplied by 100 as denoted by a circle in the plots (see text).

4.4   Asymptotic Behavior

In this section, this study investigates the asymptotic behavior of the radial intensity

distribution along the *Z*-axis at z=0, 10,000λ, z_{max}, 40,000λ, 60,000λ and 80,000λ are

shown in Fig. 4-4(c) and Fig. 4-4(d) for N=10 and 24, respectively. Note that the

radial intensity within z=d/NA has been multiplied by 100, as the plots and the

regions of illustration are not the same. Note that the asymptotic result calculated by

the stationary phase approximation is for z>>d/NA, while on the other hand, for

z<d/NA. This result is based on the moment-free Filon-type method. Fig. 4-4(c) and

(d) show the asymptotic forms with dark lines. Note that the error between the

calculated intensity and the asymptotic expression based on moment-free Filon-type

method is already enlarged by 100.

To indicate the beam propagation characteristics of quasi J_0 Bessel, Fig. 4-4(c)

and (d) plot the first three roots of J_0 Bessel function parallel to the optical axis. These

three roots denote the first three dark rings of quasi Bessel beam in Eq. (4-7).

Equation (4-7) predicts that the J_0 Bessel function is not a function of z, i.e., the quasi

Bessel beam near the optical axis is collimated within z=d/NA and the intensity is

inversely proportional to $(v_d-u)^2$. Indeed, the on-axis intensity increases from the focal

plane and reaches its maximum intensity when u=v_d. On the other hand, Eq. (4-5)

indicates that the on-axis intensity beyond z=d/NA decays because the intensity is

inversely proportional to $u^{3/2}$. The variable in the J_0 Bessel function is $v\dfrac{v_d}{u}$. Hence,

the locations of minimum in the J_0 Bessel function are linearly proportional to z and

can be plotted as straight lines with slopes of $\dfrac{j_k}{d \cdot 2\pi/\lambda}$, where j_k are the roots of J_0

Bessel function [17].

Fig. 4-4(c) and (d) plot the first three straight lines. In the case of N=10, three

dark rings of Bessel profile are apparent near z=d/NA. On the other hand, there are

eight dark rings when N=24. Except for z, which is near d/NA, these lines fit the dark

rings, and present the propagation properties of J0 Bessel beam clearly.

4.5   Influence of aperture radius

To discuss the influence of aperture size, i.e., the radius a, on the diverging J_0 Bessel

beam, we calculate the intensity disturbance in the meridional plane with the number

of split sectors N=24 and ψ =0 (XZ-plane) for different aperture radius a=40000λ,

24000λ and 16000λ. In Fig. 4 in which the dimension is in a logarithmic scale, we use

the linear curves to denote the dark rings of the J_0 Bessel beam. All intensities in the

frames are normalized by the maximum intensity when aperture radius a=40000λ. The

asymptotic approximation tells the argument in the diverging J_0 Bessel function is

$v\dfrac{v_d}{u}$ or $\dfrac{2\pi}{\lambda}d\dfrac{r}{z}$ where there is no aperture radius a in this argument. In other words,

the diverging J_0 Bessel beam is related to the z and r directly, instead of the aperture

radius a. However, the diverging J_0 Bessel beam is starting from z=d/NA=$f\cdot d/a$. The

aperture radius a, therefore, determines the position of the diverging J_0 Bessel beam

and controls the beam radius of J_0 Bessel beam in terms of $z=d/$NA. As shown in Fig.

4-5, different aperture radius result in different location of $z=d/$NA and give rise to a

minimum beam radius at $z=d/$NA. Consequently, a larger aperture radius, having

larger focusing power, leads to a smaller beam radius at $z=d/$NA, location of the

minimum beam radius.
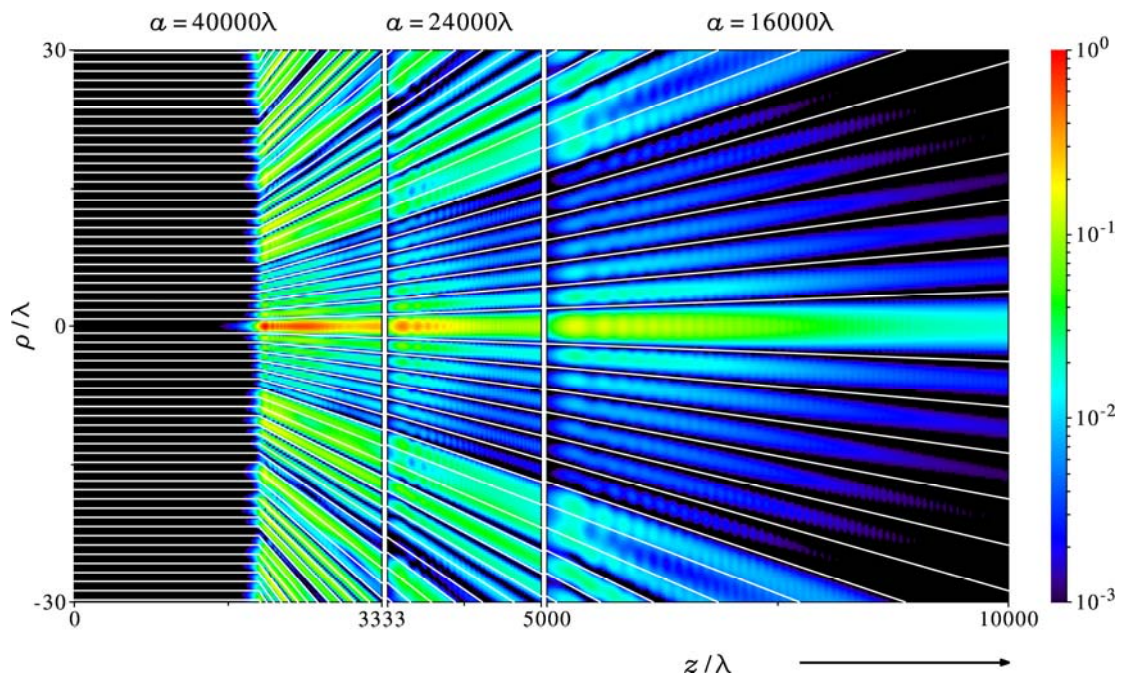
Fig. 4-5 The intensity disturbances in the meridional plane with the number of split sectors $N=24$ and $\psi=0$ (XZ-plane) for the aperture radius at $a=40000\lambda$, 24000λ and 16000λ which corresponds to NA=0.5, 0.3 and 0.2, respectively. The intensity is normalized by the maximum intensity of the case with $a=40000\lambda$. The logarithmic scale is used here. The solid lines also illustrate the dark rings of the J_0 Bessel beam.

Fig. 4-6 illustrates the intensity disturbance in the meridional plane using the

same parameters as in Fig. 4-5 except that the azimuthal angle $\psi=\pi/24$. The J_0 Bessel

beams in Fig. 4-5 and Fig. 4-6 are similar within the seventh dark rings, but they

become different once away from the seventh dark rings. The difference of intensity

disturbance is resulted from the foci of split sectors. In our arrangement, there are two

foci contributing to the J_0 Bessel beam in the meridional plane with $\psi = \pi/24$.

However, there is no focus in the XZ-plane and it gives rise to the J_0 Bessel beam

having different intensity disturbance from that in the meridional plane with $\psi = \pi/24$.

As already shown in Fig. 4-2, different intensity disturbance along different azimuthal

angle occurs because of the arrangement of the sectors.
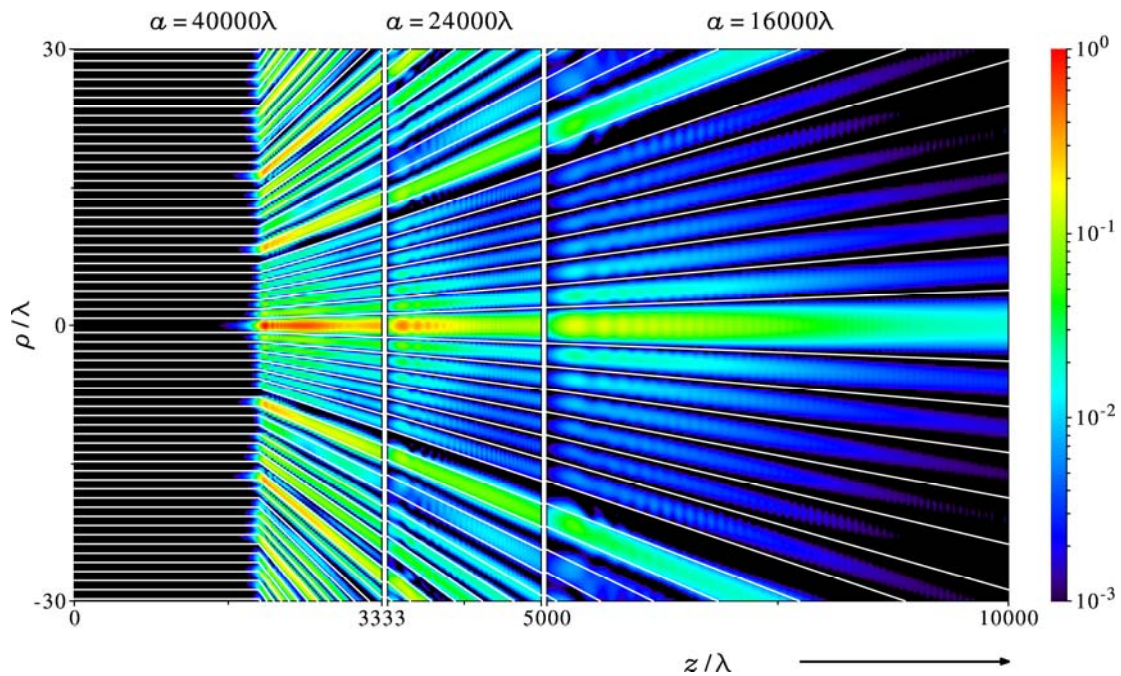
Fig. 4-6 The intensity disturbances in the meridional plane with the number of split sectors $N=24$. The parameters were the same as in Figure 4 except that the azimuthal angle $\psi = \pi/24$.

The on-axis intensity with the number of split sectors $N=24$ for different aperture

radius $a=40000\lambda$, 32000λ, 24000λ, 16000λ and 8000λ is shown in Fig. 4-7 to reflect

the influence of aperture radius a on the diverging J_0 Bessel beam. The inset shows

the on-axis intensity with a logarithmic scale. All the intensities in Fig. 4-7 are

normalized by the maximum intensity as the aperture radius $a=40000\lambda$. We can

readily see that all the asymptotes of oscillating curves overlap when z is beyond

d/NA. The inset with a logarithmic scale shows clearly the overlapping of the on-axis

intensity with different aperture radius.
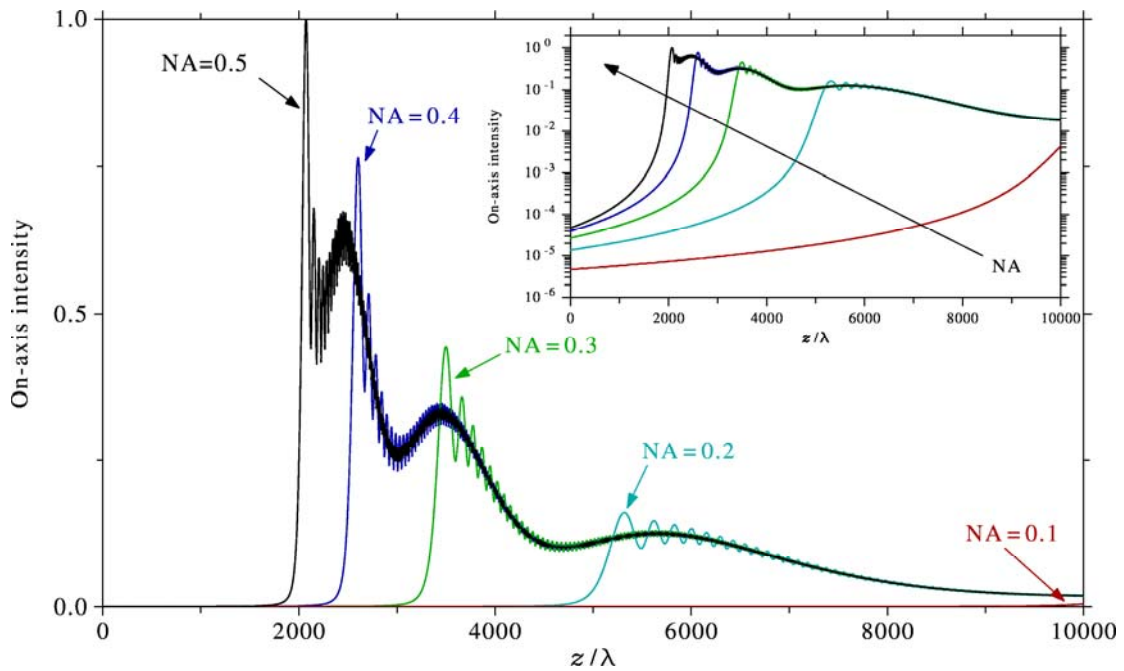
Fig. 4-7 The on-axis intensity for the aperture radius at $a=40000\lambda$, 32000λ, 24000λ, 16000λ and 8000λ which corresponds to NA=0.5, 0.4, 0.3, 0.2 and 0.1, respectively. The intensity is normalized by the maximum ox-axis intensity of the case with a=40000λ. The inset displays the logarithmic scaling for the on-axis intensity.

In short, the aperture size determines the ranges of the asymptotic solution of the J_0

Bessel beam generated by the Billet's N-split lens. Moreover, a larger aperture radius,

having larger focusing power, leads to a larger maximum on-axis intensity near

$z=d$/NA. Note that the location of the maximum on-axis intensity is *close* to $z=d$/NA, not readily on $z=d$/NA.

4.6   Summary
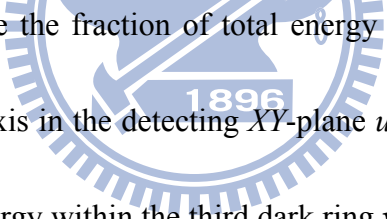
In summary, this chapter shows that it is possible to generate a quasi J_0 Bessel beam using a Billet's N-split lens that introduces a monochromatic plane wave to a ring-like pattern on the focal plane when N is large enough, e.g., 24. This study derives the asymptotic characteristics of beam propagation for the quasi J_0 Bessel beam from the stationary phase approximation and the moment-free Filon-type method.

Results show that the beam is collimated within $z=d$/NA, i.e., the dark rings of the J_0 Bessel beam result in straight lines that are parallel to the optical axis. On the other hand, the beam begins to diverge as $z>d$/NA, and the dark rings of J_0 Bessel beam lead to straight lines with intrinsically-determined slopes. Moreover, the oscillatory property of the on-axis intensity could be deduced, i.e., it increases from the focal plane to a maximum at z $\sim d$/NA, while changed to oscillate downwardly as $z>d$/NA. The aperture radius determines the location of d/NA and controls the minimum radius of J_0 Bessel beam. As expected, larger aperture radius result in smaller beam radius at $z=d$/NA and larger on-axis intensity near $z=d$/NA because of larger focusing power. Finally, note that a segmented-aperture optical system in

which phase-shifting material fills each segmented region [13-14] makes it possible to

realize the generalized Billet's *N*-split lens and create a quasi Bessel beam. The

phase-shifting material could be liquid crystal for this study.

	N=10	*N*=24	*N*→∞
v_{j3}	0.0069	0.0471	0.0550
v_{j7}	0.0449	0.1149	0.1353

Table 4-1 Fractions of energy at $z=2d/$NA for *N*=10, 24 and ∞, where the aperture radius $a=4000\lambda$.

It is interesting to note the fraction of total energy encircled within a circle of

radius *v* about the optical axis in the detecting *XY*-plane *u*=constant. Table 4-1 shows

the fraction of encircled energy within the third dark ring $v=v_{j3}=j_3 \cdot u/v_d$ and the seventh

dark ring $v=v_{j7}= j_7 \cdot u/v_d$ for *N*=10, 24 and *N*→∞ at $u=2d/$NA$=20000\lambda$. As *N*→∞, there

is 5.5% and 13.5% of total energy encircled within three dark rings and seven dark

rings, respectively. If we place a second focal lens with focal length f_2 such that the

front focal plane of second lens is the back focal plane of first split lens [17]. The

effective radius [24] on the second lens is $R_{\text{eff}}=d+f_2 \lambda/\Delta d\sim20516\lambda$ in our notation with

$f_2=30cm$ and $\Delta d\sim1.22\lambda/$NA$\sim24.4\lambda$. Noting that *d* is the radius instead of the diameter

of the ring. The corresponding fraction of encircled energy within R_{eff} is now 81.68%

as $N\to\infty$. The generation of quasi-Bessel beam has a good utilization of incident energy. Noting that, the Bessel beam generated by a diffractive phase element can possess a high diffraction efficiency of up to 93.12% [27].

5

Focal shifts on vector beams

5.1   Introduction

The studies of diffracted converging cylindrical vector beams have attracted

numerous interests both in theoretical and experimental aspects [6,31-43].

Applications include three-dimensional molecular orientation [31,32],

resolution-enhanced microscopy [33], optical trapping and manipulating [34-37], and

surface plasmon interface excitation [38, 39]. In reality, light beam is associated with

polarization. The exploration of the beam propagation characteristics of a polarized

beam is not only important for fundamental understanding but also to provide a useful

mean in exploring and probing the other systems as polarized illumination. In

literature, the propagation and the focusing properties of paraxial Bessel-Gauss beam

with azimuthal polarization have been studied in details by Greene and Hall [40-42].

In addition, the radially and azimuthally polarized beams with a large focal length and

a high numerical aperture have been explored, based on vector Debye diffraction

integral [4], by Brown *et al.* [6,43]. In viewing the importance of polarization

dependence, it is meaningful to identify the beam propagation characteristics of

polarized cylindrical beam. It is worthwhile to note that the cylindrical vector beams

can be generated, such as, by making use of a Mach–Zehnder-like interferometer [6],

by a piece of wave plate [33], by liquid-crystal spatial light modulators [50], by

twisted nematic liquid crystal device [51], or by generating the mode inside a laser

cavity [52].

Technically, once a system has a larger relative aperture, the electromagnetic

vector nature of light has to be taken into account [4,53,54,55]. When vector nature is

included in consideration, the performance will be influenced where the focal

property is always the first item to be checked because of its importance to application

[4]. The irradiance distribution in the focal region is not symmetric with respect to the

focal plane if the Fresnel number of the focusing system is bounded away from

infinity [57]. As a result, the location of the point of principal maximum irradiance is

not consistent with the geometric focus of the focusing lens but is rather closer to the

lens and this phenomenon is referred to *focal shift*. Focal shift has been extensively

investigated over the past decades, e.g., for a variety of systems including in a scalar

converging spherical wave diffracted by a circular aperture [57-61]. However, the

vector nature of electromagnetic wave was not considered there. Nevertheless,

different kinds of focal shift have been studied in a non-apertured [62,63] or apertured

Gaussian beam [64,65], a radially polarized pulsed laser beam [66], a radially

polarized Gaussian beam [67], a Laguerre-Gaussian beam [68], a vector Bessel-Gauss

beam [40], and a vector Mathieu-Gauss beam [69]. It should be noted that the paraxial

and Fresnel approximations were used there [40,62-69]. Theoretically, there are two

approaches, i.e., the vector Kirchhoff diffraction [53-55] and vector Rayleigh theory

[56], which have been used to investigate the effect of focal shifts, by focusing a

linearly polarized electromagnetic wave, with a particular value of Fresnel number

and numerical aperture (NA). A dramatic difference is that the vector Rayleigh theory

does not calculate the diffraction from the spherical wavefront to the aperture because

the vector Rayleigh theory is restricted to the diffraction at a plane screen. Therefore,

the vector Kirchhoff theory is used in this paper to derive the electromagnetic field

vectors in image space and to investigate the focal shift effects for the diffracted

converging cylindrical vector beams with different polarization status.

5.2   Theoretical Background and Beam Formalism

5.2.1 A brief on the vector Kirchhoff diffraction theory

It is known that the Fresnel number, N, and the numerical aperture, NA, follow $N = a^2 / \lambda f$ and $NA = a / f$ respectively, where a is the radius of aperture, λ the wavelength, f the focal length of system and α ($\sin\alpha$=NA) is the maximum convergence angle. Fig. 5-1(a) shows the schematic diagram of the focusing system where vector diffraction is applied to a circular aperture. A radially or azimuthally polarized monochromatic wave with angular frequency ω comes in from the left and is focused by an aplanatic lens. The representation of vectorial diffracted fields can be obtained by a vector analogy of the Green's theorem, which is used in the Helmholtz representation for the diffraction of scalar fields [70-72]. In other words, the vector version of the Green's function is applied to the electromagnetic fields to obtain the electromagnetic field vectors in image space. Therefore, the electromagnetic fields $\mathbf{E}$ and $\mathbf{H}$ in image space can be expressed as the surface integral of $\mathbf{E}_Q$ and $\mathbf{H}_Q$, namely, the spatially dependent electric and magnetic fields at the point Q on the wave front Σ. The $\mathbf{E}_Q$ and $\mathbf{H}_Q$ on the wave front Σ are momentarily

filled in an aperture on a black screen. Therefore, the vector fields in image space can

be written as [70, 72]:

$$\mathbf{E}_\Sigma(\mathbf{x}) = \frac{1}{4\pi}\int\int_\Sigma \left[ik(\hat{\mathbf{n}}\times\mathbf{H}_Q)G + (\hat{\mathbf{n}}\times\mathbf{E}_Q)\times\nabla G + (\hat{\mathbf{n}}\cdot\mathbf{E}_Q)\nabla G \right]d\sigma, \qquad (5\text{-}1)$$

$$\mathbf{H}_\Sigma(\mathbf{x}) = \frac{1}{4\pi}\int\int_\Sigma \left[-ik(\hat{\mathbf{n}}\times\mathbf{E}_Q)G + (\hat{\mathbf{n}}\times\mathbf{H}_Q)\times\nabla G + (\hat{\mathbf{n}}\cdot\mathbf{H}_Q)\nabla G \right]d\sigma, \qquad (5\text{-}2)$$

where $\hat{\mathbf{n}}$ is the inward unit normal vector of Σ and ∇ is the gradient operator with

respect to the integration-point spherical coordinate $\mathbf{r} = (r,\theta,\phi)$, $k = 2\pi/\lambda$ is the

wave number, and $\mathbf{x} = (x,y,z)$ is the Cartesian coordinate or $\mathbf{x} = (\rho,\psi,z)$ the

cylindrical coordinate of the observation point in the image space of the system as

shown in Fig. 1(a). The Green's function G and its derivative are given by

$$G(\mathbf{r},\mathbf{x}) = \frac{\exp(ik|\mathbf{r}-\mathbf{x}|)}{|\mathbf{r}-\mathbf{x}|} = \frac{\exp(iks)}{s}, \quad (\mathbf{s}\equiv\mathbf{r}-\mathbf{x}, s\equiv|\mathbf{r}-\mathbf{x}|), \qquad (5\text{-}3a)$$

$$\nabla G(\mathbf{r},\mathbf{x}) = \hat{\mathbf{s}}(ik - 1/s)G(\mathbf{r},\mathbf{x}) = \hat{\mathbf{s}}ik\zeta(s)G(\mathbf{r},\mathbf{x}), \quad (\hat{\mathbf{s}} = \mathbf{r}-\mathbf{x}/|\mathbf{r}-\mathbf{x}|) \qquad (5\text{-}3b)$$

where the scalar function $\zeta(s)$ is defined as $\zeta(s) = 1 - \dfrac{1}{iks}$. The unit vector $\hat{\mathbf{r}}$ is

directed from the observation point P($\mathbf{x}$), where the electromagnetic field vectors are

calculated, to the point Q($\mathbf{r}$) on the wave front Σ, where the surface integrals are

evaluated.
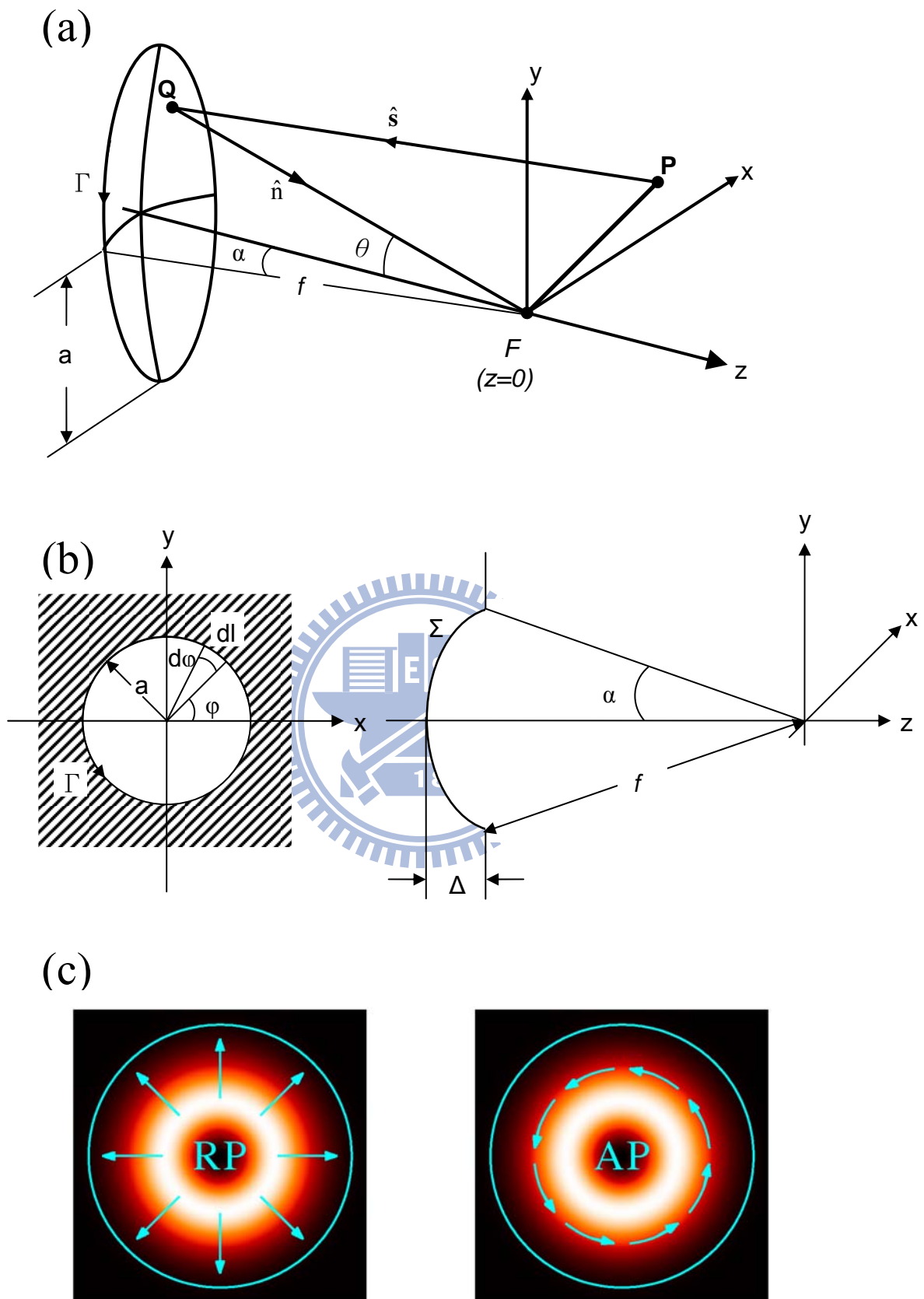
Fig. 5-1 Schematic diagrams of the geometry of a focusing system where a vector diffraction theory is applied over a spherical wavefront surface with a circular aperture of radius a. (see text) (a) three dimensional schematic plot and (b) schematic

diagram of aperture. (c) Schematic illustration of radially polarized (RP) and azimuthal polarized (AP) beams. The corresponding arrows are used to denote the polarization.

In general, the vector fields in Eqs. (5-1) and (5-2) do not satisfy the Maxwell's equations. An additional contour integral around the edge of the aperture has been added as in a saltus black screen problem. Therefore the electromagnetic fields in image space may be expressed in the following forms, $\mathbf{E}(\mathbf{x}) = \mathbf{E}_\Sigma(\mathbf{x}) + \mathbf{E}_\Gamma(\mathbf{x})$, and $\mathbf{H}(\mathbf{x}) = \mathbf{H}_\Sigma(\mathbf{x}) + \mathbf{H}_\Gamma(\mathbf{x})$, with

$$\mathbf{E}_\Gamma(\mathbf{x}) = \frac{1}{4\pi i k} \int_\Gamma (\hat{\mathbf{l}} \cdot \mathbf{H}_Q) \nabla G \mathrm{d}l, \quad \text{and} \quad \mathbf{H}_\Gamma(\mathbf{x}) = -\frac{1}{4\pi i k} \int_\Gamma (\hat{\mathbf{l}} \cdot \mathbf{E}_Q) \nabla G \mathrm{d}l. \qquad (5\text{-}4)$$

where $\hat{\mathbf{l}}$ is the unit vector tangent to the edge of the aperture in the positive direction, as shown in Fig. 5-1(b).

5.2.2 Bending of the E-vector transmitted through

aperture

To identify the beam propagation through a lens, we need to clarify the bending of the E-vector transmitted through focusing system. It can be written as [73]:

$$\mathbf{E}_Q(\theta, \phi) = \mathbf{R}^{-1} L \mathbf{R} \mathbf{E}_{\text{inc}},$$

where $\mathbf{R}$ describes the rotation of the coordinate system around the optical axis and L denotes the change of polarization on propagation through the lens, i.e.,

$$\mathbf{R} = \begin{bmatrix} \cos\phi & \sin\phi & 0 \\ -\sin\phi & \cos\phi & 0 \\ 0 & 0 & 1 \end{bmatrix}, \quad L = \begin{bmatrix} \cos\theta & 0 & -\sin\theta \\ 0 & 1 & 0 \\ \sin\theta & 0 & \cos\theta \end{bmatrix}.$$

For a radially polarized illumination, we have

$$\mathbf{E}_{inc} = |\mathbf{E}_0| g_0(\theta) l_0(\theta) \begin{bmatrix} \cos\phi \\ \sin\phi \\ 0 \end{bmatrix},$$

where $g_0(\theta)$ is the geometric factor, $|\mathbf{E}_0|$ is the amplitude of the **E**-vector in object space, $l_0(\theta)$ is the pupil function which is assumed to vary radially but still maintains the cylindrical symmetry with respect to the optical axis. In the aplanatic system, the geometric factor is $\sqrt{\cos\theta}$. For parabolic mirrors [74], the geometric factor is $\frac{1}{1+\cos\theta}$ as shown by Ignatovsky [75, 76].

Now, the electric vector component after propagating through aplanatic lens system by a RPI can be expressed as

$$\mathbf{E}_Q(\theta,\phi) = |\mathbf{E}_0| l_0(\theta) \sqrt{\cos\theta} \begin{bmatrix} \cos\theta\cos\phi \\ \cos\theta\sin\phi \\ \sin\theta \end{bmatrix}. \tag{5-5}$$

On the other hand, the incident electric fields for an API can be expressed as

$\mathbf{E}_{inc} = |\mathbf{E}_0| g_0(\theta) l_0(\theta) \begin{bmatrix} -\sin\phi \\ \cos\phi \\ 0 \end{bmatrix}$. In the same manner, the electric vector component after an aplanatic lens for API can be expressed as

$$\mathbf{E}_Q(\theta, \phi) = |\mathbf{E}_0| l_0(\theta) \sqrt{\cos\theta} \begin{bmatrix} -\sin\phi \\ \cos\phi \\ 0 \end{bmatrix}. \tag{5-6}$$

5.2.3 Diffracted electric fields in image space

By adding Eqs. (5-1) and (5-4), we can obtain the expression for the diffracted electric

field vectors in image space:

$$\mathbf{E}_i^{(d)}(\mathbf{x}) = \frac{1}{4\pi} \iint_\Sigma \left[ik(\hat{\mathbf{n}} \times \mathbf{H}_Q)G + (\hat{\mathbf{n}} \times \mathbf{E}_Q) \times \nabla G + (\hat{\mathbf{n}} \cdot \mathbf{E}_Q)\nabla G \right] d\sigma + \frac{1}{4\pi ik} \int_\Gamma (\hat{\mathbf{l}} \cdot \mathbf{H}_Q)\nabla G dl,$$

$$(5\text{-}7)$$

where the magnetic field $\mathbf{H}_Q$ can be obtained from $\mathbf{E}_Q$ by

$$\mathbf{H}_Q = \hat{\mathbf{n}} \times \mathbf{E}_Q, \tag{5-8}$$

Eq. (5-8) is true that the field $\mathbf{E}_Q$ and $\mathbf{H}_Q$ are mutually perpendicular and transverse to

the direction of propagation $\hat{\mathbf{n}}$ in free space [77]. After substituting Eqs. (5-8) and

(5-3) into Eq. (5-7), the electric field vectors could now be written as

$$\mathbf{E}_i^{(d)}(\mathbf{x}) = \frac{ik}{4\pi} \iint_\Sigma \left\{ \hat{\mathbf{n}} \times (\hat{\mathbf{n}} \times \mathbf{E}_Q) + \zeta(s) \left[(\hat{\mathbf{n}} \times \mathbf{E}_Q) \times \hat{\mathbf{s}} + (\hat{\mathbf{n}} \cdot \mathbf{E}_Q)\hat{\mathbf{s}} \right] \right\} G d\sigma$$

$$+ \frac{1}{4\pi} \int_\Gamma \hat{\mathbf{s}} \zeta(s) \left[\hat{\mathbf{l}} \cdot (\hat{\mathbf{n}} \cdot \mathbf{E}_Q) \right] G dl. \tag{5-9}$$

In Eq. (5-7) we use the following notation for the observation point in image space:

$$\sigma = f^2 \sin\theta d\theta d\phi, \quad dl = a d\phi,$$

$$\hat{\mathbf{n}} = \begin{pmatrix} -\sin\theta\cos\phi \\ -\sin\theta\sin\phi \\ \cos\theta \end{pmatrix}, \quad \hat{\mathbf{l}} = \begin{pmatrix} -\sin\phi \\ \cos\phi \\ 0 \end{pmatrix}, \quad \hat{\mathbf{s}} = \frac{1}{\varepsilon}\begin{pmatrix} -x/f + \sin\theta\cos\phi \\ -y/f + \sin\theta\sin\phi \\ -z/f - \cos\theta \end{pmatrix}, \qquad (5\text{-}10)$$

where

$$\varepsilon = \frac{s}{f} = \sqrt{\left(1+\frac{z}{f}\right)^2 - 2\left(\frac{z}{f}\right)(1-\cos\theta) + \left(\frac{x}{f}\right)\left(\frac{x}{f} - 2\sin\theta\cos\phi\right) + \left(\frac{y}{f}\right)\left(\frac{y}{f} - 2\sin\theta\sin\phi\right)}.$$

5.2.4 Formalism of radially polarized illumination

To have general beam formalism for the case of RPI, we substitute Eqs. (5-3), (5-5) and (5-10) into Eq. (5-9). After a long vector operation and algebra manipulation, the Cartesian components of the electric field vectors in image space could be deduced, i.e.,

$$\mathbf{E}_i^{(d)}(\mathbf{x}) = \mathbf{i} E_x^{(d)}(x_s, y_s, z_s) + \mathbf{j} E_y^{(d)}(x_s, y_s, z_s) + \mathbf{k} E_z^{(d)}(x_s, y_s, z_s), \qquad (5\text{-}11)$$

$$E_x^{(d)}(\mathbf{x}) = \kappa \int_0^\alpha \int_0^{2\pi} g_0(\theta) l_0(\theta) h(s)\sin\theta\left[-\left(\frac{z}{f}\zeta(s) + (\zeta(s)+\varepsilon)\cos\theta\right)\cos\phi\right]d\phi d\theta$$
$$+ \frac{NA}{4\pi}|\mathbf{E_0}|g_0(\alpha)l_0(\alpha)\int_0^{2\pi} h(s)\zeta(s)\left[-\frac{x}{f} + \sin\alpha\cos\phi\right]d\phi,$$

(5-12a)

$$E_y^{(d)}(\mathbf{x}) = \kappa \int_0^\alpha \int_0^{2\pi} g_0(\theta) l_0(\theta) h(s)\sin\theta\left[-\left(\frac{z}{f}\zeta(s) + (\zeta(s)+\varepsilon)\cos\theta\right)\sin\phi\right]d\phi d\theta$$
$$+ \frac{NA}{4\pi}|\mathbf{E_0}|g_0(\alpha)l_0(\alpha)\int_0^{2\pi} h(s)\zeta(s)\left[-\frac{y}{f} + \sin\alpha\sin\phi\right]d\phi,$$

(5-12b)

$$E_z{}^{(d)}(\mathbf{x}) = \kappa \int_0^\alpha \int_0^{2\pi} g_0(\theta) l_0(\theta) h(s) \sin\theta \left[\zeta(s) \left(\frac{x}{f}\cos\phi + \frac{y}{f}\sin\phi \right) - (\zeta(s) + \varepsilon)\sin\theta \right] d\phi d\theta$$

$$+ \frac{NA}{4\pi} |\mathbf{E_0}| g_0(\alpha) l_0(\alpha) \int_0^{2\pi} h(s) \zeta(s) \left[-\frac{z}{f} - \cos\alpha \right] d\phi,$$

$$(5\text{-}12c)$$

where $K = kf = \dfrac{2\pi N}{(\mathrm{NA})^2}$, $\kappa = \dfrac{iK}{4\pi}|\mathbf{E_0}|$ and $h(s) \equiv \dfrac{\exp(iK\varepsilon)}{\varepsilon^2}$. Now we can construct

the local azimuthal and radial components of $\mathbf{E}_i^{(d)}(\mathbf{x})$ through the following

transformations:

$$E_\psi{}^{(d)}(\mathbf{x}) = E_y{}^{(d)}\cos\psi - E_x{}^{(d)}\sin\psi,$$
$$E_\rho{}^{(d)}(\mathbf{x}) = E_x{}^{(d)}\cos\psi + E_y{}^{(d)}\sin\psi.$$

$$(5\text{-}13)$$

The transformed electric vector components are shown below.

$$E_\rho{}^{(d)}(\rho,\psi,z) = \kappa \int_0^\alpha \int_0^{2\pi} g_0(\theta) l_0(\theta) h(s) \sin\theta \cos(\phi - \psi) \left[\frac{z}{f}\zeta(s) + (\zeta(s) + \varepsilon)\cos\theta \right] d\phi d\theta$$

$$+ \frac{NA}{4\pi} |\mathbf{E_0}| g_0(\alpha) l_0(\alpha) \int_0^{2\pi} h(s)\zeta(s) \left[-\frac{\rho}{f} + \sin\alpha\cos(\phi - \psi) \right] d\phi,$$

$$(5\text{-}14a)$$

$$E_\psi{}^{(d)}(\rho,\psi,z) = 0,$$

$$(5\text{-}14b)$$

$$E_z{}^{(d)}(\rho,\psi,z) = \kappa \int_0^\alpha \int_0^{2\pi} g_0(\theta) l_0(\theta) h(s) \sin\theta \left[\frac{\rho}{f}\zeta(s)\cos(\phi - \psi) - (\zeta(s) + \varepsilon)\sin\theta \right] d\phi d\theta$$

$$+ \frac{NA|\mathbf{E_0}|}{4\pi} g_0(\alpha) l_0(\alpha) \int_0^{2\pi} h(s)\zeta(s) \left(-\frac{z}{f} - \cos\alpha \right) d\phi,$$

$$(5\text{-}14c)$$

where $\varepsilon = \sqrt{1 + \left(\dfrac{\rho}{f}\right)^2 + \left(\dfrac{z}{f}\right)^2 - 2\dfrac{\rho}{f}\sin\theta\cos(\phi - \psi) + 2\dfrac{z}{f}\cos\theta}$ in terms of the

cylindrical coordinate. As expected, the azimuthal component is zero everywhere in

the image space. The radial and longitudinal components are nonzero, however. The

radial and longitudinal fields are independent of ϕ_s which means the existence of a

rotational symmetry around the optics axis.

Now, the total time-averaged electric energy density of the diffracted electric

field vectors for the RPI in image space follows

$$W_E(\rho,\phi,z) = \left|\mathbf{E}_i^{(d)}(\rho,\phi,z)\right|^2 = \left|E_\rho^{(d)}(\rho,\phi,z)\right|^2 + \left|E_z^{(d)}(\rho,\phi,z)\right|^2. \qquad (5\text{-}15)$$

For the special case of the electric field vectors on the optical axis, we have

$$\mathbf{E}_i^{(d)}(0,0,z_s) = \mathbf{i}E_x^{(d)}(0,0,z_s) + \mathbf{j}E_y^{(d)}(0,0,z_s) + \mathbf{k}E_z^{(d)}(0,0,z_s). \qquad (5\text{-}16)$$

Both the x and y components of the diffracted axial electric field vanish, once after

carrying out the integration over ϕ,

$$E_x^{(d)}(0,0,z_s) = 0, \quad E_y^{(d)}(0,0,z_s) = 0, \qquad (5\text{-}17)$$

and only the z component is nonzero, i.e.,

$$E_z^{(d)}(0,0,z) = -\frac{\kappa}{2\pi}\int_0^\alpha g_0(\theta)l_0(\theta)h(s)\sin^2\theta\big(\zeta(s)+\varepsilon\big)d\theta$$
$$-\frac{|\mathbf{E_0}|}{2}NA\times g_0(\alpha)l_0(\alpha)(z/f+\cos\alpha)\zeta(s)h(s)\big|_{\theta=\alpha}$$

(5-18)

It should be noted that the principal maximum energy density of the radial component

is stronger than that of the longitudinal component for a system of low- relative

aperture. Therefore the evaluation of focal shifts by only the longitudinal component

of electric field on the optical axis is not adequate for a RPI with a low-relative

aperture.

5.2.5 Formalism of azimuthally polarized illumination

As to the case of API, by substituting Eqs. (5-3), (5-6) and (5-10) into Eq. (5-9) and

also after a long vector operation and algebra manipulation, we can obtain the

Cartesian components of the electric field vector in image space as shown below.

$$E_x^{(d)}(\mathbf{x}) = \kappa\int_0^\alpha\int_0^{2\pi}g_0(\theta)l_0(\theta)h(s)\sin\theta\left[-\frac{y}{f}\zeta(s)\sin\theta+\left(\frac{z}{f}\zeta(s)\cos\theta+(\zeta(s)+\varepsilon)\right)\sin\phi\right]d\phi d\theta,$$

(5-19a)

$$E_y^{(d)}(\mathbf{x}) = \kappa\int_0^\alpha\int_0^{2\pi}g_0(\theta)l_0(\theta)h(s)\sin\theta\left[\frac{x}{f}\zeta(s)\sin\theta-\left(\frac{z}{f}\zeta(s)\cos\theta+(\zeta(s)+\varepsilon)\right)\cos\phi\right]d\phi d\theta,$$

(5-19b)

$$E_z^{(d)}(\mathbf{x}) = \kappa \int_0^\alpha \int_0^{2\pi} g_0(\theta) l_0(\theta) h(s) \sin\theta \left[\zeta(s)\cos\theta\left(-\frac{x}{f}\sin\phi + \frac{y}{f}\cos\phi \right) \right] d\phi d\theta.$$

(5-19c)

Using the transformation of Eq. (5-13), one can see that the radial and longitudinal

components are zero in the image space, while the azimuthal component follows

$$E_\psi^{(d)}(\rho,\psi,z) = \kappa \int_0^\alpha \int_0^{2\pi} g_0(\theta) l_0(\theta) h(s) \sin\theta$$
$$\times \left[\frac{\rho}{f}\zeta(s)\sin\theta - \left(\frac{z}{f}\zeta(s)\cos\theta + \zeta(s) + \varepsilon \right)\cos(\phi - \psi) \right] d\phi d\theta$$

(5-20)

The azimuthally illuminated objective produces an on-axis null at all distances z_s in

the image space. As expected, and in a manner consistent with the Maxwell's

equations, the azimuthal field propagates as a purely transverse polarization through

the entire image space and the azimuthal field is independent of ψ which means that

there is a rotational symmetry around the optics axis.

5.2.6 Incident beam setting and the fractional focal shift

In literature, a Bessel-Gauss (BG) beam could be a solution of the wave equation

exhibiting radial polarization [48]. Here, we consider the incident beam is a BG beam.

Meanwhile, this BG form will be applied to both the RP and AP beams. A schematic

diagram of such an incident beam is shown in Fig. 5-1(c). In our numerical analysis,

the apodization $l_0(\theta)$ at waist in the pupil of such a BG beam follows [6]

$$l_0(\theta) = \exp\left[-\left(\frac{\beta_0 \sin\theta}{\sin\alpha}\right)^2\right] J_1\left(\frac{2\beta_0 \sin\theta}{\sin\alpha}\right), \qquad (5\text{-}21)$$

where β_0 is the ratio of the pupil radius to the beam waist radius and J_n denotes a

Bessel function of the first kind, of order n. All length units are normalized by λ and

$\beta_0 = 3/2$.

If the principal maximum energy density is located at the point where the z

value of this point is z_0, the fractional focal shift can be expressed as

$$\frac{\Delta f}{f} = -\frac{z_0}{f}. \qquad (5\text{-}22)$$

Eq. (5-22) indicates a larger positive value of fractional focal shift moves the location

of the point of principal maximum electric energy density further towards the

wavefront, and contrariwise, it causes the location further beyond the geometrical

focus. Furthermore, the change rate of fractional focal shift with the Fresnel number

could be defined as $\frac{\partial(\Delta f / f)}{\partial N}$. For the RP and AP illuminations, the principal

maximum energy density may not be on the optical axis of image space. In order to

investigate the focal shift effect for a system having an arbitrary numerical aperture

NA and finite value of Fresnel number N, the Powell's method [78] is used to

numerically determine the location of the point of principal maximum energy density

in image space.
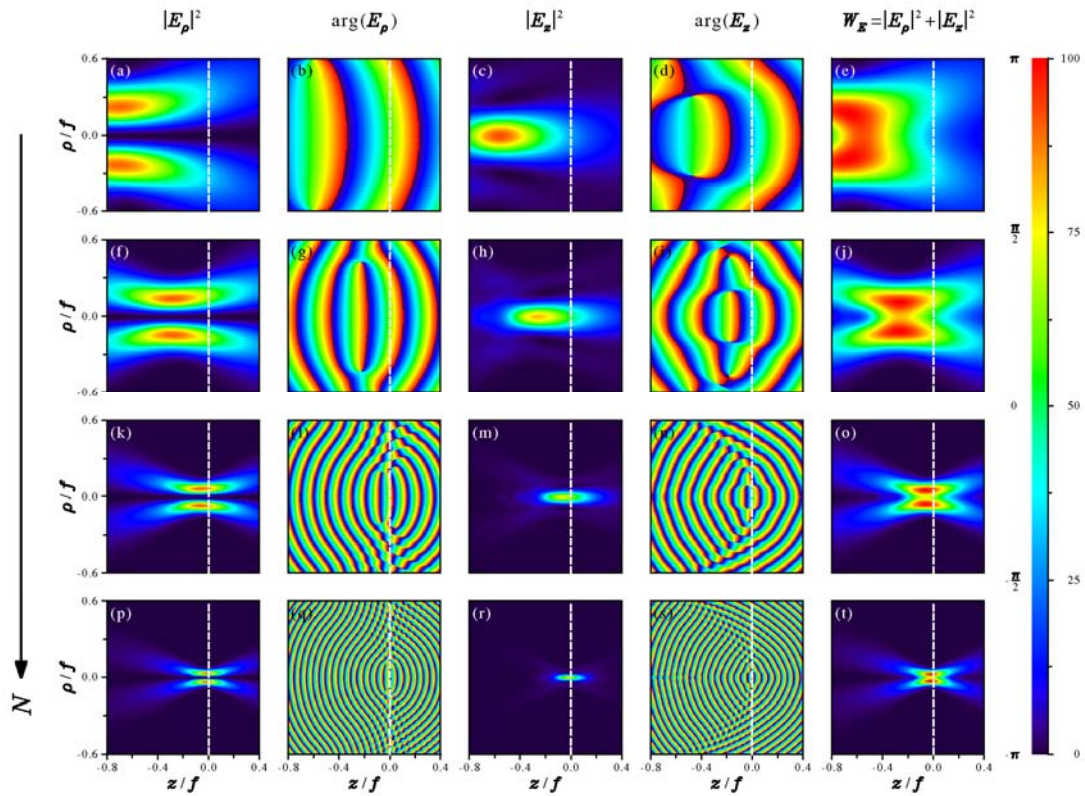
Fig. 5-2 Density plot of the normalized time-averaged electric energy density for the radially polarized beams in the ρ–z plane with a numercial aperture NA=0.7, where the dashed line is used to indicate the geometrical focal plane. The rows from top to down are with the Fresnel number N=1, N=2, N=5 and N=10 correspondingly. The radial components are shown the first colum and the corresponding phase structures are shown in the second column. The longitudinal components are shown in the third column and the corresponding phase structures are shown in the fourth column, respectively. The density plots of the normalized total time-averaged electric energy density are shown in the fifth column.

It will be very helpful to provide the distribution of total energy density to gain a

clearer feature of beam propagation characteristics. We show the results of two

polarized illuminations in Fig. 5-2 and Fig. 5-3 respectively. For a simple illustration,

we set the numerical aperture NA=0.7 and take four Fresnel numbers N, i.e., 1, 2, 5

and 10, also for comparison. Fig. 5-2 shows the result of RPI. The existence of focal

shifts associated with the radially polarized vector beams could be seen clearly. It also

shows that the fractional focal shifts decrease as the Fresnel number N increases.

Furthermore, there is a distinct asymmetry of energy-density distribution on both

sides of the geometric focus. However, this asymmetry depends strongly on the

Fresnel number N and it is less significant when the Fresnel number N is large. On the

other hand, for the case of API, as shown in Fig. 5-3, the AP beam does not generate a

longitudinal component, while the transverse field is actually resulted from the

azimuthal component. The existence of focal shift of azimuthally polarized beam is

clear. Overall, the characteristics of beam propagation of the two illuminations, i.e.,

RPI and API, are different. The difference is significant when the Fresnel number is

small. We also provide the corresponding phase structures for reference.
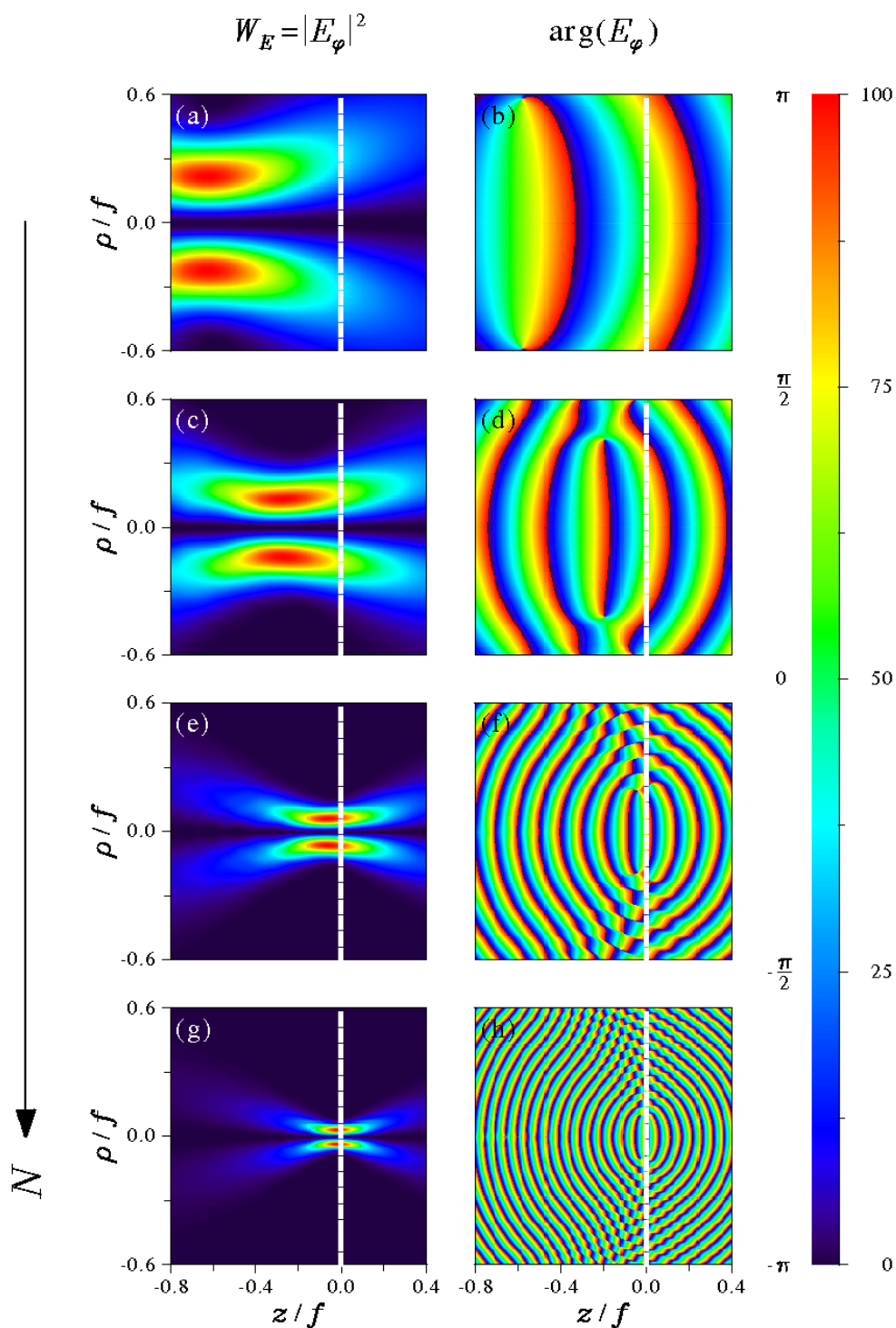
Fig. 5-3 Density plot of the normalized time-averaged electric energy density for the azimuthally polarized beams in the ρ–z plane with a numerical aperture NA=0.7, where the dashed line indicates the geometrical focal plane. The rows from top to down is with the Fresnel numbers N=1, N=2, N=5, and N=10. The first column is the energy density where the corresponding phase structures are shown in the second column respectively.

5.3   Influence of incident polarization on focal shift

In this section the influence of incident polarization on focal shift will be extensively numerically explored. In order to investigate the dependence of numerical aperture, the fractional focal shifts at different NAs are also numerically evaluated. It should be noted that for a system of low-relative-aperture, e.g., NA=0.1, the principal maximum energy density of the transverse component is stronger than that of the longitudinal component. Hence, the fractional focal shift in a low-relative-aperture system depends primarily on the transverse component, which is purely radially polarized. On the other hand, the principal maximum energy density of longitudinal component becomes comparable to that of transverse component when the system is with high-relative aperture, e.g., NA=0.9. Therefore, the fractional focal shifts will be evaluated by both of the transverse and longitudinal components. In numerical investigations, the numerical aperture NA is ranged from 0.1 to 0.99, totally 10 sets, and the Fresnel number N is taken from 1 to 12.

5.3.1 The case of radially polarized illumination (RPI)

Typical feature of beam propagation of RPI could be referenced by Fig. 5-2. It is clearly that the focal point will be shifted as the Fresnel number is changed. The focal shifts associated by RPI are shown quantitatively by fractional focal shift in Fig. 5-4. The variation could be categorized in three regions, namely A, B, and C, as denoted on the top in Fig. 5-4. In the region A, the fractional focal shift varied not significantly over a range of the Fresnel number and the amount is less than 5%. In the region B, the fractional focal shift is within 5%-30% and the variation is inversely proportional to the Fresnel number. In the region C, the shift is larger than 30% and is nearly linearly proportional with the Fresnel number. The region classification still holds with different numerical apertures, although with a high-relative aperture, the variation is more noteworthy than that of low-relative aperture. In the region A, the change rate of the fractional focal shifts with respect to the Fresnel number ($N>7$) is nearly zero, i.e., $\dfrac{\partial(\Delta f / f)}{\partial N} \sim 0$. In other words, the focal shift is much insignificant and we could take the change is less than 5% as a basic property. The change rate of the fractional focal shift with the Fresnel number becomes considerably different in the region B and $\dfrac{\Delta f}{f} \propto \dfrac{1}{N}$, but the transition is smooth. In the case of RPI, the transition point is around $N \sim 7$. In the region C, the change rate is positive and there is

a nearly linear increase as the Fresnel number is moved close to 1, i.e., $\dfrac{\partial(\Delta f / f)}{\partial N} \sim 1$.

It is interesting to note that the regions B and C are separated by the appearance of crossover feature located at $N \sim 1.8\text{-}1.9$ as denoted by a red arrow shown the insert in Fig. 5-4. The crossover is associated with the change rate of fractional focal shift which becomes faster with large NA, here the bound of NA=0.6 could be recognized in the insert shown in the figure. The corresponding fractional focal shift is ~0.3 (i.e., 30%).
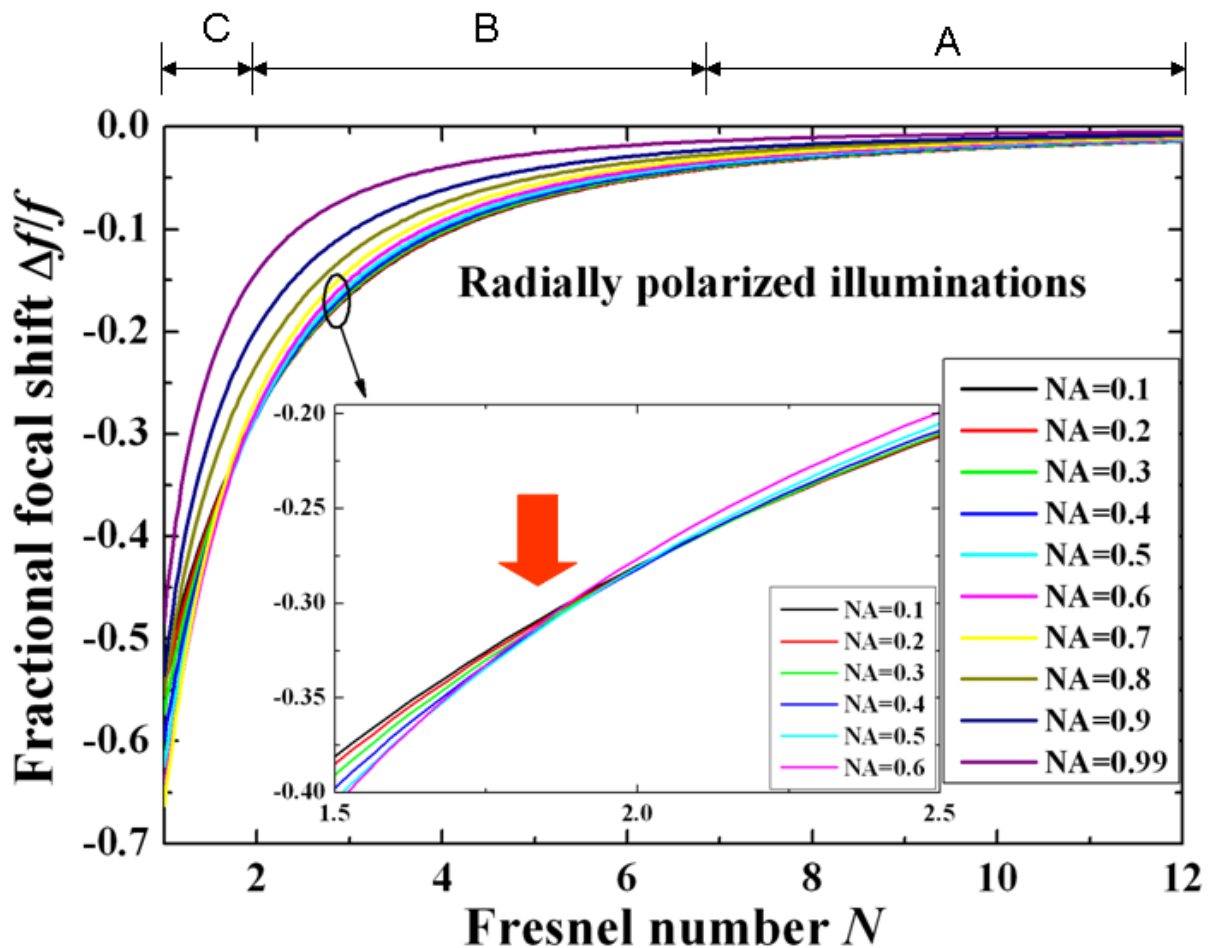
Fig. 5-4 Fractional focal shift $\Delta f/f$ versus the Fresnel number N for the radially polarized illumination (RPI).

5.3.2 The case of azimuthally polarized illumination (API)

In this subsection, we turn to focus on the case of API. The typical feature of beam

propagation can be seen by Fig. 5-3. It is different from that of RPI. However, similar

to the case of RPI, it is found that three different variations of focal shift can be

identified as shown in Fig. 5-5. It is still meaningful to note that the transition

betweens region B and C is associated with a crossover feature as denoted by the red

arrow shown in the insert of Fig. 5-5. However, the transition from the regions A to B

is with a larger N (here $N>\sim 8$ for the region A) for the case of API. Meanwhile, the

crossover is identified at $N\sim 1.7$-1.8 which is slightly less than that of RPI and the

corresponding fractional focal shift is larger, but still around 30%.
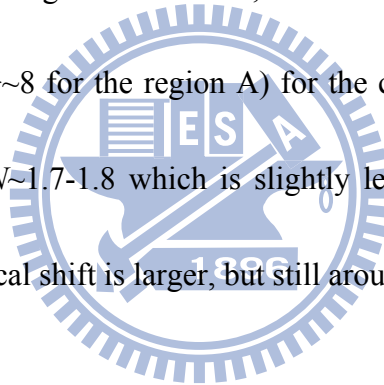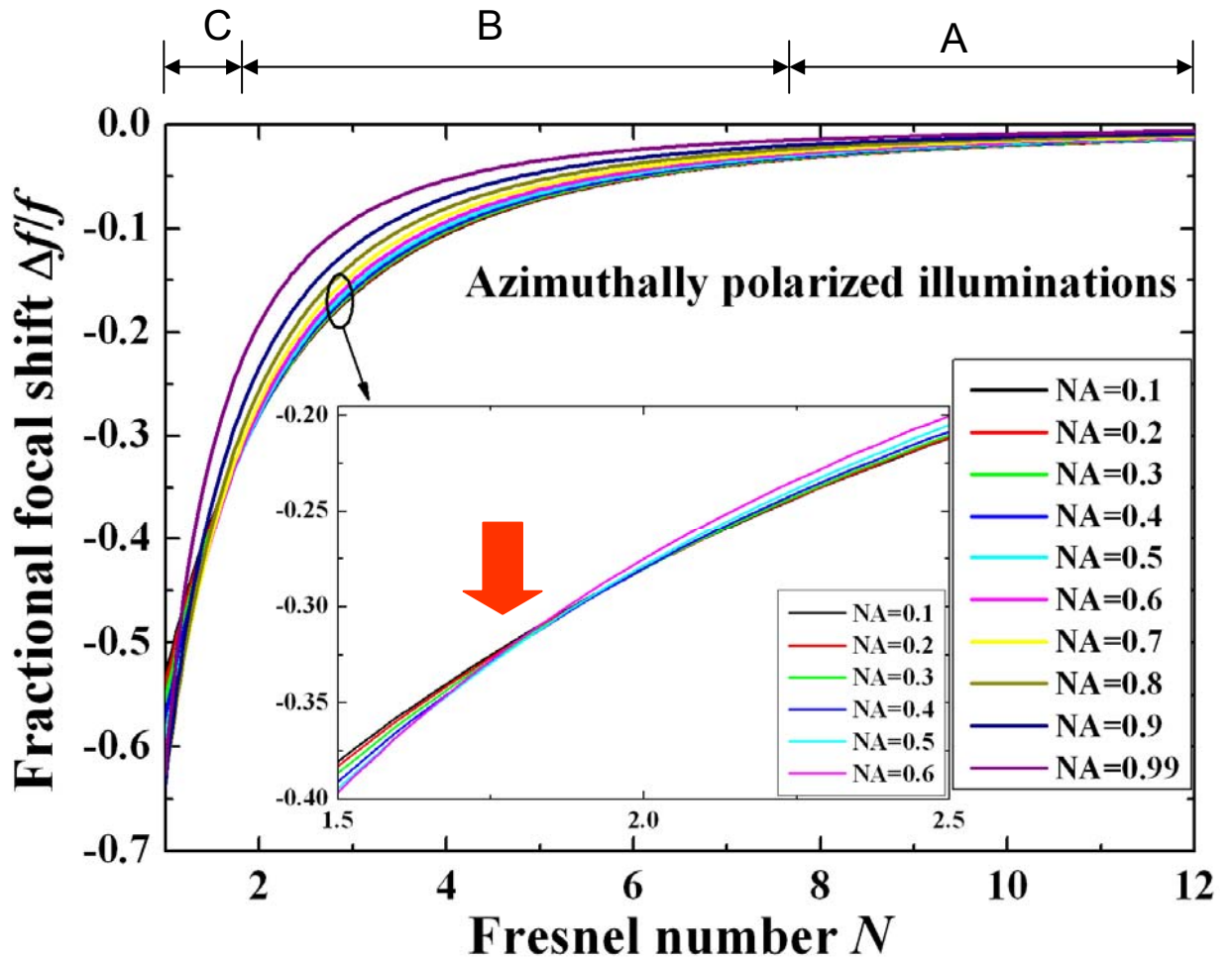
Fig. 5-5 Fractional focal shift $\Delta f/f$ versus the Fresnel number N for the azimuthally polarized illumination (API).

5.3.3 The case of linearly polarized illumination (LPI)

It is valuable to reproduce the case of LPI for comparison. In order to examine the

dependence of the fractional focal shifts by a LPI on numerical aperture NA, the

fractional focal shifts are numerically evaluated based on Ref. [53]. Fig. 5-6 shows the

result. It is possible to identify the region A for which the fractional focal shift is

taken as less than 5%. However, there is no crossover feature that could be identified

as those of RPI and API, as highlighted in the insert in Fig. 5-6, while it is still

possible to have fractional focal shift more than 30%. Unlike the cases of RPI and API, the maximum of fractional focal shift for LPI is limited within 40%, while for the case of PRI and API could reach 60-70%.
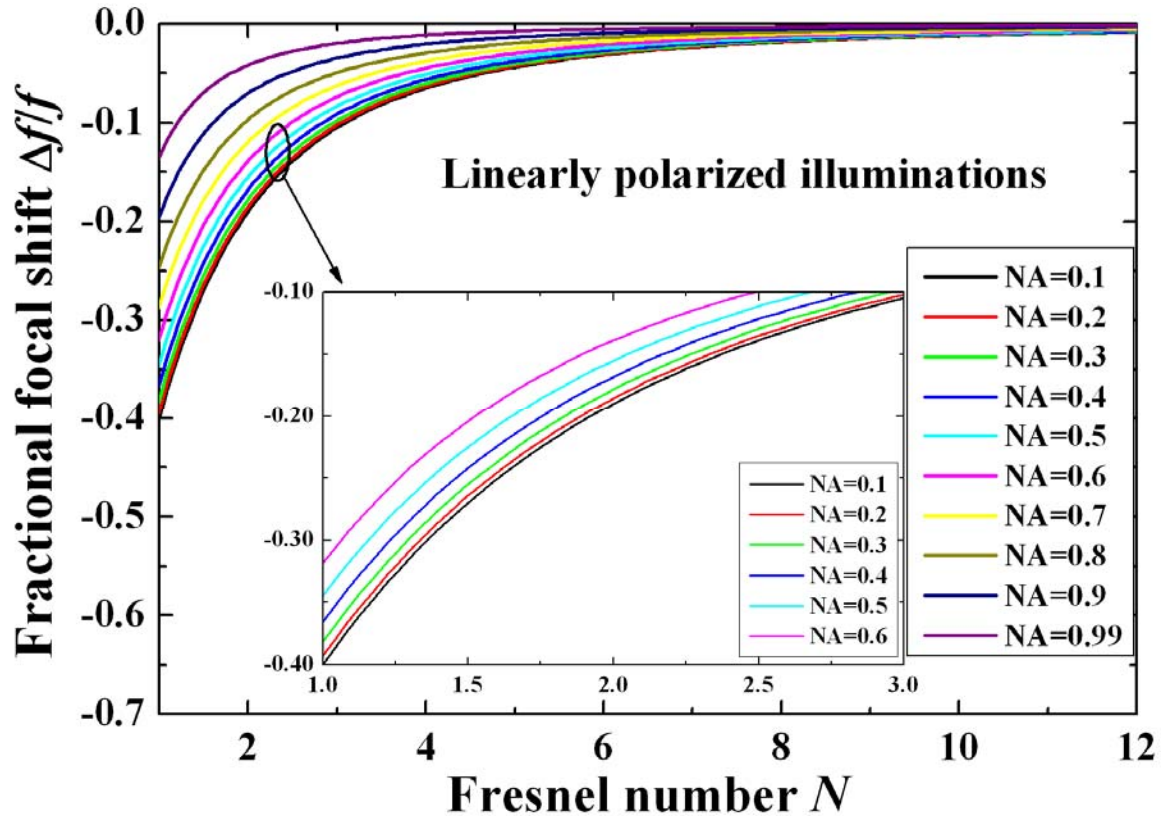
Fig. 5-6 Fractional focal shift $\Delta f/f$ versus the Fresnel number N for the linearly polarized illumination (LPI).

5.3.4 Comparison with the ratio of fractional focal shifts

To compare the differences of focal shift associated with different polarizations, the fractional focal shifts of RPI and API are normalized by that of LPI correspondingly as illustrated in Fig. 5-7. The ratio of (fractional) focal shift could provide us a whole

picture in better vision. The solid line is the ratio of (fractional) focal shifts between

PRI and LPI, while the dashed line is used to denote the ratio of (fractional) focal

shifts of API to LPI. For simplification, we show the cases of NA=0.1, 0.4, 0.7 and

0.9.
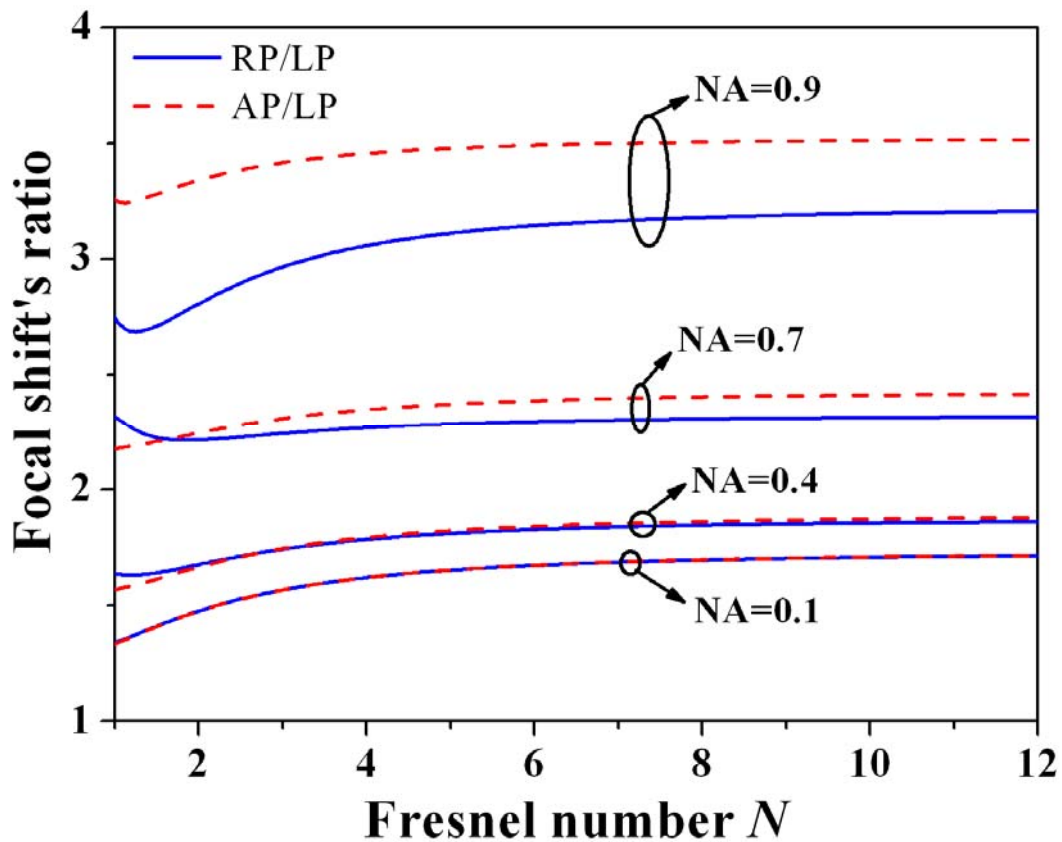
Fig. 5-7 The variation of the ratios of (fractional) focal shifts of the radially polarized
(RP) and the azimuthally polarized (AP) to the linearly polarized illuminations (LPI).
The former is denoted by a solid line while the latter is with a dash line.

As one can recognize that with a very-low-relative aperture, i.e., around NA=0.1, the

behavior of the two kinds of illumination (RPI and LPI) are nearly the same. The

power of shifting the focal point will increase as the Fresnel number is decreased. As

the Fresnel number is close to ~7-8, the variation is steady which is corresponding to

the transition from the region B to the region A as we have illustrated above. As NA

is increased, the first dissimilarity between the RPI and API occurs in the region of

low Fresnel number, as referred to the case of NA=0.4, where a thin red arrow is used

to denote the occurrence location. If we look at the case of a larger NA, e.g., NA=0.7,

there is a crossover, i.e., RPI has a greater power in shifting the focal point in low

Fresnel number, while API will take a lead as the Fresnel number lager than ~1.8. The

transition is denoted by a thick black down arrow in Fig. 5-7 for reference. When the

numerical aperture is further increased, e.g., NA=0.9, it is API to have the greatest

power in shifting the focal point for the whole range of the Fresnel number.
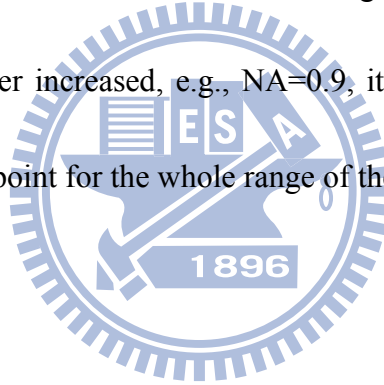
5.4 Summary

In summary, we have deduced the analytical expressions for the radially and

azimuthally polarized beams focused by an aplanatic lens by using the vector

Kirchhoff diffraction theory. A line integral around the edge of the aperture, making

the solution of Green's theorem of electromagnetic fields compatible with the

Maxwell's equations, is also calculated and added to the total electric fields. The

characteristics of field propagation have been analyzed with a center of attention on

the property of focal-shift effect. It has been shown that the focal shifts are not only

dependent on the Fresnel number, the numerical aperture, but also depend on the

incident polarization. The variation of focal shift is further classified by the fractional

focal shift and its change rate. There are basically three regions can be identified. In

one of the regions, i.e., the region A, the fractional focal shift is taken as within 5%

and its change rate ~0. The region A is mainly with large Fresnel number,

approximately $N > 7 \sim 8$. On the other hand, for very low Fresnel number, the fractional

focal shift is large, typically > 30%, and its change rate is a constant. This region is

classified as region C. In between, there is a transition; the fractional focal shift varied

inverse proportional with the Fresnel number and it is labeled as region B. The region

classification still holds for different numerical apertures and polarized illuminations.
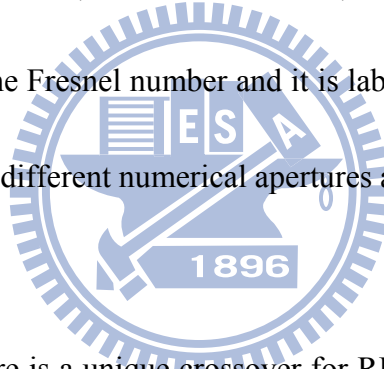
Unlike the case of LPI, there is a unique crossover for RPI and API. The crossover is

associated with the appearance of region C and the corresponding fractional focal

shift could reach up to 60-70%. On the other hand, there is no crossover that could be

identified for the case of LPI and it is interesting to note that the maximum of

fractional focal shift that could be achieved by LPI is limited with ~40%. Although

the crossover could be contributed as the result of the competition between the

numerical aperture and the Fresnel number as the incident beam is encountering

different restrictions since the polarization status is different, it is not so apparent at

all. Overall, the Fresnel number has been taken as the index of characterization, so as to the numerical aperture. When we take these two quantities in identifying the performance simultaneously, the meaning underlying the two quantities is the competition between the wave nature (λ / a) and the scale characteristic (f / a) of the corresponding system, since the Fresnel number can be expressed as $(a^2 / \lambda f) = (a / \lambda)(a / f)$ where the number aperture is (a / f). However, there is no polarization factor involved. Hence, the work shown here provides a reference for further investigation on the polarization-associated phenomena with cylindrical vector beam.

It is also worthwhile to note how the trends of focal shifts associated with RP and AP illuminations normalized with LPI could be separated as the Fresnel number is varied. The characteristics of beam propagation for the two illuminations, i.e., RPI and API, are different. But the general trend features of the two illuminations are similar in the region of large Fresnel numbers, i.e., the change rate of fractional focal shift are nearly the same, though the values are different. Furthermore, as shown above, when the system is with a low-relative aperture, e.g., 0.1, the focal shifts associated by the radially and azimuthally polarized illuminations are nearly the same, while they are about 1.65 times as large as that of linearly polarized illumination. As

the system is of high-relative aperture, e.g., 0.9, the focal shifts associated by the

radially and azimuthally polarized illuminations has ~10% difference and their ratios

with that of linearly polarized illumination become double in comparing with the case

of low-relative aperture. In other words, generally it is the azimuthally polarized

illumination to have the largest power in shifting the focal point. On the other hand,

there is anomaly in the region of very low Fresnel number which is closely related to

the onset of crossover shown in Fig. 5-4 and Fig. 5-5. The variation of focal shift in

the region of low Fresnel number is significantly different from that with large

Fresnel number.
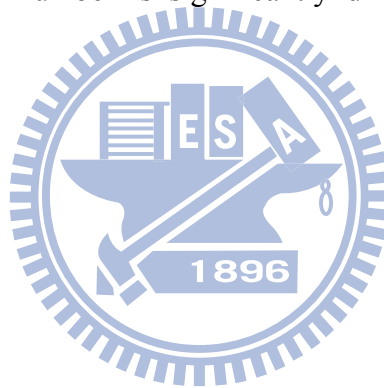
6

Conclusions and future works

6.1   Conclusions

We study the diffraction behavior of an *N*-split lens in the transversal layout i.e.,

Billet's split lens and longitudinal arrangement i.e., Meslin's split lens. The

interference patterns including the equidistant straight lines, hyperbolas, and

concentric-circle-like patterns near the optical axis generated by a Billet's *N*-split lens

have been investigated. Nevertheless, the type of lens splitting selected causes the

interference pattern of equidistant straight lines in the original Billet's lens to form an

N-fold angularly distributed pattern with an angle difference of $2\pi/N$. For a Meslin's

split lens, the rotational symmetry properties of focused field with respect to the

optical axis in the *XY*-plane and reflection symmetry with respect to the mid-point of

two foci have been studied. For an odd number of splitting *N*, there is an additional

angle shift of π/N for the azimuthally distributed patterns of equidistant straight lines.

In other words, there are two kinds of symmetry even for simple splitting operations.

On the other hand, the peak intensity distribution in the central portion resembles a

concentric-circle-like pattern, when *N* is large as a result of *N*-beam interference. As

to the Meslin's *N*-split lens, the amplitude and the phase follow

$$\left|U(-u,v,\psi+\frac{2\pi}{N})\right|=\left|U(u,v,\psi)\right| \quad \text{and} \quad \Phi(-u,v,\psi+\frac{2\pi}{N})=-\Phi(u,v,\psi)-\pi \quad \text{respectively}$$

when the splitting is with double of an even number. On the other hand, for the case

of double of an odd number, the relation changes to hold with

$$\left|U(-u,v,\psi)\right|=\left|U(u,v,\psi)\right| \quad \text{and} \quad \Phi(-u,v,\psi)=-\Phi(u,v,\psi)-\pi \text{ , where the optical units}$$

u and *v* are used to denote the *z*- and the radial coordinates respectively and the

azimuthal angle is *ψ*. Additional symmetry properties are also explored and identified,

particularly for the distributions on the focal plane. The on-axis fields have also been

discussed.

Moreover, the Bessel beam is studied and by the use of the Billet's N-split lens

distributing the focal points circularly on the focal plane. This study explores the

characteristics of beam propagation and analytically derives the asymptotic

characteristics of beam propagation based on the stationary phase approximation and

the moment-free Filon-type method. Results show that the unique Billet's *N*-split lens

can generate a quasi-Bessel beam if the number of splitting *N* is large enough, e.g., *N*

$\geqq$ 24. This study also explores the diffraction efficiency of corresponding

quasi-Bessel beam and the influence of aperture size. The potential advantage of

proposed split-lens approach is that, unlike the classical means of annual aperture, this

simple lens approach allows a much large throughput in creating the Bessel beam and

hence the Bessel beam could have more optical energy.

The diffraction behaviors of cylindrical vector beam, particularly the focal shifts

further caused by different polarizations, namely linear, radial and azimuthal, are also

investigated in terms of vector Kirchhoff diffraction theory together with an

additional line integral around the edge of the aperture to satisfy the Maxwell's

equation. The variation of focal shifts associated with numerical aperture and the

Fresnel number is also explored. It is found that with a low numerical aperture, e.g.,

0.1, the focal shifts associated by the radially and azimuthally polarized illuminations

are nearly the same, while they are about 1.65 times as large as that of linearly

polarized illumination. As the system is of high numerical aperture, e.g., 0.9, the focal

shifts associated by the radially and azimuthally polarized illuminations have ~10%

difference and their ratios with that of linearly polarized illumination become double

in comparing with the case of low numerical aperture. In general, azimuthally

polarized illumination has the largest power in shifting the focal point.

6.2 Future works

Based on the dissertation, the split lens can be used to study other non-diffracting

beams or vortex beams and consider the lens in the presence of aberration instead of a

perfect lens or a high numerical aperture system. We list the potential future works

below.

1.   Study new kind of non-diffracting beam

The new non-diffracting beams e.g. higher order Bessel beams, Mathieu beams

[25], and Airy beams [79-80] propagating with a curve are of interest to study

and generate by use of a split lens. The electromagnetic distributions in the

image space of non-diffracting beams by the split lens are an important issue to

further investigate.

2.   Vortex beams -- Optical beams with singularity

The vortex beams are a beam having phase singularity and has important

application in optical tweezers for manipulation of small objects and the control

of atomic or molecular beams in terms of the exchange of angular momentum

with optical vortices. Therefore, the vortex beam generated with the

configuration of Meslin's N-split lens is a good subject to do further research.

3.   The lens in the presence of aberrations

It is inv: ntible to bring in the aberration when making a lens. The influence of

aberrations on the performance of the generated beams by use of a split lens

needs to further investigated.

4.   The polarization of generated beams

The vector nature of electromagnetic wave has to be considered when a system

having a large numerical aperture. It is important to study these beams created

with a high numerical aperture lens in terms of vector diffraction theory.

Reference

1. J. W. Goodman, *Introduction to Fourier Optics*, 3rd Ed. (Roberts & Company Publishers, 2005).

2. H. Osterberg and L. W. Smith, Closed solutions of Rayleigh's integral for axial points," J. Opt. Soc. Am. **51**, 1050-1054 (1961).

3. M. Born and E. Wolf, *Principles of Optics*, 7th expended ed. (Cambridge University Press, 1999).

4. B. Richards and E. Wolf, "Electromagnetic diffraction in optical systems II. Structure of the image field in an aplanatic system," Proc. Roy. Soc. A **253**, 358-379 (1959).

5. See http://www.olympusmicro.com/primer/lightandcolor/opticalaberrations.html.

6. K. S. Youngworth and T. G. Brown, "Focusing of high numerical aperture cylindrical-vector beams," Opt. Express **7**, 77-87 (2000).

7. M. Mansuripur, *Classical Optics and its applications*, 2nd Ed. (Cambridge University Press, 2009).

8. D. Malacara, *Optical Shop Testing*, 3rd Ed. (Wiley Interscience, 2007).

9. L. Novotny and B. Hecht, *Principles of Nano-Optics*, (Cambridge University Press, 2006).

10. E. Wolf, *Selected works of E. Wolf, with commentary* (World Scientific, 2001).

11. S.-C. Chu and J.-L. Chern, "Characterization of the subwavelength variation signature from far-field irradiance," Opt. Lett. **29**, 1045-1047 (2004); "Retrieving two-dimensional information of the subwavelength variation from far-field irradiance", J. Opt. Soc. Am. A **23**, 2471-2475 (2006); "Characterization of

one-dimension edge roughness from far-field irradiance at subwavelength-scale precision", Opt. Commun., **281**, 1997–2001 (2008).

12. A. Senthil Kumar and R. M. Vasu, "Multiple imaging and multichannel optical processing with split lenses," Appl. Opt., **26**, 5345-5349 (1987).

13. D. Dayton, S. Sandven, J. Gonglewski, S. Browne, S. Rogers, and S. Mcdermott, "Adaptive optics using a liquid crystal phase modulator in conjunction with a Shack-Hartmann wave front sensor and zonal control algorithm," Optics Express, **1**, 338-346 (1997)

14. E. J. Fernández, P. M. Prieto, and P. Artal, "Wave-aberration control with a liquid crystal on silicon (LCOS) spatial phase modulator,", Optics Express, **17**, 11013-11025 (2009)

15. E. Collett and E. Wolf, "Symmetry properties of focused fields," Opt. Lett. **5**, 264-266 (1980).

16. C. J. Cheng and J.-L. Chern, "Symmetry Property of a generalized Billet's *N*-split lens," Opt. Commun. **283**, 3564-3568 (2010).

17. J. Durnin, J.J. Miceli, Jr., and J. H. Eberly, "Diffraction-free beams," Phys. Rev. Lett. **58** 15, 1499-1501 (1987). A review article could be found from D. McGloin, and K. Dholakia, "Bessel beams: diffraction in a new light," Contemporary Physics, **46,** 15-28 (2005).

18. W. D. Montgomery, "Self-Imaging Objects of Infinite Aperture," J. Opt. Soc. Am. **57**, 772-775 (1967).

19. V. V. Kotlyar, S. N. Khonina, and V. A. Soifer, "Algorithm for the Generation of Non-diffracting Bessel Modes," J. Mod. Opt. **42**, 1231-1239 (1995).

20. J. C. Gutierrez-Vega and M. A. Bandres, "Helmholtz-Gauss waves," J. Opt. Soc. Am. A **22**, 289-298 (2005).

21. M. Anguiano-Morales, A. Martinez, M. DavidIturbe-Castillo, and S. Chavez-Cerda, "Different field distributions obtained with an axicon and an amplitude mask," Opt. Commun. **281**, 401-407 (2008).

22. Z . Bouchal and J. Courtial, "The connection of singular and nondiffracting optics," J. Opt. A: Pure Appl. Opt. **6**, S184-8 (2004).

23. L.-G. Wang, L.-Q. Wang, and S.-Y. Zhu, "Formation of optical vortices using coherent laser beam arrays," Opt. Commun. **282**, 1088-1094 (2009).

24. Y. Lin, W. Seka, J. H. Eberly, H. Huang, and D. L. Brown, "Experimental investigation of Bessel beam characteristics," Appl. Opt. **31**, 2708-2713 (1992).

25. C.A. Dartora, M. Zamboni-Racheda, K.Z. Nobrega, E. Recami, and H.E. Hernandez-Figueroa, "General formulation for the analysis of scalar diffraction-free beams using angular modulation: Mathieu and Bessel beams," Opt. Commun. **222**, 75-80 (2003).

26. *Methods for Computer Design of Diffractive Optical Elements*, V. A. Soifer, ed., (Wiley, New York, 2002), p. 765.

27. W.-X. Cong, N.-X. Chen, and B.-Y. Gu, "Generation of nondiffracting beams by diffractive phase elements," J. Opt. Soc. Am. A **15**, 2362-2364 (1998).

28. E. R. Dufresne and D. G. Grier, "Optical tweezer arrays and optical substrates created with diffractive optical elements," Rev. Sci. Instr. **69**, 1974-1977 (1998).

29. J. E. Curtis, B. A. Koss, and D. G. Grier "Dynamic holographic optical tweezers," Opt. Commun. **207**, 169-175 (2002).

30. S. Xiang, "Efficient Filon-type methods for $\int_a^b f(x)e^{iwg(x)}dx$," Numer. Math. **105**, 633-658 (2007); A. Iserles and S. P. Norsett, "Efficient quadrature of highly oscillatory integrals using derivatives," Proc. R. Soc. A, **461**, 1383-1390 (2005).

31. B. Sick, B. Hecht, and L. Novotny, "Orientational imaging of single molecules by annular illumination," Phys. Rev. Lett. **85**, 4482–4485 (2000).

32. L. Novotny, M. R. Beversluis, K. S. Youngworth, and T. G. Brown, "Longitudinal field modes probed by single molecules," Phys. Rev. Lett. **86**, 5251-5253 (2001).

33. R. Dorn, S. Quabis, and G. Leuchs, "Sharper focus for a radially polarized light beam," Phys. Rev. Lett. **91**, 233901 (2003).

34. T. Kuga, Y. Torii, N. Shiokawa, T. Hirano, Y. Shimizu, and H. Sasada, "Novel optical trap of atoms with a doughnut beam," Phys. Rev. Lett. **78**, 4713-4716 (1997).

35. S. Sato, Y. Harada, and Y. Waseda, "Optical trapping of microscopic metal particles," Opt. Lett. **19**, 1807-1809 (1994).

36. Q. Zhan, "Trapping metallic Rayleigh particles with radial polarization," Opt. Express **12**, 3377-3382 (2004).

37. H. Kawauchi, K. Yonezawa, Y. Kozawa, and S. Sato, "Calculation of optical trapping forces on a dielectric sphere in the ray optics regime produced by a radially polarized laser beam," Opt. Lett. **32**, 1839–1841 (2007).

38. A. Bouhelier, F. Ignatovich, A. Bruyant, C. Huang, G. Colas des Francs, J.-C. Weeber, A. Dereux, G. P. Wiederrecht, and L. Novotny, "Surface plasmon interference excited by tightly focused laser beams," Opt. Lett. **32**, 2535–2537 (2007).

39. W. Chen and Q. Zhan, "Realization of evanescent Bessel beam via surface plasmon interference excited by radially polarized beam," Opt. Lett. **34**, 722–724 (2009).

40. P. L. Greene and D. G. Hall, "Focal shift in vector beams," Opt. Express **4**, 411-419 (1999).

41. P. L. Greene and D. G. Hall, "Diffraction characteristics of the azimuthal Bessel-Gauss beam," J. Opt. Soc. Am. A **13**, 962-966 (1996).

42. P. L. Greene and D. G. Hall, "Properties and diffraction of vector Bessel-Gauss beams," J. Opt. Soc. Am. A **15**, 3020-3027 (1998).

43. D. P. Biss and T. G. Brown, "Cylindrical vector beam focusing through a dielectric interface," Opt. Express **9**, 490-497 (2001).

44. A.S. van de Nes, P.R.T. Munro, S.F. Pereira, J. J. M. Braat, and P. Torok, "Cylindrical vector beam focusing through a dielectric interface: comment," Opt. Express **12**, 967-969 (2004).

45. D. P. Biss and T. G. Brown, "Cylindrical vector beam focusing through a dielectric interface: reply comment," Opt. Express **12**, 970-971 (2004).

46. D. P. Biss and T. G. Brown "Primary aberrations in focused radially polarized vortex beams," Opt. Express **3**, 384-393 (2004).

47. R. H. Jordan and D. G. Hall, "Free-space azimuthal paraxial wave equation: the azimuthal Bessel-Gauss beam solution," Opt. Lett. **19**, 427-429 (1994).

48. D. G. Hall, "Vector-beam solutions of Maxwell's wave equation," Opt. Lett. **21**, 9-11 (1996).

49. E. Y. S. Yew and C. J. R. Sheppard, "Tight focusing of radially polarized Gaussian and Bessel–Gauss beams," Opt. Lett. **32**, 3417-3419 (2007).

50. K. Yoshiki, M. Hashimoto, and T. Araki, "Second-harmonic-generation microscope using eight-segment polarization-mode converter to observe three-dimensional molecular orientation," Opt. Lett. **32**, 1680-1682 (2007).

51. M. Stalder and M. Schadt, "Linearly polarized light with axial symmetry generated by liquid-crystal polarization converters," Opt. Lett. **21**, 1948-1950 (1996).

52. D. Pohl, "Operation of a ruby laser in the purely transverse electric mode TE_{01}," Appl. Phys. Lett. **20**, 266-287 (1972).

53. Y. Li, "Focal shifts in diffracted converging electromagnetic waves. I. Kirchhoff theory," J. Opt. Soc. Am. A **22**, 68-76 (2005).

54. T. D. Visser and S. H. Wiersma, "Diffraction of converging electromagnetic waves," J. Opt. Soc. Am. A **9**, 2034-2047 (1992).

55. W. Hsu and R. Barakat, "Stratton-Chu vectorial diffraction of electromagnetic fields by aperture with application to small-Fresnel-number systems," J. Opt. Soc. Am. A **11**, 623-629 (1994).

56. Y. Li, "Focal shifts in diffracted converging electromagnetic waves. II. Rayleigh theory," J. Opt. Soc. Am. A **22**, 77-83 (2005).

57. Y. Li and E. Wolf, "Three-dimensional intensity distribution near the focus in systems of different Fresnel numbers," J. Opt. Soc. Am. A **1**, 801-808 (1984).

58. Y. Li, "Dependence of the focal shift on Fresnel number and *f* number," J. Opt. Soc. Am. **72**, 720-775 (1982).

59. Y. Li and E. Wolf, "Focal shift in diffracted converging spherical waves," Opt. Commun. **39**, 211-215 (1982).

60. Y. Li, "Focal shift in small-Fresnel-number focusing system of different relative aperture," J. Opt. Soc. Am. A **20**, 234-239 (2003).

61. C. J. R Sheppard and P. Torok, "Focal shift and the axial optical coordinate for high-aperture systems of finite Fresnel number," J. Opt. Soc. Am. A **20**, 2156-2162 (2003).

62. W. H. Carter, "Focal shift and concept of effective Fresnel number for a Gaussian beam," Appl. Opt. **21** 1989-1994 (1982).

63. Y. Li, "Oscillations and discontinuity in the focal shift of Gaussian laser beams," J. Opt. Soc. Am. A **3**, 1761-1765 (1986).

64. Y. Li and F. T. S. Yu, "Intensity distribution near the focus of an apertured focused Gaussian beam," Opt. Commun. **70**, 1-7 (1989).

65. Y. Li, "Focal shift formula for focused, apertured Gaussian beams," J. Mod. Opt. **39**, 1761-1764 (1992).

66. G. Wu, Q. Lou, J. Zhou, J. Dong, and Y. We, "Focal shift in focused radially polarized ultrashort pulsed laser beams," Appl. Opt., **46**, 6251-6255 (2007).

67. P. P. Banerjee, G. Cook, and D. R. Evans, "A q-parameter approach to analysis of propagation, focusing, and waveguiding of radially polarized Gaussian beams," J. Opt. Soc. Am. A **26**, 1366-1374 (2009)

68. W. H. Carter and M. F. Aburdence, "Focal shift in Laguerre-Gaussian beams," J. Opt. Soc. Am. A **4** 1949-1952 (1987).

69. R. I. Hernandez-Aranda and J. C. Gutierrez-Vega, "Focal shift in vector Mathieu-Gauss Beams," Opt. Express **16**, 5838-5848 (2008).

70. C. J. Bouwkamp, "Diffraction theory," Rep. Prog. Phys. **17**, 35-100 (1954).

71. Sec. 8. 11 of Ref. 3.

72. J. A. Stratton and L. J. Chu, "Diffraction theory of electromagnetic waves," Phys. Rev. 56, 99-107 (1939).

73. P. Torok, P. Varga, Z. Laczik, and G. R. Booker, "Electromagnetic diffraction of light focused through a planar interface between materials of mismatched refractive indices: an integral representation," J. Opt. Soc. Am. A **12**, 325-332 (1995).

74. R. Barakat, "Diffraction of converging electromagnetic fields in the neighborhood of the focus of a parabolic mirror having a central obscuration," Appl. Opt. **26**, 3790-3795 (1987)

75. V. S. Ignatovsky, "Diffraction by a lens having arbitrary opening," Trans. Opt. Inst. Petrograd **1**, paper 4 (1920).

76. V. S. Ignatovsky, "Diffraction by a parabolic mirror having arbitrary opening," Trans. Opt. Inst. Petrograd **1**, paper 5 (1920).

77. J. D. Jackson, "Classical Electrodynamics," 3rd Ed. (Wiley, New York, 1999).

78. W. H. Press, S. A. Teukolsky, W. T. Vetterling, and B. P. Flannery, "Direction Set (Powell's) Methods in Multidimensions," in *Numerical Recipes in C*, pp. 412-420, (Cambridge University Press, Cambridge, UK, 1992).

79. M. V. Berry and N. L. Balazs, "Nonspreading Wave Packets," Am. J. Phys. **47**, 264 (1979).

80. G. A. Siviloglou and D. N. Christodoulides, "Accelerating Finite Energy Airy Beams," Opt. Lett. **32**, 979 (2007).